UNIVERSITÀ DEGLI STUDI
DI SALERNO

Department of Industrial Engineering

Doctoral Dissertation
Doctoral Program in Innovative Engineering Technologies for Industrial Sustainability - IETIS (XXXVIII cycle)

Advanced Approach for Vibroacoustic and Aeroacoustic Analysis of Piaggio P180 Avanti

By

Carmen Brancaccio

Supervisors:
Prof. Roberto Citarella
Dr. Eng. Luigi Federico

Doctoral Examination Committee:

Roberto CITARELLA	Professor, University of Salerno (UNISA)	President and Supervisor
Sergio DE ROSA	Professor, University of Naples Federico II (UNINA)	Examiner
Christophe HOAREAU	Assistant Professor, Conservatoire National des Arts et Métiers (CNAM)	Referee and Examiner

Università degli Studi di Salerno
2026

Declaration

I hereby declare that, the contents and organization of this dissertation constitute my own original work and does not compromise in any way the rights of third parties, including those relating to the security of personal data.

Carmen Brancaccio
2026

* This dissertation is presented in partial fulfillment of the requirements for **Ph.D. degree**.

A Zia Lucia,
mia eterna amica

Acknowledgements

I gratefully acknowledge Piaggio Aerospace for providing the industrial framework and the opportunity within which this doctoral research was carried out.

I acknowledge the Italian Aerospace Research Centre (CIRA) for its technical support. In particular, I am sincerely grateful to Eng. Pasquale Vitiello for his valuable technical support and expert guidance. I would also like to extend my sincere thanks to Eng. Giovanni Fasulo for his helpful technical contributions to this work.

I wish to express my sincere gratitude to Prof. Francesco Marulo (University of Naples Federico II) for providing the acoustic test data employed in this study. His expertise and guidance were essential to the development and validation of the methodology presented in this thesis.

Finally, I thank Dr. Eng. Claudio Testa (Institute of Marine Engineering, National Research Council of Italy – INM-CNR) for his constant supervision and guidance.

Abstract

Turboprop aircraft cabin noise is strongly influenced by low frequency tonal excitation associated with the propeller Blade-Passage Frequency (BPF) and its harmonics. In this frequency range, the interior acoustic field is governed by the interaction between fuselage structural modes, cabin acoustic modes and fluid–structure coupling effects, leading to a highly receiver-dependent response. The accurate prediction of these mechanisms requires deterministic numerical models able to represent both the structural dynamics of the fuselage and the acoustic behaviour of the enclosed cabin cavity.

This thesis develops a high-fidelity coupled structural–acoustic Finite Element (FE) model of the Piaggio P180 Avanti EVO cockpit–cabin fuselage assembly for cabin noise prediction up to the third BPF harmonic of the reference propeller operating condition. In addition to the construction of the numerical model, the work proposes a modal-based mesh-sizing strategy for the structural domain, where representative fuselage subcomponents are dynamically characterised and their modal behaviour is used, with reference to the maximum frequency of interest, to define appropriate element sizes. The acoustic mesh is defined from wavelength-based criteria and made compatible with the structural discretisation along the fluid–structure interfaces. The modelling framework is assessed through a progressive verification and validation procedure. The structural model shows satisfactory correlation with the available experimental modal data, while the acoustic cavity model is successfully verified against analytical solutions for an equivalent rigid-walled cylindrical cavity. The coupled structural–acoustic response is then validated against full-scale laboratory acoustic test data obtained on a Piaggio P180 Avanti EVO fuselage barrel.

The validation considers both a body-in-white configuration and a trimmed configuration with acoustic absorbing material applied to the cabin inner surfaces. For the untreated configuration, a sensitivity analysis on the effective loaded area is performed to assess the influence of the equivalent representation of the experimental acoustic source. A further sensitivity study investigates the effect of the acoustic impedance assigned to the closing panels of the cavity. For the trimmed configuration, the absorbing material is represented through equivalent impedance boundary conditions reconstructed from measured absorption data. In the frequency range considered for the numerical–experimental comparison, from 80 Hz to 250 Hz in one-third octave bands, the main experimental Noise Reduction (NR) trends are reproduced, with the best agreement observed at receiver locations close to the excitation region. At these locations, the predicted NR values generally fall within the sensitivity envelope defined by the equivalent loaded area variations. Larger discrepancies occur at more distant receivers, where the response is more strongly affected by reflected-field contributions and by uncertainties in the representation of the experimental test article, particularly the cabin floor.

The developed framework provides a physically consistent numerical basis for low-frequency cabin noise prediction in the Piaggio P180 Avanti EVO fuselage. It also supports future studies involving realistic propeller-induced excitation, cabin noise reduction strategies and the extension towards passenger centred psychoacoustic indicators.

Keywords: Piaggio P180 Avanti EVO; turboprop cabin noise; structural–acoustic coupling; finite element method; noise reduction; modal validation; acoustic treatment.

Sommario

Il rumore in cabina degli aeromobili turboelica è fortemente influenzato da eccitazioni tonali a bassa frequenza associate alla frequenza di passaggio di pala (BPF) e alle sue armoniche. In questo intervallo di frequenze, il campo acustico interno è governato dall'interazione tra i modi strutturali della fusoliera, i modi acustici della cabina e gli effetti di accoppiamento fluido–struttura, dando luogo a una risposta fortemente dipendente dalla posizione del ricevitore. La previsione accurata di tali meccanismi richiede modelli numerici deterministici in grado di rappresentare sia la dinamica strutturale della fusoliera sia il comportamento acustico della cavità interna della cabina.

Questa tesi sviluppa un modello agli elementi finiti accoppiato strutturale–acustico ad alta fedeltà dell'assieme cabina passeggeri–cabina piloti del Piaggio P180 Avanti EVO, finalizzato alla previsione del rumore in cabina fino alla terza armonica della BPF. Oltre alla costruzione del modello numerico, il lavoro propone una strategia di dimensionamento della mesh strutturale basata sull'analisi modale, in cui sottocomponenti rappresentativi della fusoliera vengono caratterizzati dinamicamente e il loro comportamento modale viene utilizzato, con riferimento alla massima frequenza di interesse, per definire dimensioni appropriate della mesh. La mesh acustica, invece, è definita sulla base di criteri legati alla lunghezza d'onda ed è resa compatibile con la discretizzazione strutturale lungo l' interfaccia fluido–struttura.

Il modello numerico è valutato attraverso una procedura progressiva di verifica e validazione. Il modello strutturale mostra una correlazione soddisfacente con i dati modali sperimentali disponibili, mentre il modello della cavità acustica viene verificato con successo rispetto a soluzioni analitiche relative a una cavità cilindrica equivalente con pareti rigide. Successivamente, la risposta accoppiata strutturale–acustica viene validata mediante dati sperimentali acustici di laboratorio su scala reale, ottenuti su un barrel di fusoliera del Piaggio P180 Avanti EVO.

La validazione considera sia una configurazione body-in-white sia una configurazione trimmed, con materiale fonoassorbente applicato alle superfici interne della cabina. Per la configurazione non trattata, viene eseguita un'analisi di sensibilità sull'area caricata efficace, al fine di valutare l'influenza della rappresentazione equivalente della sorgente acustica sperimentale. Un'ulteriore analisi di sensibilità indaga l'effetto dell'impedenza acustica assegnata ai pannelli di chiusura della cavità. Per la configurazione trimmed, il materiale fonoassorbente è rappresentato mediante condizioni al contorno di impedenza equivalente ricostruite a partire da dati sperimentali di assorbimento.

Nell'intervallo di frequenze considerato per il confronto numerico–sperimentale, da 80 Hz a 250 Hz in bande di un terzo d'ottava, l'andamento sperimentale della riduzione di rumore (NR) è ben riprodotto, con il miglior accordo osservato nelle posizioni dei ricevitori prossime alla regione di eccitazione. In tali posizioni, i valori di NR previsti ricadono generalmente all'interno dell'inviluppo di sensibilità definito dalle variazioni dell'area caricata equivalente. Scostamenti più marcati si osservano in corrispondenza dei ricevitori più distanti, dove la risposta è maggiormente influenzata dai contributi del campo riflesso e dalle incertezze nella rappresentazione dell'articolo di prova sperimentale, in particolare del pavimento della cabina.

Il lavoro sviluppato fornisce una base numerica fisicamente consistente per la previsione del rumore, a bassa e media frequenza, nella fusoliera del Piaggio P180 Avanti EVO. Esso può supportare studi futuri riguardanti l'eccitazione realistica indotta dall'elica, strategie di riduzione del rumore in cabina e l'estensione verso indicatori psicoacustici centrati sul passeggero.

Parole chiave: Piaggio P180 Avanti EVO; rumore in cabina di aeromobili turboelica; accoppiamento strutturale–acustico; metodo degli elementi finiti; riduzione del rumore; validazione modale; trattamento acustico.

Contents

List of Figures

List of Tables

List of Acronyms

ANC Active Noise Control

ASAC Active Structural Acoustic Control

ATVA Adaptive Tunable Vibration Absorber

BEM Boundary Element Method

BPF Blade-Passage Frequency

CAD Computer-Aided Design

EPNL Effective Perceived Noise Level

FE Finite Element

FEM Finite Element Method

FRF Frequency Response Function

ICAO International Civil Aviation Organization

MAC Modal Assurance Criterion

NR Noise Reduction

OSHA Occupational Safety and Health Administration

SEA Statistical Energy Analysis

SII Speech Intelligibility Index

SIL Speech Interference Level

SPL Sound Pressure Level

STI Speech Transmission Index

TBL Turbulent Boundary Layer

TWA Time-Weighted Average

Chapter 1

Introduction

1.1 Origin and Evolution of the Aircraft Noise Problem

For the first four decades of powered flight, propellers represented the exclusive means of aircraft propulsion. During this period, research efforts progressively expanded beyond purely aerodynamic considerations to include the acoustic emissions generated by rotating blades. In particular, during the 1940s and 1950s, significant attention was devoted to understanding the physical mechanisms responsible for propeller noise generation [1]. Among the pioneering contributions, Gutin (1948) developed one of the first theoretical models of rotor noise, demonstrating that the steady aerodynamic forces acting on a propeller behave as acoustic dipole sources [2].

The introduction of the jet engine as a propulsion system for military aircraft during the Second World War marked a significant shift in the technological landscape. The substantially higher exhaust velocities associated with turbojet engines resulted in dramatically increased acoustic emissions. As jet propulsion began to be considered for commercial aviation, it became evident that effective noise mitigation strategies were required to ensure the sustainable development of civil air transport. Consequently, in the late 1940s and 1950s, substantial research efforts were devoted to understanding the physical mechanisms of jet noise generation and to developing predictive and control methodologies.

The systematic scientific discipline we now call aeroacoustics emerged during this period, described as the "marriage of acoustics with unsteady aerodynamic flow" [1]. A central milestone in the theoretical understanding of aerodynamically generated sound was the work of M.J. Lighthill (1952). Lighthill's *acoustic analogy*, complemented by several experimental studies, provided the first rigorous theoretical framework for jet noise prediction. Replacing unsteady fluid flow with a volume distribution of equivalent acoustic sources, this approach allows the estimation of the radiated noise based on the characteristic properties of the flow and empirically derived constants, thereby establishing the foundations of modern computational aeroacoustics [3–6].

The rapid growth of commercial jet transport during the 1960s led to increasing public concern regarding aircraft noise exposure around major airports. In response, formal regulatory frameworks were introduced. In 1969, the Federal Aviation Administration (FAA) formally introduced aircraft noise certification requirements through 14 CFR Part 36, establishing the first regulatory limits on aircraft acoustic emissions [7]. Shortly thereafter, in 1971, the International Civil Aviation Organization (ICAO) adopted Annex 16 to the Chicago Convention, establishing internationally harmonized aircraft noise certification standards [8]. These early regulations introduced defined certification measurement locations and adopted the Effective Perceived Noise Level (EPNL) - a measure of aircraft noise closely linked to levels of human annoyance - as the primary metric for aircraft noise evaluation. For the first time, acoustic performance became a mandatory design constraint for aircraft manufacturers [9].

As progressively stricter certification limits were introduced through successive amendments of ICAO Annex 16, incremental modifications of pure turbojet engines proved insufficient. The recognition that jet noise intensity scales approximately with the eighth power of exhaust velocity motivated a fundamental redesign of propulsion systems. The introduction of bypass and subsequently turbofan engines reduced exhaust velocity while maintaining thrust, achieving substantial acoustic benefits alongside improved thermodynamic efficiency [1]. Although the primary motivation for the adoption of turbofan engines was enhanced fuel efficiency, noise reduction represented a significant additional advantage.

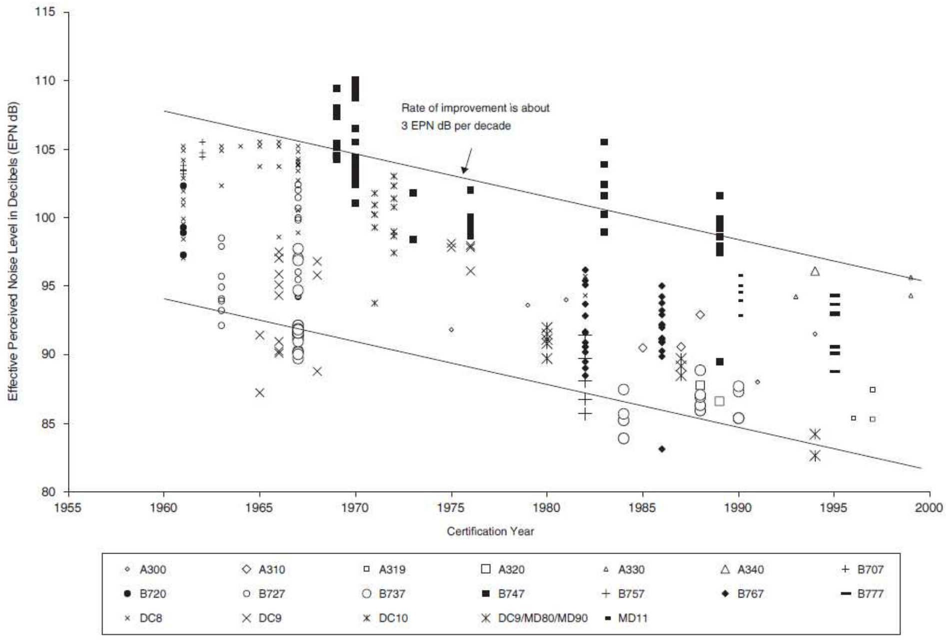

Fig. 1.1 Trends in aircraft noise levels: Effective Perceived Noise Level during takeoff for aircraft at maximum takeoff weight as a function of certification date.

Throughout the 1980s and 1990s, technological progress in aircraft noise mitigation was largely evolutionary, involving the progressive introduction of higher bypass-ratio propulsion systems, improvements in acoustic liner materials, and continuous aerodynamic and structural refinements. Analysis of aircraft certification data from the 1960s to the early 2000s shows that these developments produced a nearly linear long-term trend in noise reduction, corresponding to an average improvement of approximately 3 dB per decade, as illustrated in Fig. 1.1 [9]. This sustained progression reflects the combined influence of progressively stricter regulatory requirements and continuous technological innovation in propulsion architectures, acoustic treatments, and airframe design.

As propulsion-related noise levels were progressively reduced, the 1970s saw research attention expand beyond engine sources to include airframe noise, defined as the non-propulsive acoustic emissions generated by aircraft in flight. Major sources include flap and wing trailing edges, flap side edges, landing gear, cavity mechanisms, turbulent boundary layers over the fuselage and wings, and structural panel vibrations [1]. The recognition of complex interactions among noise sources and propagation mechanisms highlighted the necessity of integrated design approaches. Rather than addressing acoustic issues as a post-design correction, the concept of "silent integrated design" emerged, promoting the inclusion of aeroacoustic considerations from the earliest stages of aircraft development.

Over the following decades, aircraft noise regulations continued to evolve through progressively more stringent certification standards. Successive amendments of ICAO Annex 16 introduced increasingly restrictive limits, culminating in the most recent Chapter 14 requirements. These limits are expressed in terms of cumulative EPNL values evaluated at three reference points: fly-over (6.5 km from the brake release point, under the take-off flight path), sideline (the highest noise measurement recorded at any point 450 m from the runway axis during take-off) and approach (2 km from the runway threshold, under the approach flight path). The regulatory framework applies to both turbofan-powered and propeller-driven aeroplanes and is primarily directed toward the control of aircraft noise radiated to the external environment. Reducing the number of people affected by significant aircraft noise has therefore become one of the main priorities of the ICAO [10].

Unlike external aircraft noise, which is regulated through international certification standards, no specific certification limits exist for interior aircraft cabin noise. Instead, when cabin noise exposure is considered from a regulatory perspective, it is typically evaluated with reference to occupational noise exposure guidelines intended to protect flight crew members as workers [11]. Within this framework, noise exposure limits are commonly expressed in terms of a time-weighted average (TWA) over a standard working period. In the United States, the Occupational Safety and Health Administration (OSHA) establishes an action level of 85 dB(A) over an 8-hour TWA, above which employers must implement hearing conservation programs, and a permissible exposure limit of 90 dB(A) over the same exposure period [1]. Measurements

[1]Historically, the FAA held primary responsibility for the safety and health aspects of cockpit and cabin crew working environments, a role assumed in 1975. However, in 2013 the FAA issued a policy statement clarifying that OSHA has the authority to enforce its occupational noise exposure standards within aircraft cabins during operations.

reported in the literature indicate that typical cabin noise levels during cruise generally range between 60 and 80 dB(A), remaining below these occupational thresholds in most operating conditions, although higher levels — approaching 90–93 dB(A) — may occur during specific phases of flight such as takeoff [11, 12].

Aircraft manufacturers typically establish internal cabin noise targets in response to customer expectations and passenger experience requirements. Achieving acceptable cabin acoustic conditions requires a detailed understanding of the physical mechanisms responsible for interior noise generation and transmission. These mechanisms arise from complex interactions between aerodynamic excitation, structural vibration of the fuselage, and acoustic propagation within the enclosed cabin volume, which together constitute the core of aircraft *vibroacoustic* analysis.

Identifying the dominant noise sources and their transmission paths is therefore essential for predicting, assessing and ultimately reducing interior aircraft noise.

1.2 Cabin Noise Sources

Aircraft cabin noise is generally divided into two main contributions: noise generated by the propulsion system and noise associated with the airframe itself [13]. The characteristics of engine noise depend strongly on the propulsion architecture. Aircraft engines are commonly classified into piston, turbojet, turbofan, and turboprop types. Among these, the present work focuses primarily on the turboprop configuration.

A turboprop propulsion system essentially consists of two main components: a gas turbine engine and a propeller. The gas turbine provides the thermodynamic power cycle, including air compression, combustion, and energy extraction, while the propeller converts the mechanical power delivered by the turbine into thrust by accelerating a large mass of air. A schematic representation of the operating principle of a turboprop engine is shown in Fig. 1.2.

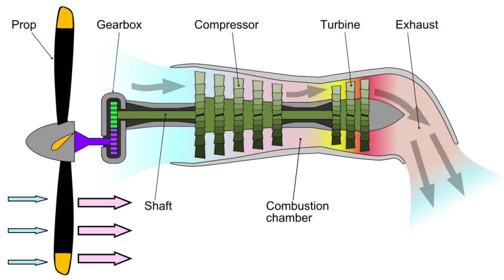

Fig. 1.2 Schematic diagram showing the operation of a turboprop engine.

In turboprop aircraft, noise is mainly generated by periodic aerodynamic and mechanical sources associated with rotating components, such as the propeller blades and internal turbomachinery.

Propeller noise can be classified into three categories: harmonic noise, broadband noise, and narrow-band random noise. Harmonic noise represents the periodic component of the acoustic signal, whose time signature can be described as a pulse repeating at a constant rate. For an ideal propeller rotating at a constant speed, the acoustic signal is characterised by a fundamental frequency corresponding to the Blade-Passage Frequency (BPF), defined as

$$f_{BPF} = \frac{N_B \, N_{RPM}}{60} \tag{1.1}$$

where N_{RPM} is the propeller rotational speed in revolutions per minute and N_B is the number of propeller blades.

Since the pressure pulses generated by the propeller are not purely sinusoidal, the acoustic spectrum contains several harmonic components occurring at integer multiples of the fundamental frequency. The frequency of the n-th harmonic can therefore be written as

$$f_n = n \, f_{BPF} \qquad n = 1, 2, 3, \ldots \tag{1.2}$$

Broadband noise, in contrast, is stochastic in nature and contains energy distributed across a wide range of frequencies. In the case of propellers, the resulting frequency spectrum is continuous, although its amplitude distribution may vary with frequency, producing a characteristic spectral shape.

Narrow-band random noise exhibits a quasi-periodic behaviour in the time domain. Although the signal may appear approximately periodic, detailed analysis shows that the energy associated with each harmonic component is not concentrated at a single discrete frequency. Instead, it is distributed over a narrow frequency range around the harmonic frequencies. Consequently, while the spectrum still displays identifiable harmonic components, these peaks are broadened rather than appearing as sharp spectral lines, particularly at higher frequencies.

Aircraft noise may also originate from aerodynamic interactions between the airflow and the aircraft structure, commonly referred to as airframe noise. This type of noise is primarily generated by turbulent flow phenomena around non-propulsive components such as wings, fuselage, landing gear, and high-lift devices. From the perspective of cabin acoustics, pressure fluctuations associated with the turbulent boundary layer along the fuselage may excite structural vibrations of the aircraft skin panels, contributing to the interior noise field.

In addition to the noise generated by the propulsion system and by aerodynamic interactions with the airframe, which radiates toward the fuselage as *airborne* acoustic excitation, further mechanisms contribute to the generation of interior cabin noise. Mechanical excitations generated within the propulsion system — such as vibrations associated with rotating machinery, gearbox components, and propellers — as well as aerodynamic loads acting on lifting surfaces, including the interaction of the propeller wake with the wing and tail surfaces, may directly excite the aircraft structure. These dynamic forces induce vibrations that propagate through the structural framework of the airframe and may subsequently radiate acoustic energy into the cabin. These vibrational disturbances are commonly identified as *structure-borne* noise [14].

Consequently, interior aircraft noise arises from the combined contribution of airborne acoustic excitation and structure-borne vibrations. The resulting sound field inside the cabin is therefore governed by coupled interactions between aerodynamic pressure fluctuations, fuselage structural dynamics and acoustic radiation within the enclosed cabin space. These interactions form the basis of the aircraft vibroacoustic problem [15]. The acoustic environment generated by these mechanisms directly affects the conditions experienced by passengers and crew inside the aircraft cabin. For this reason, understanding and controlling interior aircraft noise is not only a vibroacoustic modelling challenge, but also a key requirement for improving passenger comfort during flight.

1.3 Impact of Interior Aircraft Noise on Passenger Comfort

As early as the 1930s, the importance of acoustic comfort in air transportation had already been recognized. Bassett and Zand [16] observed that, when scheduled passenger flights began to become widespread, complaints about cabin noise rapidly emerged, and "many have decided that, except in emergencies, the discomfort of air transportation is not worth the speed." Until that time, aircraft noise had largely been accepted by pilots and early passengers as an *unavoidable evil* associated with high-speed flight. However, with the expansion of commercial aviation, it became clear that excessive cabin noise could negatively affect passenger acceptance of air transport, highlighting the need to maintain cabin noise levels below the *discomfort level*.

Within the aerospace industry, improving passenger comfort has progressively become a major design objective. In scientific literature, comfort is commonly defined as a pleasant state of physiological, psychological and physical harmony between a human being and the surrounding environment, or more generally as a sense of subjective well-being [17]. Within this framework, the study and control of Noise, Vibration and Harshness (NVH) have become key aspects of aircraft design. Aircraft cabin noise, identified as any unwanted sound perceived by passengers, together with structural vibrations transmitted through the fuselage, may lead to discomfort during flight and significantly affect the perceived quality of the flight experience. The concept of harshness refers to the subjective perception of the quality and unpleasantness of noise and vibration stimuli experienced inside the cabin, including how abrupt, rough, or intrusive they are perceived. This perception is influenced not only by the magnitude of noise and vibration, but also by their spectral content and temporal characteristics [18].

Traditionally, the quantification of interior noise has relied on energy-based acoustic metrics, such as the equivalent continuous sound pressure level (L_{eq}), which represents the total sound energy averaged over a given time interval. To better reflect human hearing sensitivity, these measurements are typically adjusted using the A-weighted sound pressure levels, in dB(A), which emphasize mid-frequency components that are most relevant for speech intelligibility and perceived annoyance [19]. However, in large aircraft cabins and especially in turboprop environments, low-frequency noise may play a significant role in passenger discomfort. For this reason, C-weighted levels, expressed in dB(C), are sometimes used to better account for low-frequency contributions that are only partially represented by the A-weighting curve [20, 21].

Despite their widespread use, purely energy-based acoustic metrics often fail to fully explain the variability of subjective passenger responses to cabin noise. These limitations have motivated the integration of psychoacoustic approaches, which aim to relate the physical characteristics of sound to the auditory perceptions they evoke [22]. In recent years, psychoacoustic analysis has been increasingly applied across several engineering fields, including aircraft noise and propulsion-system design [23–26]. Psychoacoustic metrics extend conventional acoustic analysis by describing specific perceptual attributes of sound, such as Loudness, Sharpness, Tonality, Roughness, and Fluctuation Strength [27, 28]. Loudness, measured in Sones according to ISO 532-1 or Zwicker's model, is generally recognized as one of the dominant predictors of perceived annoyance, while Sharpness quantifies the high-frequency content and correlates with the perception of a "treble" versus "bass" timbre. Tonality is particularly relevant in turboprop aircraft, where discrete tonal components generated by propellers or engines can significantly increase perceived annoyance. Roughness and Fluctuation Strength describe the rapid or slow temporal modulations of the sound field, respectively, and may be relevant for evaluating the impulsive nature of rotorcraft noise or Turbulent Boundary Layer (TBL) excitations.

The noise level inside an aircraft cabin not only influences passengers' overall acoustic comfort, but also affects the intelligibility of speech and the ease of verbal communication between passengers and crew [29]. For this reason, several objective metrics have been developed to quantify speech intelligibility in noisy environments. Among the most widely used indicators is the Speech

Interference Level (SIL), which provides a simplified estimate of the masking effect of background noise on speech communication. The SIL is typically defined as the arithmetic average of the Sound Pressure Level (SPL) in the octave bands centered at 500, 1000, 2000, and 4000 Hz, corresponding to the frequency range that contributes most significantly to speech perception [30]. More advanced objective measures include the Speech Transmission Index (STI) and the Speech Intelligibility Index (SII), both designed to predict speech intelligibility under different acoustic conditions [31, 32]. The STI evaluates the degradation of temporal amplitude modulations of the speech signal caused by background noise and reverberation, providing a quantitative index between 0 and 1 that correlates with subjective intelligibility ratings. The SII, derived from the earlier Articulation Index (AI), is based on the proportion of speech information that remains audible to the listener. The method divides the speech spectrum into several frequency bands and computes a weighted average of the signal-to-noise ratios within each band, where the weighting factors reflect the relative importance of each band for speech understanding. These metrics provide useful tools for assessing the impact of cabin noise on speech communication and perceived acoustic comfort inside aircraft cabins.

With the increasing competitiveness of the aviation market, passenger comfort and customer satisfaction have progressively become key factors influencing aircraft design and airline operations [33]. The quality of the cabin environment therefore plays a crucial role in shaping passengers' perception of the travel experience. Recognizing the strong relationship between passenger comfort and customer loyalty, airlines are increasingly focusing on improving the quality of the cabin environment as a strategy to attract and retain passengers. The growing demand for improved cabin comfort, together with increasingly stringent external noise requirements, has made vibroacoustic performance a critical consideration in modern aircraft design.

1.4 Vibroacoustic Analysis of Turboprop Aircraft Cabin Noise

When an elastic structure interacts with a surrounding fluid, structural vibrations and acoustic pressure fields in the fluid become coupled through fluid–structure interaction mechanisms. The acoustic pressure acting along the fluid–structure interface generates distributed loads on the structure, modifying its vibrational response, while structural oscillations simultaneously induce pressure fluctuations in the adjacent fluid domain. The strength and nature of these bidirectional interactions, commonly referred to as *vibroacoustic coupling*, depend on several factors, including the geometry of the structural and fluid domains, the material properties of both the structure and the fluid, and the frequency content of the dynamic excitation [34]. In particular, the coupling strength is strongly influenced by the density of the surrounding fluid. When the fluid is relatively light, such as air, the acoustic loading generally produces a limited feedback effect on the structural dynamics, and the interaction is commonly referred to as weak coupling [35]. Conversely, when the surrounding medium is heavy, such as water, the acoustic loading exerted on the structure becomes significant and may strongly affect the structural response, resulting in strong coupling conditions [36]. In aircraft cabin applications, the internal cavity is filled with air; therefore, the structural–acoustic interaction is generally characterised by weak coupling. Nevertheless, the coupled response may still become significant when structural natural frequencies are close to acoustic cavity modes, leading to efficient energy transfer between the fuselage structure and the internal pressure field [37].

Due to increasingly stringent structural weight requirements, aircraft cabins are typically designed as lightweight thin-shell structures. As a consequence, they are particularly susceptible to vibration and noise excitation from both external and internal sources. In this context, cabin noise amplification may arise from the combined effects of structural vibration, vibroacoustic coupling and cavity resonance. While structural vibrations provide the transmission path from the external excitation to the cabin interior, acoustic cavity modes may amplify the internal sound field when they are excited within the frequency range of interest [38].

From a computational perspective, the analysis of vibroacoustic problems requires the structural equations of motion to be solved together with the acoustic wave equation governing the pressure field in the fluid domain. Depending on the level of interaction to be represented, either uncoupled or coupled formulations may be adopted. The objective is to determine the structural degrees of freedom, such as displacements and rotations, as well as the acoustic degrees of freedom represented by the pressure field. In an uncoupled approach, the structural response is first computed and then used as an input for the acoustic analysis. In contrast, in coupled analysis the structural and acoustic equations are combined into a single system that accounts for the mutual interaction between the structure and the surrounding fluid. In this case, the acoustic loading generated by the fluid medium is directly incorporated into the structural equations, and the structural and acoustic degrees of freedom are solved simultaneously [39].

In turboprop aircraft, interior cabin noise is primarily dominated by discrete tonal components occurring at multiples of the BPF, together with broadband contributions generated by the turbulent boundary layer. These excitation mechanisms concentrate a significant portion of the acoustic energy within the low-frequency range where tonal propeller noise and structural–acoustic modal interactions dominate the interior sound field [40, 41].

In the BPF range and its lower harmonics, the vibroacoustic response is largely deterministic. At these frequencies, both the stiffened airframe and the enclosed cabin cavity exhibit low modal density, characterised by sparse and well-separated natural modes [42]. Consequently, the interior sound field may exhibit strong spatial variability, with pronounced seat-to-seat differences associated with the location of nodal and antinodal regions of the acoustic modes. In this regime, an accurate description of the vibroacoustic behaviour requires deterministic modelling approaches capable of capturing the modal characteristics of the structural and acoustic subsystems [43–46]. Such analyses typically require detailed information about geometry, material properties, and boundary conditions [43].

The selection of the most appropriate vibroacoustic modelling strategy depends not only on the frequency range of interest, but also on the spatial and spectral resolution required for the predicted structural and acoustic responses [47]. Deterministic numerical methods, such as the Finite Element Method (FEM) and the Boundary Element Method (BEM), are mesh-based approaches that rely on detailed descriptions of the geometry, material properties, and boundary conditions of the structural and acoustic domains [47, 48]. In these methods, the physical domain, or its boundary in the case of BEM, is discretized into a finite number of elements connected at nodes, allowing the vibration and sound pressure responses to be computed at discrete spatial locations and over narrow frequency bands. As a result, deterministic approaches provide high spatial and spectral resolution and are particularly suitable for analysing modal phenomena, local resonances and structural–acoustic transmission paths. The accuracy of deterministic methods strongly depends on the spatial resolution of the mesh. In particular, the element size must be sufficiently small to capture the structural and acoustic wavelengths associated with the highest frequency of interest. As the analysis frequency increases, the structural and acoustic wavelengths decrease and the required mesh density increases significantly. This leads to a rapid growth in the number of degrees of freedom of the numerical model and, consequently, in the computational cost of the simulations, especially for large structures such as aircraft fuselages.

For this reason, deterministic approaches may become computationally impractical for large-scale vibroacoustic systems or for analyses extending to high frequencies. As the frequency increases, the modal density of both the structural and acoustic subsystems grows and individual modes begin to overlap. Under these conditions, the vibroacoustic response becomes increasingly diffuse and the prediction of individual modal contributions becomes less meaningful. In such situations, statistical modelling strategies can be adopted. Among these approaches, Statistical Energy Analysis (SEA) represents one of the most widely used techniques for high-frequency vibroacoustic analysis [49]. Instead of resolving detailed vibration and pressure fields, SEA describes the average exchange of vibrational and acoustic energy between interconnected subsystems.

However, statistical approaches are inherently less suited to reproduce the deterministic, mode-driven spatial variability that characterizes low-frequency turboprop cabin noise. In addition, they may be sensitive to modelling choices when boundary conditions and excitation are not characterised with sufficient fidelity [50, 42]. In the frequency range dominated by the BPF and its lower harmonics, the vibroacoustic behaviour is governed by a limited number of structural and acoustic modes, and localized resonant transmission paths play a dominant role in determining the interior sound field. For this reason, deterministic approaches based on coupled structural–acoustic FE modelling — sometimes combined with BEM formulations for the exterior acoustic field — are widely employed to capture modal coupling effects, structural transmission paths, and the influence of geometrical details such as frames, stringers, floors, and window regions [51, 52, 43].

In this context, the use of high-fidelity structural and acoustic models becomes essential. Simplified geometrical representations or idealized boundary conditions may reproduce general trends of the vibroacoustic response, but they may not fully capture the actual transmission mechanisms and the local pressure distributions observed in realistic aircraft cabin environments.

1.4.1 State of the Art in Interior Noise Prediction and Control

Within the broader field of aircraft cabin vibroacoustics, turboprop aircraft represent a particularly demanding class of configurations because their interior acoustic environment is strongly affected by low-frequency tonal excitation generated by the propellers. In contrast with turbofan-powered aircraft, where cabin noise is often dominated by broadband aerodynamic sources and structural transmission through the fuselage, turboprop aircraft exhibit pronounced discrete-frequency components associated with the BPF and its harmonics. Recent comparative measurements between turboprop and turbofan cabins have confirmed that turboprop aircraft may exhibit a more severe interior noise environment. In particular, C-weighted sound pressure levels (L_{Ceq}) during cruise were found to be higher, reflecting the strong contribution of low-frequency noise. The primary technical concern lies in the presence of dominant low-frequency tones — stemming from propeller blade emissions and airframe vibrations — which stand out from the broadband background and are not adequately captured by standard A-weighting filters [53]. These findings are consistent with measurement-based investigations on regional turboprops [40], which identified the propellers as the most significant contributors to cabin noise. In particular, the fundamental propeller frequency and its harmonics were shown to dominate the interior spectra during cruise conditions, together with significant components associated with structural and acoustic resonances arising from the interaction between the propeller wake and the airframe. Furthermore, comfort-oriented investigations have confirmed that the combined effect of low-frequency noise and structural vibration remains a major challenge in turboprop cabin design [21].

From a vibroacoustic modelling perspective, turboprop interior noise can be interpreted as a classical *source–path–receiver* problem in which the dominant source is the propeller system, the main transmission path is the airframe structure, and the receiver is the enclosed cabin cavity. The importance of installation effects in this chain has been clearly demonstrated by Chirico et al. [54], who showed that propeller installation, layout and phase relationships can significantly modify the resulting tonal acoustic field. More recent simulation studies on multi-propeller aircraft have further confirmed the relevance of integrated external–interior acoustic analyses for low-noise turboprop design [55, 56].

Because the low-frequency response of turboprop cabins is governed by discrete tonal excitation and by relatively low modal densities of both the fuselage structure and the acoustic cavity, deterministic modelling approaches are particularly suitable in this regime. One of the earliest computational approaches specifically addressing turboprop cabin noise relied on deterministic structural–acoustic formulations ased on the coupled use of FEM and BEM. In this context, Ahlquist et al. [52] developed a coupled FEM/BEM vibroacoustic model of a turboprop aircraft, establishing a foundational methodology for low-frequency noise prediction in turboprop cabins, specifically focusing on the first three BPF tones. Subsequent studies have increasingly relied on high-fidelity FE models to resolve local structural–acoustic coupling, seat-to-seat variability and the influence of realistic cabin geometries. Cinefra et al. [57], for instance, developed a detailed FE vibroacoustic model of a regional turboprop cabin and used it to predict the interior sound pressure field and evaluate the impact of innovative materials and acoustic treatments on cabin comfort. Their study demonstrates that the low-frequency (0-300 Hz) interior response is highly sensitive to the fuselage's structural layout, specifically the disposition of stiffenings and the use of poro-elastic sandwich configurations, which significantly influence noise reduction levels in regions distant from structural reinforcements. Similarly, Moruzzi et al. [58] investigated the use of sandwich trim panels with heterogeneous acoustic metamaterial cores for low-frequency attenuation in a regional turboprop cabin. Their subsequent work on a windowless fuselage configuration further demonstrated that architectural modifications and resonant metamaterial treatments can significantly alter the vibroacoustic response in the 100–300 Hz range, where BPF-related acoustic energy is concentrated [59]. These studies confirm the relevance of deterministic high-fidelity FE modelling for capturing local modal coupling and spatial variations of the interior pressure field.

Despite these advances in predictive modelling, the mitigation of low-frequency noise remains a challenging problem in acoustic engineering. In turboprop aircraft, this issue is particularly critical because propeller-induced tonal noise is concentrated in the low-frequency range. As a consequence, traditional sound insulation and absorption materials — which are generally more effective at higher frequencies — often provide limited attenuation in the frequency bands associated with the BPF and its harmonics. This limitation stems from the physical principle that long-wavelength (low-frequency) acoustic waves can pass through insulating layers without undergoing significant damping [40]. For this reason, significant research effort has been devoted to active, semi-active and hybrid noise control strategies, specifically targeting low-frequency tonal components. Reviews on active vibroacoustic control in aerospace applications highlight aircraft interior low-frequency noise as one of the most suitable targets for active or semi-active control approaches [60]. These include Active Noise Control (ANC) systems based on loudspeakers generating anti-noise within the cabin, Active Structural Acoustic Control (ASAC) techniques using piezoelectric actuators to reduce structural radiation from the fuselage, adaptive tunable vibration absorbers (ATVA) designed to target dominant tonal components, and active or semi-active engine mounting systems that modify the dynamic stiffness of the support structure in order to reduce vibration transmission. Misol [61] demonstrated significant reductions of propeller-induced interior noise in a twin turboprop aircraft using smart active sidewall panels. Romeu et al. [62] proposed a FEM/BEM-based optimisation framework for ANC in turboprop cabins, shifting the control objective from local pressure minimisation to global acoustic energy reduction. In addition to global control strategies, several studies have investigated localized ANC solutions. Yoon et al. [63] investigated the influence of ANC on perceived passenger annoyance in turboprop cabins through psychoacoustic experiments, showing that although ANC can effectively reduce dominant low-frequency tonal components, the perceived improvement in comfort may be smaller than expected due to spectral changes in the residual sound field. Similarly, Dimino et al. [64] evaluated an ANC system integrated into aircraft seat headrests, demonstrating that localized control strategies can generate effective zones of quiet near the passenger's ears and significantly reduce the low-frequency tonal noise typical of turboprop aircraft cabins. These studies indicate that active control represents a promising route for low-frequency tonal noise mitigation, but also confirm the need for accurate predictive models of the cabin sound field.

Alongside active control, passive and hybrid passive–active concepts have received increasing attention. Moruzzi et al. [58, 59] demonstrated that metamaterial-based trim panels can significantly improve low-frequency noise attenuation in regional turboprop cabins compared with conventional soundproofing solutions. Their studies showed that resonant metamaterial concepts can be integrated not only as add-on acoustic treatments but also as structural design elements influencing the overall cabin vibroacoustic response. In a broader aircraft-cabin context, Leão et al. [65] explored multilayer porous and nano-fibrous treatments for cabin noise attenuation. Their work highlighted the potential of advanced lightweight acoustic treatments whose combined behaviour resembles that of a Helmholtz resonator, enabling improved acoustic performance particularly in targeted low-frequency bands [65]. Hybrid solutions combining passive insulation with active control have also been proposed. Aloufi et al. [66] developed a quadruple-panel aircraft cabin window system combining passive insulation with ASAC. While the passive architecture effectively attenuates mid-to-high frequencies, piezoelectric stack actuators integrated into the window boundaries actively target low-frequency sound transmission.

Although deterministic approaches are essential in the low-frequency range, a single modelling strategy is generally not sufficient across the entire vibroacoustic spectrum. In this context, Cotoni et al. [50] discussed the Hybrid FE–SEA method for aircraft interior noise analysis, showing that FE details can be introduced into an SEA framework to improve mid-frequency predictions while maintaining a manageable computational cost. Petrone et al. [45] developed a SEA model of an aircraft fuselage section to predict interior SPL at cruise conditions in the medium-to-high frequency range and investigated the influence of different cabin configurations in order to identify the main parameters affecting acoustic insulation performance. More recently, Hesse et al.

[43] proposed a knowledge-based model generation framework for aircraft cabin noise prediction starting from pre-design data. Although highly relevant for early design stages, this approach still relies on simplified structural representations in order to maintain computational efficiency. NASA studies by Grosveld on the Large Civil Tiltrotor also adopted a frequency-dependent modelling strategy, combining deterministic and hybrid approaches to predict cabin noise generated by turbulent boundary layer excitation and blade-passage-related sources over a broad frequency range [46, 42]. These studies confirm that deterministic modelling is particularly relevant at low frequencies, while hybrid and statistical approaches become increasingly advantageous as the frequency range increases.

A recurrent feature of the literature is the widespread use of reduced models, subsystem models and fuselage sections. This is particularly evident in SEA-based and hybrid studies, where the objective is often to assess the influence of trim systems, windows, damping layers or sidewall treatments on a representative fuselage segment rather than on a complete fuselage assembly [45, 50]. While such reduced configurations are extremely useful for isolating transmission mechanisms and exploring parametric trends, they may not fully account for some aspects of the response of the complete fuselage assembly. These include longitudinal structural continuity, global barrel modes, floor participation, and the actual spatial arrangement of openings, frames, stringers and local reinforcements. This aspect becomes particularly relevant in turboprop aircraft, where BPF-related excitation lies in a frequency range in which individual structural and acoustic modes remain clearly identifiable and where local and global modal interactions may both influence the interior acoustic field [40, 53, 57].

Another recurring limitation concerns experimental validation. A substantial fraction of published studies remains predominantly numerical, and when validation is performed, it is often limited to acoustic response quantities without prior structural dynamic validation of the FE model in terms of natural frequencies and mode shapes. Section-based studies and treatment-oriented investigations are typically validated against local acoustic indicators or transfer functions rather than against a comprehensive dataset representative of a complete aircraft configuration [57, 58, 43]. Conversely, experimental studies provide valuable insights, but often pursue different objectives, focusing on specific subsystems, active or passive noise-control strategies, or the subjective perception of cabin noise. Misol's full-scale experiments on the active reduction of propeller-induced interior noise in a Dornier Do728 aircraft represent a notable example: they provide strong experimental evidence for the effectiveness of active trim panels, but their objective is not the development and validation of a complete structural and vibroacoustic FE framework for predictive fuselage modelling [61]. A similar consideration applies to comfort- and annoyance-oriented studies, which are essential for understanding the perceptual effects of cabin noise, but do not directly address the validation of high-fidelity vibroacoustic models against structural and acoustic experimental data [21, 63].

Overall, the current state of the art suggests three main conclusions. First, turboprop cabin noise is predominantly a low-frequency vibroacoustic problem in which the BPF and its harmonics play a central role [40, 53, 62]. Second, deterministic and coupled FEM/BEM approaches remain essential in the low-frequency range, whereas hybrid FE–SEA and SEA methods become more suitable as modal density increases and modal overlap becomes significant [52, 57, 50, 45, 46]. Third, despite the increasing number of studies on turboprop cabin noise and its mitigation, relatively few works address the vibroacoustic behaviour of a real turboprop fuselage through a high-fidelity FE model supported by structural, acoustic and coupled vibroacoustic validation. This observation motivates the gap addressed in the present work.

1.4.2 Gap and Motivation of the Present Work

Despite the progress discussed in the previous section, several limitations remain when the objective is the development of predictive vibroacoustic tools applicable to real aircraft configurations. A first limitation concerns the geometrical and structural idealisations commonly adopted in numerical models. Many studies rely on simplified fuselage sections, cylindrical shells, isolated panels, representative cabin segments, or reduced structural configurations. These models are valuable for identifying specific transmission mechanisms and for performing parametric analyses; however, they cannot fully reproduce the global vibroacoustic behaviour of a real cockpit–cabin fuselage assembly. In particular, simplified models may neglect the longitudinal continuity of the structure, the interaction between cockpit and passenger-cabin regions, the role of the passenger floor, the actual distribution of frames and stringers, and the influence of local geometrical discontinuities such as windows, doors and emergency exits.

A second limitation concerns the level of structural detail included in the numerical representation. In the low- to mid-frequency range, the vibroacoustic response is governed by a limited number of structural and acoustic modes. As a consequence, the predicted cabin sound field is highly sensitive to the mass and stiffness distribution of the fuselage, to the local arrangement of stiffening members, and to the adopted boundary conditions. Accurate prediction therefore requires high-fidelity structural models able to represent the main load-carrying components of the aircraft, including the skin, frames, stringers, floor structure, bulkheads, window frames and local reinforcements. Excessively simplified structural representations may reproduce general trends, but they are less suitable for predicting local pressure distributions, receiver-dependent variations and modal transmission paths.

A further limitation concerns experimental validation. A substantial part of the available literature remains predominantly numerical, while experimental validation, when present, is often limited to acoustic response quantities, local transfer functions, or simplified test configurations. This is particularly relevant for turboprop aircraft, because the BPF and its lower harmonics generally fall in a frequency range where both the fuselage structure and the cabin cavity exhibit sparse and well-separated modes. In this regime, the predicted interior sound field is strongly affected by the accuracy of the structural modal response, the acoustic modal behaviour and their coupled interaction. A reliable predictive model should therefore be assessed through a progressive validation strategy including structural dynamics, acoustic modal behaviour and coupled vibroacoustic response.

These limitations are particularly relevant for the Piaggio P180 Avanti EVO. The aircraft is characterised by a distinctive rear-mounted pusher-propeller configuration, which generates tonal excitation in a frequency range where individual structural and acoustic modes remain clearly identifiable. Moreover, the cockpit–cabin fuselage assembly includes several geometrical and structural features that are expected to influence the vibroacoustic transmission behaviour, such as the passenger floor, local window cavities, door and emergency-exit regions, frames, stringers and bulkheads. Despite the industrial and aeroacoustic relevance of this configuration, a high-fidelity structural–acoustic FE model of the Piaggio P180 Avanti EVO cockpit–cabin fuselage assembly, supported by structural, acoustic and coupled vibroacoustic validation, is not available in the open literature.

The present thesis addresses this gap by developing a detailed structural–acoustic FE model of the Piaggio P180 Avanti EVO fuselage region relevant to cabin noise transmission. The model is designed to capture the low- to mid-frequency vibroacoustic behaviour associated with the first BPF harmonics and to provide a physically consistent representation of the dominant transmission mechanisms between the external excitation, the fuselage structure and the internal acoustic cavity. The predictive capability of the model is assessed through a progressive validation procedure, including comparison with available structural modal data, acoustic modal verification against analytical reference solutions, preliminary coupled-response verification and numerical–experimental correlation against full-scale cabin NR measurements.

The motivation of the work is therefore twofold. From a methodological perspective, the thesis aims to establish a validated high-fidelity modelling framework for low-frequency cabin-noise prediction in a real turboprop fuselage configuration. From an engineering perspective, the model provides a numerical basis for future analyses involving realistic propeller-induced pressure fields, acoustic-treatment optimisation and passenger-comfort-oriented cabin noise assessment.

1.5 Objectives and Structure of the Thesis

1.5.1 Objectives of the Thesis

The main objective of this thesis is the development and validation of a high-fidelity coupled structural–acoustic FE model of the Piaggio P180 Avanti EVO cockpit–cabin fuselage assembly. The model is intended to reproduce the dominant vibroacoustic transmission mechanisms occurring in the frequency range associated with the first three BPF harmonics of the reference propeller operating condition, where the response is governed by sparse structural and acoustic modes and by strong spatial variability of the internal pressure field.

Within this general objective, the thesis addresses a set of specific research issues. First, it investigates whether a geometrically detailed structural–acoustic FE model can reproduce the dominant low-frequency structural and acoustic modal behaviour of the Piaggio P180 Avanti EVO cockpit–cabin fuselage assembly. Second, it examines how modelling assumptions related to structural idealisation, acoustic-domain definition, excitation area and boundary impedance affect the numerical–experimental correlation of the predicted cabin NR. Third, it assesses the extent to which simplified impedance boundary conditions and equivalent acoustic-treatment representations can reproduce the main trends observed in full-scale experimental data. Finally, it establishes whether the validated model can provide a reliable numerical basis for future analyses involving realistic propeller-induced pressure fields, acoustic treatment optimisation and cabin noise reduction strategies.

To address these research issues, the work pursues the following operational objectives:

1. to develop a geometrically detailed structural FE model of the cockpit–cabin fuselage assembly, including the main load-carrying components, stiffening elements, floor structure, bulkheads, windows and local reinforcements;

2. to define structural and acoustic mesh resolution criteria suitable for modal-based vibroacoustic analysis up to the target frequency range;

3. to verify the acoustic cavity model through comparison with analytical solutions for an equivalent rigid-walled cylindrical cavity;

4. to validate the structural behaviour and coupled vibroacoustic response through comparison with available experimental modal and NR data;

5. to identify the main modelling assumptions and uncertainty sources affecting the predictive capability of the model.

1.5.2 Structure of the Thesis

The structure of the thesis is as follows.

Chapter 1 introduces the problem of turboprop aircraft cabin noise and presents the state of the art on interior noise prediction and control. The research gap and the objectives of the present work are also discussed. Chapter 2 outlines the numerical framework adopted for the analysis of coupled vibroacoustic problems, including the governing equations of the structural and acoustic fields, the fluid–structure coupling conditions and the FE formulation. A modal reduction approach is also introduced to enable efficient frequency-domain simulations. Chapter 3 introduces the aircraft under investigation, the Piaggio P180 Avanti family. The chapter presents the historical development of the aircraft and discusses its main aerodynamic, structural and aero-acoustic characteristics, with particular attention to the relevance of the first three BPF harmonics. Chapter 4 describes the development of the structural–acoustic FE model of the Piaggio P180 Avanti EVO cockpit–cabin fuselage assembly. The structural model is generated from the aircraft CAD geometry and validated through comparison with experimental modal data. The acoustic model of the passenger cabin is then introduced and verified through comparison with analytical solutions for an equivalent cylindrical cavity. The mesh-sizing criteria adopted for both the structural and acoustic domains are also discussed. Chapter 5 presents a preliminary verification of the coupled structural–acoustic model. A forced frequency response analysis is performed on a reduced passenger cabin configuration in order to verify the implementation of the fluid—structure coupling and to assess the physical consistency of the vibroacoustic response in terms of acoustic pressure fields and Noise Reduction. Chapter 6 is devoted to the numerical–experimental validation of the vibroacoustic model. The model is adapted to reproduce a full-scale laboratory acoustic test campaign, and its predictive capability is assessed through comparison with experimental NR data. Both a body-in-white configuration and a configuration with acoustic treatment are considered. Chapter 7 summarizes the main findings of the thesis and outlines possible directions for future research, including the extension of the validated framework to realistic propeller-induced pressure fields and cabin NR studies.

Chapter 2

Governing Equations and Numerical Formulation of Vibroacoustic Problems

This chapter introduces the analytical and numerical formulation adopted for the structural–acoustic analyses performed in this thesis. The formulation provides the basis for the construction of the structural and acoustic models described in Chapter 4, the coupled-response verification discussed in Chapter 5, and the full-scale numerical–experimental validation presented in Chapter 6.

The vibroacoustic problem consists of the interaction between a fluid domain and a structural domain, coupled at their common interface. Following the formulation presented in [67], the fluid–structure interaction problem is illustrated in Fig. 2.1. The structural domain is denoted by Ω_s, while its boundary is partitioned into a portion Σ_s where external loads are prescribed and a portion Σ_u where displacements are imposed, such that

$$\partial\Omega_s = \Sigma_s \cup \Sigma_u \tag{2.1}$$

The fluid domain is denoted by Ω_f, whose boundary includes a portion Σ_w where a normal velocity is prescribed. The interface between the fluid and the structure is denoted by Σ_i.

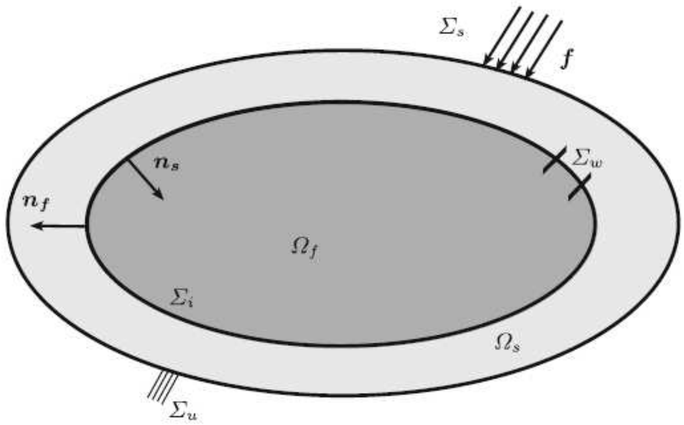

Fig. 2.1 Schematic representation of the vibroacoustic coupling between fluid and structural domains.

The vectors $\mathbf{n}_s$ and $\mathbf{n}_f$ denote the outward normal directions to the structural and fluid domains, respectively, and $\mathbf{f}$ represents the prescribed surface traction acting on Σ_s.

In the following, the governing equations of the acoustic and structural fields are first introduced, together with the coupling conditions at the interface. Subsequently, a numerical formulation based on the weak form of the coupled problem is derived, leading to its finite element discretisation and matrix representation.

2.1 Governing Equations

2.1.1 Acoustic Field

In linear acoustics, sound is described as a small perturbation of the equilibrium state of a compressible, homogeneous, and inviscid fluid initially at rest.

Assuming the presence of small-amplitude acoustic waves in a quiescent medium ($\mathbf{v}_0 = 0$), characterised by an equilibrium pressure p_0 and density ρ_0, the acoustic field variables can be decomposed into a steady component and a fluctuating contribution:

$$\begin{cases} \mathbf{v}(\mathbf{x}, t) = \mathbf{v}'(\mathbf{x}, t), \\ p(\mathbf{x}, t) = p_0 + p'(\mathbf{x}, t), \\ \rho(\mathbf{x}, t) = \rho_0 + \rho'(\mathbf{x}, t). \end{cases} \tag{2.2}$$

Here, $\mathbf{x} = (x, y, z)$ denotes the spatial position, while p', ρ', and $\mathbf{v}'$ denote the acoustic pressure fluctuation, density fluctuation, and particle velocity, respectively.

Under the assumption of infinitesimal perturbations, nonlinear terms of higher-order can be neglected. Within this linearised framework, the conservation of mass yields the continuity equation:

$$\frac{\partial \rho'}{\partial t} + \rho_0 \nabla \cdot \mathbf{v}' = 0 \tag{2.3}$$

while the conservation of momentum for an inviscid fluid leads to the linearised Euler equation:

$$\rho_0 \frac{\partial \mathbf{v}'}{\partial t} + \nabla p' = 0 \tag{2.4}$$

Equations 2.3 and 2.4 constitute the fundamental set governing the propagation of small acoustic disturbances in the fluid.

By taking the time derivative of Eq. 2.3 and the divergence of Eq. 2.4 and then subtracting the resulting expressions, an intermediate relation involving both pressure and density fluctuations is obtained:

$$\nabla^2 p' - \frac{\partial^2 \rho'}{\partial t^2} = 0 \tag{2.5}$$

To close the system, a thermodynamic relation between pressure and density fluctuations is required. Assuming adiabatic acoustic transformations, the state equation for a perfect gas can be linearised about the equilibrium state, leading to:

$$\frac{\partial p}{\partial \rho} = \frac{p_0}{\rho_0} k = c_0^2 \tag{2.6}$$

where c_0 denotes the speed of sound in the fluid. Linearization of the equation of state about the equilibrium condition yields:

$$p' = c_0^2 \rho' \tag{2.7}$$

Substituting into Eq. 2.5, the classical acoustic wave equation in the time domain is obtained:

$$\nabla^2 p' = \frac{1}{c_0^2} \frac{\partial^2 p'}{\partial t^2} \tag{2.8}$$

In vibroacoustic applications, it is often convenient to formulate the problem in the frequency domain by assuming a harmonic time dependence of the acoustic pressure field:

$$p'(\mathbf{x}, t) = p(\mathbf{x}) e^{i\omega t} \tag{2.9}$$

where $p(\mathbf{x})$ denotes the complex amplitude of the acoustic pressure field and ω is the angular frequency. In the following, the time dependence is omitted and the pressure field is denoted simply by p.

Substituting this expression into Eq. 2.8, one finally obtains the Helmholtz equation in the absence of external acoustic sources within the fluid domain:

$$\nabla^2 p + \frac{\omega^2}{c_0^2} p = 0 \quad \text{in } \Omega_f \tag{2.10}$$

which governs the spatial distribution of the acoustic pressure field in the frequency domain and defines the acoustic problem to be solved.

Acoustic Boundary Conditions

In order to obtain a well-posed acoustic problem, appropriate boundary conditions must be specified on the boundary of the fluid domain. These conditions describe the interaction between the acoustic field and the surrounding environment, such as rigid walls, vibrating structures, or absorbing materials.

The linearised momentum equation provides a relation between the pressure gradient and the particle acceleration. By projecting the momentum equation onto the outward normal direction $\mathbf{n}_f$ of the boundary surface, one obtains:

$$\rho_f \frac{\partial v_n}{\partial t} + \frac{\partial p}{\partial n_f} = 0 \tag{2.11}$$

where $v_n = \mathbf{v} \cdot \mathbf{n}_f$ denotes the normal component of the particle velocity. From this point onward, the fluid density is denoted by ρ_f, corresponding to the equilibrium density ρ_0 introduced in the linearised formulation.

Assuming harmonic time dependence, the normal component of the particle velocity can be expressed as

$$v_n(\mathbf{x}, t) = \hat{v}_n(\mathbf{x}) e^{i\omega t} \tag{2.12}$$

which implies

$$\frac{\partial v_n}{\partial t} = i\omega v_n \tag{2.13}$$

Substituting into Eq. 2.11, the following general boundary relation is obtained:

$$\frac{\partial p}{\partial n_f} = -i\omega \rho_f v_n \tag{2.14}$$

Rigid Wall Boundary Condition For an acoustically rigid boundary, the normal component of the particle velocity vanishes ($v_n = 0$). In this case, Eq. 2.14 reduces to:

$$\frac{\partial p}{\partial n_f} = 0 \tag{2.15}$$

This condition corresponds to a Neumann boundary condition and represents a perfectly reflecting surface.

Impedance Boundary Condition In many practical applications, boundaries deviate from the ideal perfectly reflecting behaviour and exhibit partial reflection of acoustic energy, accompanied by dissipation effects. This behaviour can be modelled through an acoustic impedance Z, defined as the ratio between acoustic pressure and normal particle velocity:

$$Z = \frac{p}{v_n} \tag{2.16}$$

Substituting into Eq. 2.14, the impedance boundary condition is obtained:

$$\frac{\partial p}{\partial n_f} = -i\omega\rho_f \frac{p}{Z} \tag{2.17}$$

This condition represents a Robin-type boundary condition, involving a linear combination of the acoustic pressure and its normal derivative.

Prescribed Pressure Boundary Condition In some cases, the acoustic pressure is directly imposed on the boundary, leading to a Dirichlet condition of the form:

$$p = \bar{p} \tag{2.18}$$

where $\bar{p}$ is a prescribed pressure value.

Acoustic Sources Acoustic sources can be introduced either as boundary conditions or as source terms within the domain. In the present formulation, they are typically represented through prescribed pressure or normal velocity conditions on the boundary.

2.1.2 Structural Field

The structural field is governed by the balance of linear momentum. Its integral form can be written as

$$\int_V \mathbf{b}\, dV + \int_S \mathbf{T}\, dS = \int_V \rho_s \mathbf{a}\, dV \tag{2.19}$$

where $\mathbf{b}$ denotes the body force per unit volume, $\mathbf{T}$ the surface traction vector, and $\mathbf{a}$ the acceleration field.

The corresponding local form of the momentum balance is expressed as

$$\rho_s \frac{\partial^2 \boldsymbol{u}}{\partial t^2} = \nabla \cdot \boldsymbol{\sigma} + \mathbf{b} \quad \text{in } \Omega_s \tag{2.20}$$

where $\boldsymbol{u}$ is the displacement field and $\boldsymbol{\sigma}$ is the Cauchy stress tensor.

Assuming linear elastic material behaviour, the constitutive relation is given by Hooke's law:

$$\boldsymbol{\sigma} = \mathbf{C} : \boldsymbol{\varepsilon} \quad \text{in } \Omega_s \tag{2.21}$$

where $\mathbf{C}$ denotes the fourth-order elasticity tensor and $\boldsymbol{\varepsilon}$ is the strain tensor defined as

$$\boldsymbol{\varepsilon} = \frac{1}{2}\left(\nabla \boldsymbol{u} + \nabla \boldsymbol{u}^T\right) \quad \text{in } \Omega_s \tag{2.22}$$

Substituting the constitutive relation into Eq. 2.20 yields the governing equation in terms of the displacement field:

$$\rho_s \frac{\partial^2 \boldsymbol{u}}{\partial t^2} = \nabla \cdot (\mathbf{C} : \boldsymbol{\varepsilon}) + \mathbf{b} \tag{2.23}$$

In vibroacoustic applications, a frequency-domain formulation is typically adopted by assuming harmonic time dependence:

$$\boldsymbol{u}(\mathbf{x}, t) = \boldsymbol{u}(\mathbf{x}) e^{i\omega t} \tag{2.24}$$

where $\boldsymbol{u}(\mathbf{x})$ denotes the complex amplitude of the continuous displacement field. In the following, the time dependence is omitted and the continuous displacement field is denoted by $\boldsymbol{u}$.

Substituting this expression into Eq. 2.20 yields the structural equilibrium equation in the frequency domain:

$$-\omega^2 \rho_s \boldsymbol{u} = \nabla \cdot \boldsymbol{\sigma} + \mathbf{b} \tag{2.25}$$

Structural Boundary Conditions

Referring to Fig. 2.1, the boundary of the structural domain can be decomposed into two complementary parts: a portion Σ_u where displacements are prescribed, and a portion Σ_s where tractions are applied.

Prescribed Displacement On Σ_u, the displacement field is imposed:

$$\boldsymbol{u} = \bar{\boldsymbol{u}} \quad \text{on } \Sigma_u \tag{2.26}$$

This condition represents a Dirichlet boundary condition.

Prescribed Traction On Σ_s, the surface traction vector is prescribed:

$$\boldsymbol{\sigma} \mathbf{n}_s = \mathbf{f} \quad \text{on } \Sigma_s \tag{2.27}$$

where $\mathbf{n}_s$ denotes the outward normal to the structural domain and $\mathbf{f}$ is the prescribed surface traction vector introduced in Fig. 2.1, coinciding with the surface traction vector $\mathbf{T}$ appearing in Eq. 2.19.

This condition corresponds to a Neumann-type boundary condition and represents externally applied surface forces.

2.1.3 Vibroacoustic Coupling

Referring to Fig. 2.1, the interaction between the fluid and structural domains occurs at the common interface Σ_i. At this interface, suitable continuity conditions must be enforced to ensure a physically consistent exchange of energy between the two media. These conditions express the continuity of normal velocity and the equilibrium of normal stresses.

Kinematic condition At the interface Σ_i, the normal component of the fluid particle velocity must coincide with the normal velocity of the structure:

$$v_n = \frac{\partial u_n}{\partial t} \tag{2.28}$$

Assuming harmonic time dependence, this condition becomes

$$v_n = i\omega u_n \tag{2.29}$$

where $v_n = \mathbf{v} \cdot \mathbf{n}_f$ denotes the normal component of the fluid particle velocity, and $u_n = \boldsymbol{u} \cdot \mathbf{n}_s$ denotes the normal component of the structural displacement.

Dynamic condition The equilibrium of forces at the interface requires that the normal stress in the structure balances the acoustic pressure exerted by the fluid:

$$\boldsymbol{\sigma}\mathbf{n}_s = -p\mathbf{n}_s \quad \text{on } \Sigma_i \tag{2.30}$$

This condition expresses the continuity of normal stresses across the interface.

Coupled boundary condition By substituting the kinematic condition (Eq. 2.29) into the acoustic boundary relation (Eq. 2.14), the following coupling condition is obtained:

$$\frac{\partial p}{\partial n_f} = -i\omega \rho_f v_n = \omega^2 \rho_f u_n \quad \text{on } \Sigma_i \tag{2.31}$$

Equation 2.31 can be equivalently written in compact form as

$$\nabla p \cdot \mathbf{n}_f - \rho_f \omega^2 \, \boldsymbol{u} \cdot \mathbf{n}_f = 0 \quad \text{on } \Sigma_i \tag{2.32}$$

The coupled vibroacoustic problem is therefore defined by the Helmholtz equation in the fluid domain Ω_f, the structural equilibrium equation in the solid domain Ω_s, and the interface conditions given by Eqs. 2.29–2.31.

2.2 Numerical Formulation

2.2.1 Weak Formulation

The weak formulation of the coupled vibroacoustic problem is derived starting from the governing equations of the structural and acoustic fields together with the interface coupling conditions.

Let $\delta \boldsymbol{u} \in C_u$ and $\delta p \in C_p$ denote admissible virtual displacement and pressure fields, respectively, where C_u and C_p are function spaces of sufficiently regular functions. In particular, the virtual displacement field satisfies $\delta \boldsymbol{u} = 0$ on Σ_u.

Structural field Multiplying the structural equilibrium equation (Eq. 2.25), assuming vanishing body forces ($\mathbf{b} = \mathbf{0}$), by the virtual displacement $\delta \boldsymbol{u}$ and integrating over the structural domain Ω_s, the following expression is obtained:

$$\int_{\Omega_s} \delta \boldsymbol{u} \cdot \left(-\omega^2 \rho_s \boldsymbol{u}\right) d\Omega = \int_{\Omega_s} \delta \boldsymbol{u} \cdot (\nabla \cdot \boldsymbol{\sigma})\, d\Omega \tag{2.33}$$

Applying integration by parts and introducing the strain tensor, the weak form becomes:

$$k(\boldsymbol{u}, \delta \boldsymbol{u}) - \omega^2 m(\boldsymbol{u}, \delta \boldsymbol{u}) - c(p, \delta \boldsymbol{u}) - f(\delta \boldsymbol{u}) = 0, \qquad \forall\, \delta \boldsymbol{u} \in C_u \tag{2.34}$$

Acoustic field Starting from the Helmholtz equation (Eq. 2.10), multiplying by the virtual pressure δp and integrating over the fluid domain Ω_f:

$$\int_{\Omega_f} \delta p \left(\nabla^2 p + \frac{\omega^2}{c_0^2} p\right) d\Omega = 0 \tag{2.35}$$

Applying integration by parts leads to:

$$h(p, \delta p) - \omega^2 q(p, \delta p) - \omega^2 \rho_f\, c(\delta p, \boldsymbol{u}) = 0, \qquad \forall\, \delta p \in C_p \tag{2.36}$$

The terms appearing in Eqs. 2.34–2.36 are defined as follows:

$$k(\boldsymbol{u}, \delta \boldsymbol{u}) = \int_{\Omega_s} \boldsymbol{\varepsilon}(\delta \boldsymbol{u}) : \mathbf{C} : \boldsymbol{\varepsilon}(\boldsymbol{u}) \, dV \tag{2.37}$$

$$m(\boldsymbol{u}, \delta \boldsymbol{u}) = \int_{\Omega_s} \rho_s \, \delta \boldsymbol{u} \cdot \boldsymbol{u} \, dV \tag{2.38}$$

$$c(p, \delta \boldsymbol{u}) = \int_{\Sigma_i} \delta \boldsymbol{u} \cdot p \, \mathbf{n}_s \, dS \tag{2.39}$$

$$f(\delta \boldsymbol{u}) = \int_{\Sigma_s} \delta \boldsymbol{u} \cdot \mathbf{f} \, dS \tag{2.40}$$

$$h(p, \delta p) = \int_{\Omega_f} \nabla \delta p \cdot \nabla p \, dV \tag{2.41}$$

$$q(p, \delta p) = \int_{\Omega_f} \frac{1}{c_0^2} \, p \, \delta p \, dV \tag{2.42}$$

$$c(\delta p, \boldsymbol{u}) = \int_{\Sigma_i} \boldsymbol{u} \cdot \delta p \, \mathbf{n}_f \, dS \tag{2.43}$$

The terms $k(\boldsymbol{u}, \delta \boldsymbol{u})$ and $m(\boldsymbol{u}, \delta \boldsymbol{u})$ represent the virtual structural potential energy and virtual structural kinetic energy, respectively, while $h(p, \delta p)$ and $q(p, \delta p)$ correspond to the virtual acoustic potential energy and virtual acoustic kinetic energy, respectively. The terms $c(p, \delta \boldsymbol{u})$ and $c(\delta p, \boldsymbol{u})$ describe the virtual coupling energy for the structural side and the virtual coupling energy for the acoustic side, respectively. The term $f(\delta \boldsymbol{u})$ is the virtual structural external energy.

The weak formulation defined by Eqs. 2.34–2.36 constitutes the basis for the finite element discretisation of the coupled vibroacoustic problem.

2.2.2 Finite Element Discretisation for Vibroacoustic System

The finite element formulation is obtained by introducing the finite element approximations of the continuous displacement and pressure fields, denoted by $\boldsymbol{u}^h$ and p^h, together with the related virtual fields $\delta \boldsymbol{u}^h$ and δp^h:

$$\boldsymbol{u}^h = \mathbf{N}_s \mathbf{u}, \qquad \delta \boldsymbol{u}^h = \mathbf{N}_s \, \delta \mathbf{u} \tag{2.44}$$

$$p^h = \mathbf{N}_f \mathbf{p}, \qquad \delta p^h = \mathbf{N}_f \, \delta \mathbf{p} \tag{2.45}$$

where $\mathbf{N}_s$ and $\mathbf{N}_f$ are the matrices of finite element shape functions for the structural and acoustic domains, respectively, and $\mathbf{u}$ and $\mathbf{p}$ collect the corresponding unknown nodal values.

Substituting these approximations into the weak formulation and exploiting the arbitrariness of the virtual fields, the problem can be expressed in terms of discrete operators.

The structural contributions lead to:

$$k(\boldsymbol{u}^h, \delta \boldsymbol{u}^h) = \delta \mathbf{u}^T \mathbf{K} \mathbf{u} \tag{2.46}$$

$$m(\boldsymbol{u}^h, \delta \boldsymbol{u}^h) = \delta \mathbf{u}^T \mathbf{M} \mathbf{u} \tag{2.47}$$

The coupling term at the interface becomes:

$$c(p^h, \delta \boldsymbol{u}^h) = \delta \mathbf{u}^T \mathbf{C} \mathbf{p} \tag{2.48}$$

while the external force contribution is written as:

$$f(\delta \boldsymbol{u}^h) = \delta \mathbf{u}^T \mathbf{f} \tag{2.49}$$

Similarly, for the acoustic field, one obtains:

$$h(p^h, \delta p^h) = \delta \mathbf{p}^T \mathbf{H} \mathbf{p} \tag{2.50}$$

$$q(p^h, \delta p^h) = \delta \mathbf{p}^T \mathbf{Q} \mathbf{p} \tag{2.51}$$

where $\mathbf{K}$ and $\mathbf{M}$ are the structural stiffness and mass matrices, $\mathbf{H}$ and $\mathbf{Q}$ are the acoustic stiffness and mass matrices, and $\mathbf{C}$ is the coupling matrix arising from the fluid–structure interaction at the interface and $\mathbf{f}$ is the vector of equivalent nodal forces associated with the prescribed surface tractions.

The matrices $\mathbf{K}$ and $\mathbf{H}$ are positive semi-definite. In particular, the kernel of $\mathbf{K}$ has dimension six in three-dimensional problems, corresponding to the rigid body motions of the structure, while the kernel of $\mathbf{H}$ has dimension one, associated with constant pressure fields. The mass matrix $\mathbf{M}$ is positive definite.

Collecting all contributions, the coupled vibroacoustic problem can be written in matrix form as:

$$\begin{bmatrix} \mathbf{K} & -\mathbf{C} \\ \mathbf{0} & \mathbf{H} \end{bmatrix} \begin{bmatrix} \mathbf{u} \\ \mathbf{p} \end{bmatrix} - \omega^2 \begin{bmatrix} \mathbf{M} & \mathbf{0} \\ \rho_f \mathbf{C}^T & \mathbf{Q} \end{bmatrix} \begin{bmatrix} \mathbf{u} \\ \mathbf{p} \end{bmatrix} = \begin{bmatrix} \mathbf{f} \\ \mathbf{0} \end{bmatrix} \tag{2.52}$$

Numerical integration is performed using Gaussian quadrature, which provides an approximate evaluation of the integrals arising in the finite element formulation. The number of integration points is chosen according to the polynomial order of the interpolation functions. Further details can be found in [68].

2.2.3 Reduced-Order Model by Projection onto Modal Basis

In order to reduce the computational cost associated with the solution of the full vibroacoustic system, a reduced-order model is constructed by projecting the problem onto a modal basis. In this framework, the system response is approximated as a linear combination of a limited number of structural and acoustic modes.

The reduction is performed by considering the modal properties of the decoupled systems: the structural modes are computed in vacuo, while the acoustic modes are obtained in the fluid domain with rigid boundary conditions at the interface [69, 70]. This leads to the solution of two independent eigenvalue problems. For the structural domain, the following generalized eigenvalue problem is solved:

$$\left(\mathbf{K} - \omega^2 \mathbf{M}\right) \boldsymbol{\phi}^s = \mathbf{0} \tag{2.53}$$

Similarly, for the acoustic domain, one obtains:

$$\left(\mathbf{H} - \omega^2 \mathbf{Q}\right) \boldsymbol{\phi}^f = \mathbf{0} \tag{2.54}$$

In both eigenvalue problems, the stiffness and mass matrices are symmetric, as they arise from symmetric bilinear forms in the weak formulation. This ensures that the eigenvalue problems are well-posed and admit real eigenvalues and orthogonal eigenvectors.

The solution of these eigenvalue problems provides the structural and acoustic eigenvectors and eigenfrequencies:

$$\boldsymbol{\Phi}_s = \begin{bmatrix} \vdots & & \vdots \\ \boldsymbol{\phi}_1^s & \cdots & \boldsymbol{\phi}_{m_s}^s \\ \vdots & & \vdots \end{bmatrix}_{(n_s \times m_s)} \qquad \text{and} \qquad \boldsymbol{\omega}_s = \begin{bmatrix} \vdots \\ \omega_i^s \\ \vdots \end{bmatrix}_{(m_s \times 1)} \tag{2.55}$$

$$\boldsymbol{\Phi}_f = \begin{bmatrix} \vdots & & \vdots \\ \boldsymbol{\phi}_1^f & \cdots & \boldsymbol{\phi}_{m_f}^f \\ \vdots & & \vdots \end{bmatrix}_{(n_f \times m_f)} \qquad \text{and} \qquad \boldsymbol{\omega}_f = \begin{bmatrix} \vdots \\ \omega_i^f \\ \vdots \end{bmatrix}_{(m_f \times 1)} \tag{2.56}$$

where n_s and n_f denote the number of structural and acoustic degrees of freedom of the system, respectively, while m_s and m_f denote the number of retained structural and acoustic modes used to construct the reduced modal bases.

The discrete displacement and pressure vectors are then approximated by projection onto the reduced modal bases:

$$\mathbf{u} \approx \boldsymbol{\Phi}_s \boldsymbol{\alpha}, \qquad \mathbf{p} \approx \boldsymbol{\Phi}_f \boldsymbol{\beta} \tag{2.57}$$

where $\boldsymbol{\alpha}$ and $\boldsymbol{\beta}$ are the vectors of generalized modal coordinates.

Substituting Eq. 2.57 into Eq. 2.52, the following fully coupled reduced-order system is obtained:

$$\begin{bmatrix} \mathbf{K}_r & -\mathbf{C}_r \\ \mathbf{0} & \mathbf{H}_r \end{bmatrix} \begin{bmatrix} \boldsymbol{\alpha} \\ \boldsymbol{\beta} \end{bmatrix} - \omega^2 \begin{bmatrix} \mathbf{M}_r & \mathbf{0} \\ \rho_f \mathbf{C}_r^T & \mathbf{Q}_r \end{bmatrix} \begin{bmatrix} \boldsymbol{\alpha} \\ \boldsymbol{\beta} \end{bmatrix} = \begin{bmatrix} \mathbf{f}_r \\ \mathbf{0} \end{bmatrix} \tag{2.58}$$

where the reduced matrices are defined as:

$$\mathbf{K}_r = \boldsymbol{\Phi}_s^T \mathbf{K} \boldsymbol{\Phi}_s, \qquad \mathbf{M}_r = \boldsymbol{\Phi}_s^T \mathbf{M} \boldsymbol{\Phi}_s \tag{2.59}$$

$$\mathbf{H}_r = \boldsymbol{\Phi}_f^T \mathbf{H} \boldsymbol{\Phi}_f, \qquad \mathbf{Q}_r = \boldsymbol{\Phi}_f^T \mathbf{Q} \boldsymbol{\Phi}_f \tag{2.60}$$

$$\mathbf{C}_r = \boldsymbol{\Phi}_s^T \mathbf{C} \boldsymbol{\Phi}_f \tag{2.61}$$

$$\mathbf{f}_r = \boldsymbol{\Phi}_s^T \mathbf{f} \tag{2.62}$$

The resulting system has a significantly reduced size compared to the original one, since $m_s \ll n_s$ and $m_f \ll n_f$. This allows for a substantial reduction in computational cost while retaining the dominant dynamic behaviour of the coupled system. The reduced-order model is then used to compute the forced vibroacoustic response for a prescribed excitation frequency ω. The solution is expressed in terms of the generalized modal coordinates $\boldsymbol{\alpha}$ and $\boldsymbol{\beta}$, which describe the contribution of the retained structural and acoustic modes to the overall system response.

Once the modal coordinates are determined, the physical displacement and pressure fields can be reconstructed through the modal expansions given in Eq. 2.57. This approach enables an efficient evaluation of the coupled vibroacoustic response over a range of excitation frequencies while significantly reducing the computational cost compared to the full-order model. The accuracy of the reduced-order vibroacoustic model strongly depends on the number of retained structural and acoustic modes. In modal-based frequency response analyses, the truncation frequency of the modal basis is typically selected above the highest excitation or response frequency of interest. In engineering practice, a commonly adopted guideline is to retain modes up to approximately 1.5–2 times the maximum analysis frequency, in order to achieve a satisfactory compromise between computational efficiency and solution accuracy [71]. This choice allows one to account for the influence of higher-frequency modes on the dynamic response within the frequency band of interest.

2.3 Numerical Implementation in MSC Nastran

The formulation presented in the previous sections is implemented in this thesis within the MSC Nastran FE environment.

Structural eigenvalue analyses are performed using SOL 103, while acoustic modal analyses are carried out using SOL 107/SEMODES under rigid-wall boundary conditions. A Lanczos-based eigenvalue extraction is adopted for the modal analyses, allowing the retained structural and acoustic modes to be computed within the prescribed frequency range.

The coupled structural–acoustic frequency-response analyses are performed using SOL 111. A modal superposition strategy is adopted in order to reduce the computational cost associated with the solution of the full coupled system. In this approach, the response is expressed in terms of retained structural and acoustic eigenvectors, consistently with the projection procedure described in Section 2.2.3. The full physical model is used to compute the uncoupled structural and acoustic modal bases, whereas the forced coupled vibroacoustic response is evaluated in the reduced modal space. All coupled structural–acoustic frequency-response results presented in Chapters 5 and 6 are obtained using this modal superposition approach. The number of retained modes is selected so that the modal basis extends beyond the maximum excitation frequency of interest. In the analyses presented in this thesis, a frequency margin is introduced by retaining modes up to approximately twice the maximum forcing frequency, in order to limit modal truncation effects. A sensitivity assessment of the modal truncation frequency is reported in Chapter 6, where the influence of the retained modal basis on the predicted NR response is evaluated for representative validation cases.

The coupling between the structural and acoustic domains is enforced at the common fluid–structure interfaces. In the present model, a one-to-one correspondence between structural and acoustic nodes is adopted along these interfaces. This modelling choice provides a geometrically consistent structural–acoustic connection and minimises interpolation-related uncertainties in the transfer of interface quantities.

Damping is introduced through a modal damping representation. A constant modal damping ratio of 2% is adopted in all frequency-response analyses as a simplified assumption for the lightly damped aircraft structure, consistently with common practice in modal-based airframe vibration analyses [72–74].

When acoustic absorbing materials are included in the numerical model, their effect is represented through equivalent impedance boundary conditions applied to selected acoustic cavity surfaces. In MSC Nastran, these boundary conditions are introduced through the `CAABSF`, which allows the acoustic surface impedance to be assigned to the boundary of the fluid domain without explicitly modelling the porous material volume [75].

Chapter 3

Piaggio P180: An Iconic Aircraft

This chapter introduces the Piaggio P180 Avanti EVO as the aircraft case study considered in this thesis. The discussion focuses on the aerodynamic, structural and acoustic features that are directly relevant to the development of a high-fidelity vibroacoustic model. Particular attention is devoted to the three-lifting-surface configuration, the rear-mounted pusher-propeller arrangement, the lightweight pressurised fuselage and the tonal excitation mechanisms associated with the BPF harmonics.

The Piaggio P180 Avanti project originated in 1979, in the aftermath of the 1970s oil crises, with the objective of engineering a *JetProp* aircraft capable of achieving jet-category cruise speeds while maintaining the fuel economy of a twin-engine turboprop. At a time when fuel efficiency had become a central design concern, Piaggio Chief Designer Alessandro Mazzoni proposed an unconventional aircraft architecture aimed at combining high aerodynamic efficiency, short take-off and landing capability, cabin comfort and reduced interior noise.

A key element of this design philosophy was the Three-Lifting-Surface Configuration (3LSC), patented by Mazzoni. The configuration consists of an unconventional aerodynamic layout featuring a forward canard wing, a mid-mounted main wing, and a conventional T-tail horizontal stabiliser. This arrangement, combined with rear-mounted pusher propellers, was intended to reduce aerodynamic drag, preserve a spacious cabin layout and improve the

Fig. 3.1 P180 prototype aircraft in commemorative livery during the one-million fleet flight hours celebration.

internal acoustic environment by locating the main propulsion noise sources aft of the pressurised passenger compartment.

The project initially involved a 50% partnership with Gates Learjet Company in 1982, and the aircraft was commercially named “Avanti”. Owing to its unconventional aerodynamic configuration, an extensive experimental campaign was conducted, including more than 5.000 hours of wind tunnel testing in both U.S. and Italian facilities. After the withdrawal of Gates Learjet in 1985, Piaggio continued the program independently. The first prototype was rolled out in April 1986 and performed its maiden flight in September of the same year. Following a comprehensive flight-test and certification campaign, the aircraft obtained Italian certification in March 1990 and FAA certification shortly thereafter [76]. The early commercial reception of the aircraft was affected by a change in the economic context. By the time the P180 entered the market, fuel-price pressure had eased and many business-aviation operators were increasingly oriented toward light jets, despite their higher fuel consumption. This unfavourable market timing, together with the large investment required by the programme, placed significant financial pressure on Piaggio. The company entered receivership in 1994 and filed for bankruptcy in 1998. In the same year, a consortium led by the Ferrari and Di Mase families acquired the assets of IAM Rinaldo Piaggio, allowing the company to re-emerge as Piaggio Aero Industries SpA.

In the following years, the original design philosophy of the Avanti became increasingly aligned with renewed interest in fuel-efficient aircraft. Rising operating costs, environmental concerns and the need to combine high cruise speed with reduced fuel consumption contributed to restoring the competitiveness of the platform. In this context, the Avanti came to be recognised as one of the "greenest" aircraft in the business-aviation segment, combining near-jet performance with markedly lower environmental impact [77].

Over time, the P180 platform evolved through three main production variants: the original P180 Avanti, the Avanti II and the Avanti EVO. The operational maturity of the platform is confirmed by a significant milestone: in December 2020, the global fleet surpassed one million flight hours, as shown in Fig. 3.1 [78].

More recently, after several years under extraordinary administration, Piaggio Aerospace entered a new industrial phase following its acquisition by Baykar Technologies. The new ownership has announced plans to relaunch the P180 programme through investments in production and maintenance capabilities, including an increase in production rate, the development of an updated version known as the Avanti NX, and the strengthening of the global maintenance, repair and overhaul network [79, 80].

3.1 Three-Lifting-Surface Concept

In the late 1970s, Alessandro Mazzoni recognised that, given the technological limitations of contemporary turboprop engines, significant performance improvements could not be achieved through propulsion alone. Instead, achieving higher cruise speeds and improved fuel efficiency required a substantial reduction in aerodynamic drag. This consideration became one of the central design drivers of the P180 Avanti. The solution proposed by Mazzoni was an unconventional aerodynamic layout known as the Three-Lifting-Surface Configuration. The concept departs from traditional aircraft architectures by distributing lift generation across three distinct surfaces: a forward canard wing, a high-aspect-ratio main wing, and a small horizontal stabiliser atop the conventional vertical stabiliser.

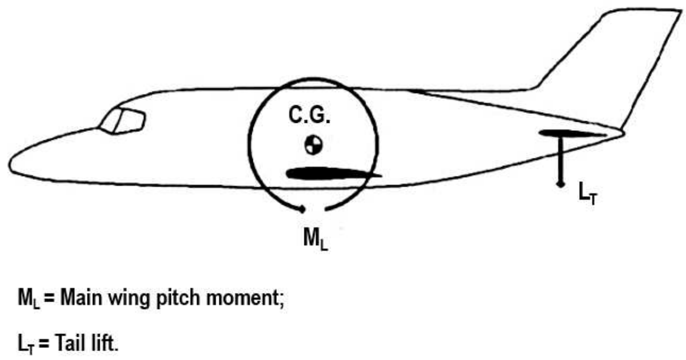

Fig. 3.2 Conventional two-surface configuration lift balance. M_L denotes the nose-down pitching moment generated by the main wing lift, while L_T represents the negative lift produced by the horizontal tail to balance M_L moment.

As shown in Fig. 3.2, in conventional two-surface configurations, the lift produced by the main wing generates a nose-down pitching moment due to the aft position of the aerodynamic centre relative to the centre of gravity (C.G.). This moment is typically balanced by a downward force generated by the horizontal stabiliser, often referred to as "negative lift". This trim force can reach up to 10% of the aircraft weight in cruise and up to 20% during approach. As a consequence, the main wing must generate additional lift, supporting up to 110–120% of the aircraft weight. This results in increased induced drag, larger wing area, and higher structural weight.

In contrast, the 3LSC configuration of the Avanti significantly reduces these penalties (Fig. 3.3). As shown in Fig. 3.3a, the forward wing produces positive lift that counterbalances the nose-down pitching moment generated by the main wing. As a result, the horizontal tail produces negligible lift in cruise conditions, and the total lift generated by the aircraft is approximately equal to its weight. This leads to a reduction in required wing area, induced drag, profile drag, and structural weight. Although the horizontal tail may still generate a limited amount of negative lift in certain flight conditions, the resulting penalties in terms of drag and structural weight are marginal, while the improvements in controllability are considerable.

An additional advantage of the forward wing lies in its aerodynamic design, particularly its incidence angle, which is selected such that it stalls prior to the

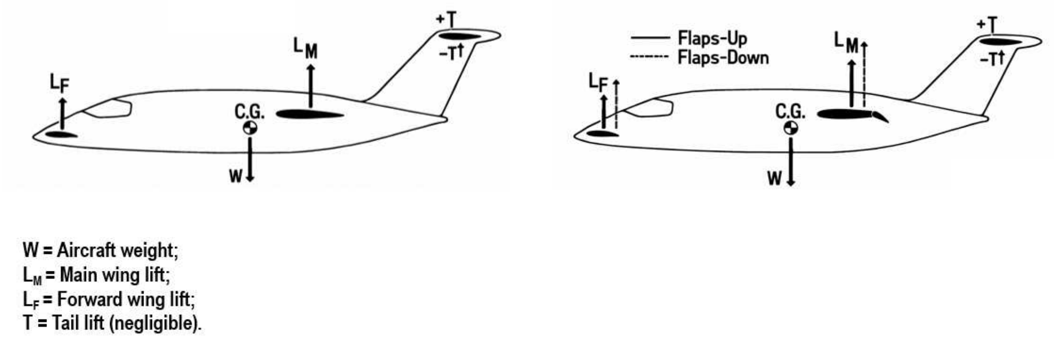

(a) Cruise configuration. (b) Flap deployment.

Fig. 3.3 Three-surface configuration lift balance under different flight conditions. In cruise (left), the total lift is shared between the forward wing (L_F) and the main wing (L_M), while the horizontal tail contribution (T) is negligible. When the main wing flaps are deployed (right), the increase in lift and the rearward shift of the centre of pressure generate a higher nose-down pitching moment, which is compensated by additional positive lift produced by the forward wing.

main wing. When the forward wing reaches its stall condition, the resulting loss of lift at the front generates an inherent nose-down pitching moment, thereby promoting natural stall recovery and enhancing flight safety.
In addition, the aircraft is equipped with twin fixed ventral stabilising fins located on the aft fuselage. These fins contribute to a stabilising nose-down pitching moment and improve lateral-directional stability by mitigating yawing tendencies at high angles of attack.

The forward wing is equipped with flaps that are scheduled to deploy in coordination with the main wing flaps. During takeoff and landing, when the main wing flaps increase lift and shift the centre of pressure aft, the forward wing flaps are electronically programmed to extend in concert with the main wing flaps, providing the precise amount of additional up-lift needed to balance the aftward movement of the main wing's centre of lift (Fig. 3.3b).

Mazzoni was well aware that, although the forward wing contributes to pitch balance, the use of a canard as a primary lifting surface may lead to reduced longitudinal stability. For this reason, the Avanti retains a conventional horizontal stabiliser with elevator, ensuring precise pitch control and handling qualities comparable to those of traditional aircraft configurations. As a result, the aircraft exhibits conventional and predictable stall behaviour without requiring artificial stall protection systems such as stick-pushers or stick-shakers.

From the viewpoint of the present thesis, the relevance of the 3LSC is not limited to aerodynamic efficiency and stability. Together with the fuselage and engine installation, the forward and main wings contribute to the non-uniform inflow experienced by the rear-mounted pusher propellers. This wake–propeller interaction can modify the tonal content associated with the BPF and its harmonics, making the P180 a particularly relevant aircraft for vibroacoustic modelling in the low- to mid-frequency range. Therefore, the same aerodynamic architecture that contributes to the high efficiency of the P180 also plays a role in its distinctive aeroacoustic behaviour.

3.2 Airframe Design and Manufacturing

The Piaggio P180 Avanti features an advanced airframe design that combines aerodynamic efficiency, structural optimisation, and manufacturing innovation. A defining characteristic of the aircraft is its pusher configuration, with both the wing and engines located aft of the rear pressure bulkhead. This arrangement not only reduces cabin noise by isolating the primary noise sources from the passenger compartment, but also enables a more efficient structural layout and improved cabin usability.

From the viewpoint of the present thesis, these aspects are relevant because they define the structural architecture of the fuselage and therefore influence the dynamic response involved in cabin noise transmission.

A key design philosophy of the aircraft is the concentration of primary structural loads within a central “structural core”. Loads generated by the wing, landing gear, and aft pressurisation bulkhead are efficiently transferred through this core, allowing multiple load paths to be supported by the same structural elements at different times. This approach results in a significant reduction in structural weight while maintaining high strength and stiffness.

In the Avanti EVO configuration, the airframe is composed of approximately 90% aluminium alloys and 10% composite materials. The latter are strategically employed only in regions where their specific properties provide significant

Fig. 3.4 Integrally stiffened machined wing upper panel.

advantages, such as the horizontal stabiliser, fins and engine nacelles.
The wing structure consists of two halves joined at the fuselage centreline between structural bulkheads, the front one being the aft pressure bulkhead. The wing skins are machined from aluminium plates to incorporate integral stiffeners arranged in a grid pattern (Fig. 3.4). This solution eliminates the need for conventional stringers and riveted joints on the external surface, thereby improving aerodynamic smoothness and promoting laminar flow over a significant portion of the wing.

The main wing was developed around a dedicated low-drag laminar-flow airfoil, designed to exploit the favourable aerodynamic conditions provided by the pusher configuration. Since the propeller slipstream does not impinge on the main wing, the boundary layer can remain laminar over a larger portion of the chord than in conventional tractor-propeller aircraft [81]. Reported data indicate that laminar flow extends over approximately 45% of the upper surface and 55% of the lower surface, corresponding to more than 50% of the wing chord overall. This represents a significant improvement compared with typical values of about 20% for conventional tractor-propeller configurations [77].

Maintaining laminar flow was a primary design driver not only for the wing but also for the fuselage that features a continuously varying cross-section optimised to maximize internal volume while minimizing aerodynamic drag. The

Fig. 3.5 Avanti vacuum jigs for central fuselage assembly.

fuselage is designed as a monocoque structure made of conventional aluminium alloy, built through an innovative "outside-in" construction process, whereby large, stretch-formed and chemically milled skin panels are held in place by vacuum pressure as internal structure is riveted into place (Fig. 3.5). The result is a fuselage built to extremely close external tolerances, thus minimizing drag due to imperfections. This approach is essential to preserve the intended aerodynamic contours and to maintain laminar flow over the external surfaces [78, 81].

A stringer-less fuselage configuration was developed to minimize frame height, thereby maximizing the usable cabin width and improving passenger comfort. The aft placement of both the wing and the engines not only contributes to lower cabin noise levels but also enables full stand-up headroom within the cabin.

The combined action of the Avanti's three lifting surfaces, together with its laminar flow characteristics, allows for a 34% reduction in the main wing area compared to conventional designs, leading to proportional reductions in structural weight and profile drag.

3.3 Evolutionary Variants: From Avanti to the EVO

Since its introduction, the Piaggio P180 platform has undergone three major evolutionary stages, primarily driven by advancements in avionics, propulsion systems, and acoustic performance, leading to the identification of three main variants: the P180 Avanti, Avanti II, and Avanti EVO. Despite these developments, the fundamental architectural layout of the aircraft has remained essentially unchanged. In particular, the three-lifting-surface configuration and the rear-mounted pusher-propeller arrangement have been preserved across all variants.

The P180 platform is powered by two Pratt & Whitney Canada PT6A-66 series turboprop engines operating in a pusher configuration and driving five-blade Hartzell counter-rotating propellers. The engines are based on a free-turbine architecture, in which the gas generator and the power turbine driving the propeller are mechanically independent. This configuration provides high operational flexibility and is well suited to the high-speed turboprop mission of the aircraft.
The original P180 Avanti was equipped with PT6A-66 engines, while later variants, starting from the Avanti II, adopted the upgraded PT6A-66B standard. While maintaining the same flat-rated power, this evolution provided improved thermodynamic capability and enhanced high-altitude performance. In parallel, the propeller system has undergone significant evolution across the three configurations, with improvements in blade geometry and operating conditions.

From an acoustic standpoint, the P180 exhibits a distinctive behaviour. The rear-mounted propulsion system effectively isolates the cabin from the primary noise sources, resulting in consistently low internal noise levels and a high level of passenger comfort across all variants. However, the same pusher arrangement also introduces an important aeroacoustic limitation. Due to the pusher arrangement, the propellers operate within a highly disturbed inflow field, where the wakes generated by the forward wing, the main wing, and the engine exhaust impinge directly on the propeller disk. This interaction produces significant unsteady aerodynamic loading on the blades, leading to elevated external noise levels (Fig. 3.6) [78].

The following subsections summarise the main evolutionary stages of the P180 platform, focusing on the aspects most relevant to the present work: propulsion architecture, propeller operating conditions, acoustic performance and cabin-related design features.

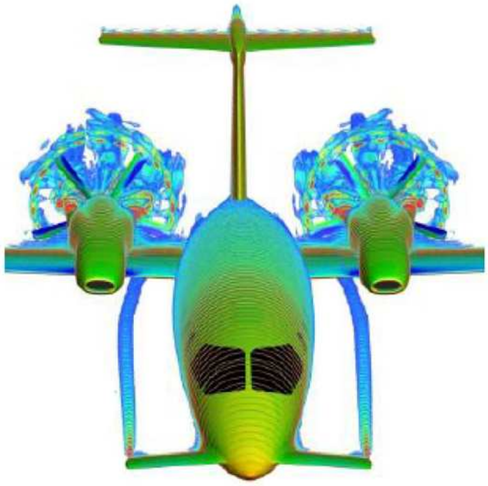

Fig. 3.6 Wake impingement on the rear-mounted pusher propeller disk.

3.3.1 The Original P180 Avanti (1986–2005)

The baseline configuration, certified in 1990 by both Italian authorities and the Federal Aviation Administration (FAA), established the aerodynamic and structural foundations of the platform (Fig. 3.7).

From a propulsion standpoint, the aircraft was equipped with two Pratt & Whitney Canada PT6A-66 turboprop engines, flat-rated at 850 SHP, driving five-blade Hartzell counter-rotating propellers in a pusher configuration. This architectural choice was driven not only by aerodynamic considerations but also by specific acoustic objectives defined early in the design phase. Indeed, since its inception in 1979, one of the primary goals was to ensure a high level of passenger comfort through low cabin noise and reduced vibration levels. The rear positioning of the engines and propellers, located aft of the pressurised cabin, effectively isolates the main noise sources from the passenger compartment. This configuration, combined with the extensive laminar flow over the fuselage and the absence of propeller-induced disturbances in the cabin region, results in a particularly quiet interior environment with minimal vibratory transmission. An additional benefit of the aft-mounted engine and wing configuration is the possibility of a flat cabin floor throughout the fuselage height, further improving passenger comfort. The pressurised cabin also offers generous dimensions — 1.85 m in width and 1.75 m in height — together with a differential pressure of 9.0 psi.

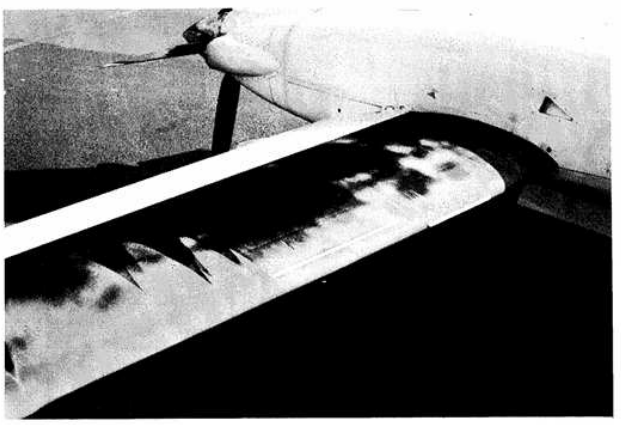

Fig. 3.7 Early certification flight-test campaign of the P180 Avanti (early 1990s). Natural Laminar Flow (NLF) visualisation on test aircraft FAN 571 (Flight 510) at 140 KIAS and 30.000 ft. The investigation utilised acenaphtene sublimating paint to map boundary-layer transition lines across the airframe, successfully verifying the real extension of NLF.

Despite its excellent internal acoustic performance, the original P180 already exhibited the characteristic aeroacoustic limitation associated with the pusher configuration. The propellers operate within the disturbed wake field generated by the upstream lifting surfaces and engine exhaust, leading to increased external noise levels.

The avionics suite was designed for single-pilot IFR operations under FAR 23 regulations, with a focus on reducing pilot workload and ensuring system reliability. Advanced for its era, the cockpit featured a hybrid analog/digital architecture with an Electronic Flight Instrument System (EFIS) for navigation and weather display. Automated flight was managed by the Collins APS-65A Digital Flight Control System, a fully integrated three-axis autopilot with electric trim capability. Redundant instrumentation and navigation systems were implemented to enhance operational safety.

From a structural standpoint, the airframe consists of approximately 80% aluminium alloy, while composite materials account for about 20% of the structure. The use of composites is concentrated in major sections including the tail, engine nacelles, and forward wing, all located outside the pressurised fuselage and not in contact with fuel for safety considerations.

In terms of performance, the aircraft achieved a cruise speed of approximately 711 km/h and a range of about 2.400 km, placing it among the fastest turboprop aircraft in its class.

3.3.2 P180 Avanti II (2005–2014)

The Avanti II represented a mid-life modernization of the P180 platform, primarily focused on improving cockpit integration, operational efficiency, and high-altitude performance, and passenger comfort.

From a propulsion standpoint, the aircraft was upgraded with the introduction of the Pratt & Whitney Canada PT6A-66B turboprop engines. While maintaining the same flat-rated power of 850 SHP, the thermodynamic rating was increased to approximately 1.630 HP, providing 8–13% more available power at high altitudes. This enhancement resulted in improved climb performance and more efficient cruise operation up to a service ceiling of FL410.

The most significant advancement was the integration of the Rockwell Collins Pro Line 21 avionics suite. This fully digital system replaced the previous hybrid architecture with an EFIS based on three large-format Adaptive Flight Displays, substantially improving situational awareness and reducing pilot workload.

From an acoustic perspective, the Avanti II maintained the key advantage of the original configuration, namely low internal noise levels ensured by the pusher-propeller arrangement. As reported in [77], at maximum cruise conditions (over 400 knots at 2.000 rpm), the propeller noise inside the cabin remains subdued but still noticeable. However, reducing the propeller speed below 1.900 rpm — at the cost of approximately 5 to 10 knots of cruise speed — results in a significant improvement in acoustic comfort, producing a cabin environment comparable to that of a modern light jet. Under optimised cruise conditions (350 KTAS at FL230 with propellers at 1.800 rpm), a Speech Interference Level of 65 dB is achieved, highlighting the aircraft's "best in class" internal noise performance.

Despite its excellent internal acoustic characteristics, the Avanti II retains the typical aeroacoustic limitation associated with the pusher configuration.

The aircraft was certified under FAR 36 and ICAO Annex 16 standards, with recorded values such as 76.0 EPNdB during flyover certification.

From a cabin perspective, the Avanti II introduced refinements in ergonomics and passenger comfort. The 2008 interior redesign included LED lighting systems and improved sidewall integration. In addition, an electrically powered vapor-cycle air conditioning system allows cabin pre-conditioning via Ground Power Unit prior to engine start.

In terms of performance, the Avanti II achieved a maximum cruise speed of approximately 740 km/h, confirming its position as one of the fastest turboprop aircraft in its category.

3.3.3 P180 Avanti EVO (2014–Present)

The Avanti EVO represents the most advanced evolution of the P180 platform, officially introduced in 2014, with first deliveries starting in 2015. This variant was developed to enhance aerodynamic efficiency, reduce environmental impact, and further improve operational performance and passenger comfort (Fig. 3.8).

A major advancement concerns the propulsion system, which was upgraded with Pratt & Whitney PT6A-66B engines now coupled with newly developed aluminium, counter-rotating five-blade scimitar-type Hartzell propellers. These propellers are specifically designed to operate at reduced rotational speeds, approximately 1.800 rpm, compared to 2.000 rpm in earlier variants. In addition, the propulsion system integration was refined through the introduction of patented “shark gills” exhaust ducts that optimize hot gases impact on blades and hub and at the same time improve thrust in cruise while reducing community noise at takeoff and landing [81] (Fig. 3.9).

A significant reduction in external noise is achieved, with an overall decrease of approximately 5 dB(A), corresponding to nearly a 68% reduction in perceived community noise.

In order to improve overall performance, the P180 Avanti EVO incorporates integrated winglets and new fiberglass forward wing tips, perfectly integrated in the original yet advanced aerodynamic design.

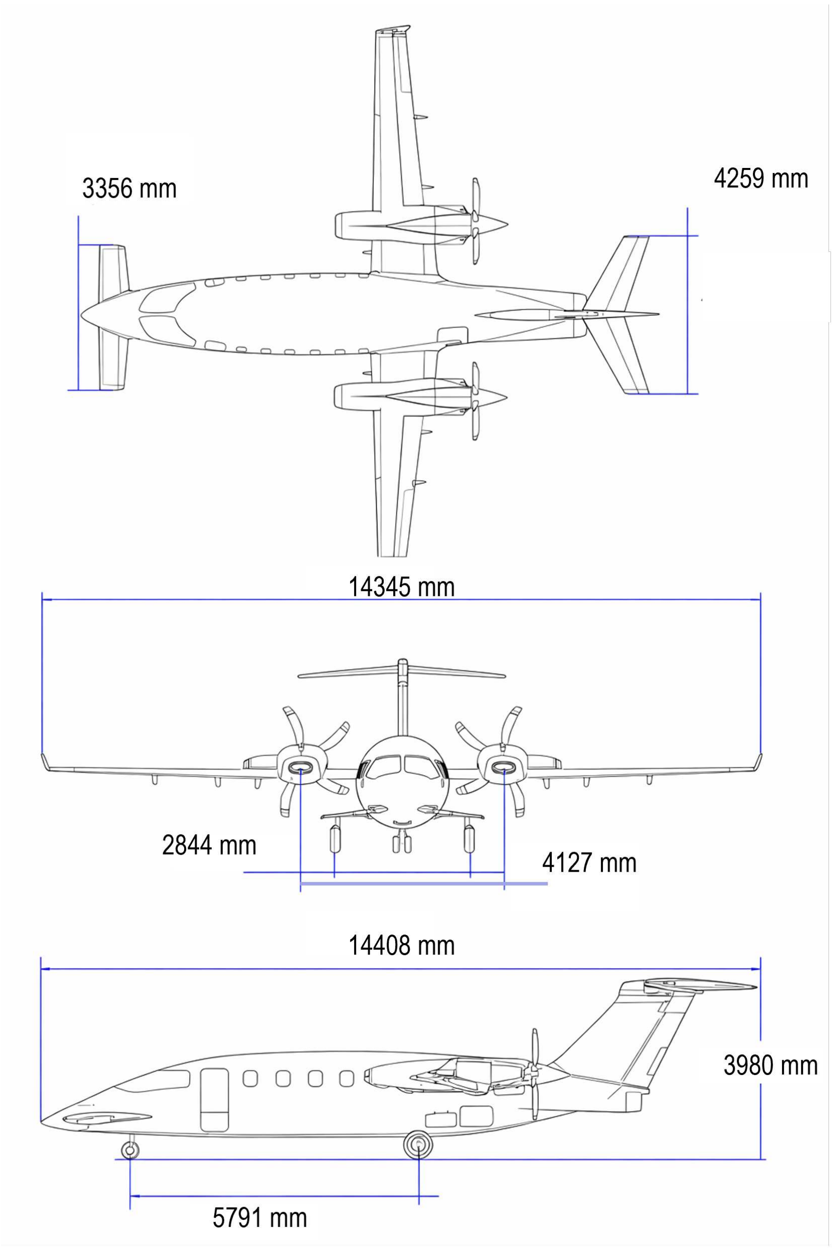

Fig. 3.8 Top, front, and side views of the Piaggio P180 Avanti EVO illustrating the main geometric dimensions of the aircraft configuration.

Fig. 3.9 Avanti EVO pusher propeller with scimitar blades and optimised low-noise “shark gill” exhaust ducts (left) and CFD visualisation of the disturbed wake field impinging on the propeller disk (right).

The current Avanti EVO features an airframe comprising 90% aluminium alloy and 10% composite construction. Advanced materials are retained for structurally efficient components like the horizontal stabiliser, engine nacelles - manufactured in carbon fiber to accommodate their complex area-ruled “wasp-waist” geometry - and the new winglets. In contrast, other sections such as the forward wing and fuselage nose have reverted to aluminium alloy construction, as the use of composite materials in these areas provided only marginal weight savings while significantly increasing manufacturing complexity and cost.

From a cabin perspective, these improvements contribute significantly to passenger comfort. Internal acoustic performance is enhanced, with cabin noise reduced by approximately 20%. In addition, the generous cabin dimensions — accommodating up to seven passengers — approximately 1.75 m in height, the highest in its class, and 1.85 m in width, exceeding that of many comparable aircraft — enable full stand-up headroom and provide an enhanced sense of space compared to conventional turboprop aircraft (see Fig. 3.10). Further comfort benefits are provided by the redesigned environmental control system, implemented as a fully digital dual-zone system with an increased cooling capacity of approximately 25%. The integration of a digital pressurisation controller allows optimised cabin pressure profiles during climb and descent. Combined with a pressurisation capability of approximately 9 psi, this ensures a sea-level cabin up to approximately 24.000 ft and maintains a cabin altitude of about 6.600 ft at a cruising altitude of 41.000 ft, thereby reducing passenger fatigue during high-altitude operations.

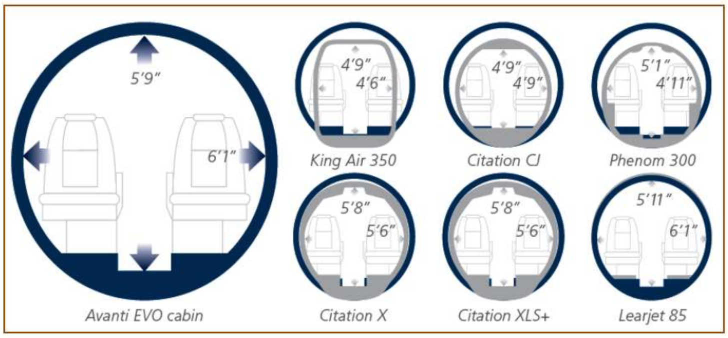

Fig. 3.10 Full stand-up cabin cross-section (left) and dimensional comparison with competing aircraft (right).

System-level upgrades include the introduction of a new Magnaghi landing gear with digital steering and optional anti-skid braking, improving ground handling and safety.

The avionics suite is based on an enhanced version of the Rockwell Collins Pro Line 21 Electronic Flight Instrument System system, a fully integrated digital flight deck that consolidates flight, navigation, and engine data into a set of large-format displays. This architecture significantly improves situational awareness and reduces pilot workload, supporting efficient single-pilot operations.

The Avanti EVO holds several world speed records, achieving a maximum cruise speed of approximately 745 km/h. For the present thesis, however, its main relevance lies in the combination of a high-speed pusher-propeller configuration, reduced propeller rotational speed, five-blade propellers and a pressurised fuselage architecture representative of the configuration used for the structural–acoustic finite element model.

3.4 P180 Avanti EVO Case Study for Low-Frequency Vibroacoustic Modelling

The Piaggio P180 Avanti EVO represents a particularly relevant case study for the development of a cabin-noise prediction framework because it combines an unconventional aircraft configuration with distinctive vibroacoustic excitation mechanisms. The aircraft is one of the fastest and most efficient turboprop aircraft in its class and remains, to date, the only certified aircraft featuring a three-lifting-surface configuration. Its sustained use as a multipurpose platform across civil and institutional applications, including medical services, law enforcement and surveillance, aerial photography and surveying, flight inspection, executive and business transport, regional transport, cargo missions and pilot training, further supports its relevance as an industrially meaningful configuration.

From a technical point of view, the interest in the P180 Avanti EVO is mainly related to its rear-mounted pusher-propeller arrangement. The pusher arrangement contributes to the aerodynamic efficiency of the platform by preserving natural laminar flow over a large portion of the wing and fuselage surfaces, while enabling a reduction of approximately 34% in the total wing area. However, this same configuration places the propellers within the disturbed inflow generated by the forward wing, main wing, fuselage, and the engine exhaust. As a consequence, the propeller blades are subjected to significant unsteady aerodynamic loading, giving rise to a characteristic tonal acoustic signature and making the exterior noise signature one of the most critical aeroacoustic aspects of the P180 platform.

A further motivation for selecting the P180 Avanti EVO lies in the availability of experimental data at different validation levels. In particular, structural modal data and laboratory acoustic measurements are available for configurations representative of the aircraft fuselage. This allows the related numerical model to be assessed both in terms of structural dynamics and coupled vibroacoustic response.

3.4.1 Definition of the BPF Harmonic Range

From an aeroacoustic standpoint, the dominant tonal components generated by a propeller occur at the BPF and its harmonics. As reported in [82], in pusher-propeller configurations, the unsteady blade loading caused by the interaction between the rotating blades and the wake mean velocity distribution of upstream bodies (forward wing, main wing, fuselage, and engine exhausts) amplifies the tonal content of the acoustic spectrum. This interaction is particularly critical in the low- and mid-frequency range most relevant for cabin noise transmission. While the fundamental BPF component generally carries the highest acoustic energy and is primarily governed by thickness and steady-loading noise mechanisms, the interaction with the mean velocity deficit of the wake can substantially increase the levels of the harmonics above the first by 10 to 20 dB. As a result, the first few BPF orders define the frequency range of primary interest for the development of the vibroacoustic model.

For the development of a high-fidelity cabin noise prediction framework, considering a frequency range covering the first three BPF harmonics is therefore physically justified.

For the reference operating condition considered in this thesis, the five-blade propellers of the P180 Avanti EVO operate at approximately 1800 rpm. The corresponding fundamental BPF is therefore about 150 Hz, while the second and third harmonics occur at approximately 300 Hz and 450 Hz, respectively. The frequency range up to the third BPF harmonic is therefore adopted as the primary band of interest for the vibroacoustic analyses developed in the following chapters.

3.4.2 Implications for Structural–Acoustic Model

The aircraft features discussed in this chapter have direct implications for the modelling strategy adopted in the present thesis. The rear-mounted pusher-propeller configuration defines the frequency range of primary interest through the BPF and its first harmonics, while the lightweight pressurised fuselage governs the main structural transmission path between the external excitation and the internal cabin environment.

From a structural point of view, the passenger floor, frames, stringers, bulkheads, window frames, door region and emergency-exit area represent key features affecting the dynamic response of the cockpit–cabin assembly. These components introduce local stiffness variations and geometrical discontinuities that may influence the transmission of external pressure fluctuations into the cabin acoustic cavity.

From an acoustic point of view, the non-cylindrical cabin geometry, the presence of the floor and the local cavities surrounding the windows are expected to affect the spatial distribution of the internal pressure field, especially in the low-frequency range where acoustic modes are sparse and well separated.

On this basis, the structural–acoustic FE model developed in Chapter 4 is required to represent not only the global fuselage barrel, but also the main structural and acoustic features that govern low-frequency cabin-noise transmission.

Chapter 4

Structural–Acoustic Finite Element Model of the Piaggio P180 Avanti EVO Fuselage

4.1 Introduction and Modelling Objectives

This chapter describes the development of the structural–acoustic FE model of the Piaggio P180 Avanti EVO cockpit–cabin fuselage assembly. The model is intended for subsequent coupled vibroacoustic analyses in the low- to mid-frequency range, with the objective of predicting the acoustic response inside the passenger cabin within the frequency range covering the first three BPF harmonics.

The model is developed from the three-dimensional (3D) CAD geometry provided by Piaggio Aerospace and reduced to the fuselage region relevant to the cockpit and passenger cabin vibroacoustic response. The FE model is based on a hybrid structural discretisation strategy. Thin-walled structural components are represented by shell elements, while local stiffening contributions are introduced by means of one-dimensional structural elements where appropriate. The internal acoustic domain is modelled using 3D acoustic fluid elements.

The frequency range of interest is governed by the tonal excitation produced by the five-blade propellers. For the operating condition considered in this work, the propeller rotational speed is equal to 1800 rpm. The corresponding fundamental BPF is therefore

$$f_{\mathrm{BPF}} = N_b \frac{\Omega}{60} = 5\frac{1800}{60} = 150 \text{ Hz}, \tag{4.1}$$

where N_b is the number of blades and Ω is the propeller rotational speed expressed in revolutions per minute. Since the first three BPF harmonics are considered, the maximum excitation frequency of direct interest is

$$f_{\mathrm{exc,max}} = 3f_{\mathrm{BPF}} = 450 \text{ Hz}. \tag{4.2}$$

Although the coupled vibroacoustic response is investigated up to the third BPF harmonic, the structural model must retain sufficient modal accuracy over a wider frequency range. In modal-based vibroacoustic analyses, a frequency margin above the maximum excitation frequency is commonly introduced in order to account for the influence of neighbouring higher-frequency modes. Therefore, in the present work, the target frequency adopted for the structural mesh definition is set equal to twice the maximum excitation frequency, namely

$$f_{\mathrm{conv}} = 2f_{\mathrm{exc,max}} = 900 \text{ Hz}. \tag{4.3}$$

The structural and acoustic meshes are defined according to their respective physical resolution requirements. The structural mesh is sized to capture the relevant modal deformation patterns and bending wavelengths of the fuselage components up to the target convergence frequency. Therefore, dedicated mesh convergence studies are performed for the main structural regions. The acoustic mesh is instead defined according to the acoustic wavelength in air, while preserving compatibility with the structural discretisation along the fluid–structure interfaces.

The chapter is organised as follows. First, the geometrical model and the main structural layout of the fuselage are described. The structural FE model is then introduced, with particular attention to the mesh-sizing methodology adopted for the skin, frames, stringers, floor and local reinforcements. The structural model, including both the passenger cabin and cockpit regions, is

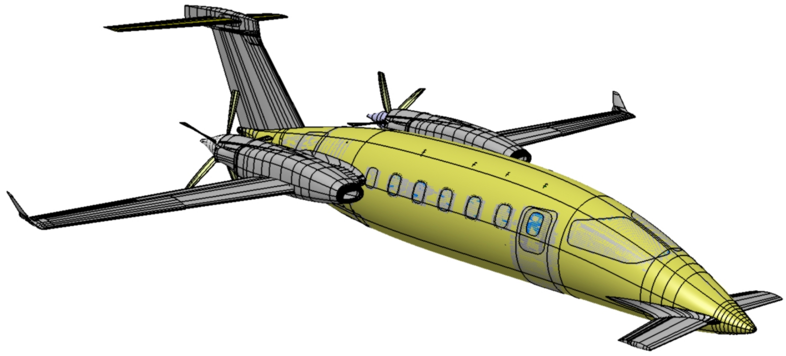

Fig. 4.1 Three-dimensional CAD model of the Piaggio P180 Avanti EVO.

then assessed through modal correlation with available experimental free–free data. The acoustic FE model is subsequently discussed, including the definition of the cabin acoustic cavity, the acoustic mesh-sizing criterion and the modal verification of the fluid domain.

4.2 Geometrical Definition of the Fuselage Model

The starting point of the modelling activity is the complete 3D CAD model of the Piaggio P180 Avanti EVO, provided by Piaggio Aerospace. Since the objective of the present work is the prediction of the acoustic response inside the cabin, the aircraft-level CAD model was reduced to the fuselage region directly involved in the vibroacoustic transmission path. The resulting geometrical model includes the fuselage barrel portion containing both the cockpit and the passenger cabin, as shown in Fig. 4.2. The retained fuselage structure consists of the external skin, circumferential frames, longitudinal stringers, bulkheads, window frames, passenger floor and floor stiffening members. These components are selected because they either define the boundaries of the internal acoustic cavity or contribute to the structural dynamic behaviour governing the transmission of external pressure fluctuations towards the cabin interior.

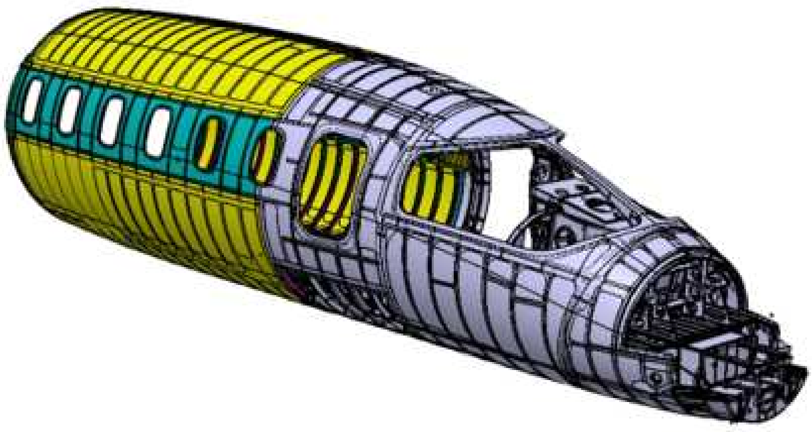

(a) External view of the cockpit–cabin fuselage CAD model.

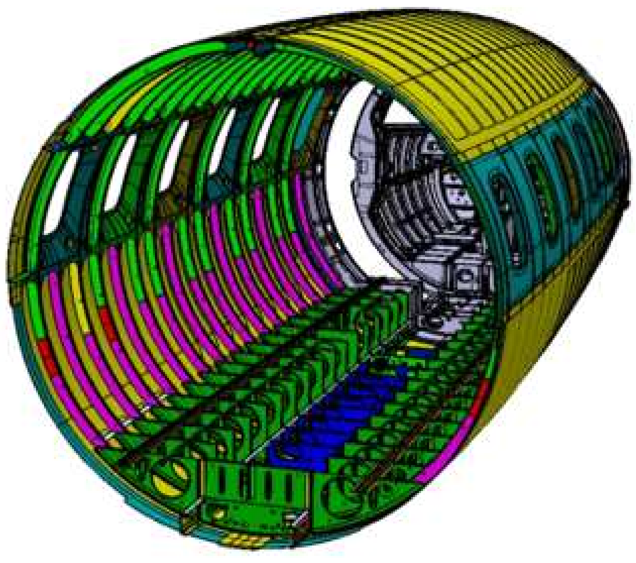

(b) Internal view showing the structural layout of the passenger cabin region.

Fig. 4.2 Three-dimensional CAD model of the Piaggio P180 cockpit–cabin fuselage assembly: external configuration and internal structural arrangement.

4.3 Structural Finite Element Model

The structural FE model is based on a reduced-dimensional representation of the fuselage structure. Due to the thin-walled nature of the aircraft fuselage, a full 3D solid FE model would lead to a prohibitive computational cost, especially for frequency-domain coupled structural–acoustic simulations. Therefore, the main thin-walled structural components are represented by shell elements, while one-dimensional elements are locally introduced where required to reproduce additional stiffening effects and equivalent sectional properties. This hybrid FE approach provides an efficient representation of the structural dynamics of the fuselage while preserving the main stiffness and mass characteristics of the actual aircraft structure [83].

A reference FE model provided by Piaggio Aerospace is used as the structural baseline for the definition of material properties, shell thicknesses, one-dimensional element types and equivalent sectional properties of the stiffening members. However, the spatial resolution of the Piaggio mesh is not suitable for the vibroacoustic frequency range considered in this work, since it was developed for modelling requirements different from those of the present analysis and does not provide the local resolution required to capture the relevant deformation patterns of the thin-walled components. For this reason, a new geometry-based structural model is generated from the CAD data through a dedicated mid-surface extraction procedure. In this process, the CAD model provides the geometrical reference for the reconstructed shell surfaces, while the Piaggio FE model provides the structural idealisation and property data adopted in the present work.

4.3.1 Mid-Surface Extraction and Modelling Assumptions

The reduced-dimensional structural geometry is generated from the 3D CAD model through a dedicated mid-surface extraction procedure performed in Siemens FEMAP [84]. This operation provides the geometrical basis required for the shell discretisation of the thin-walled fuselage components. In the mid-surface representation, each thin-walled solid component is replaced by its

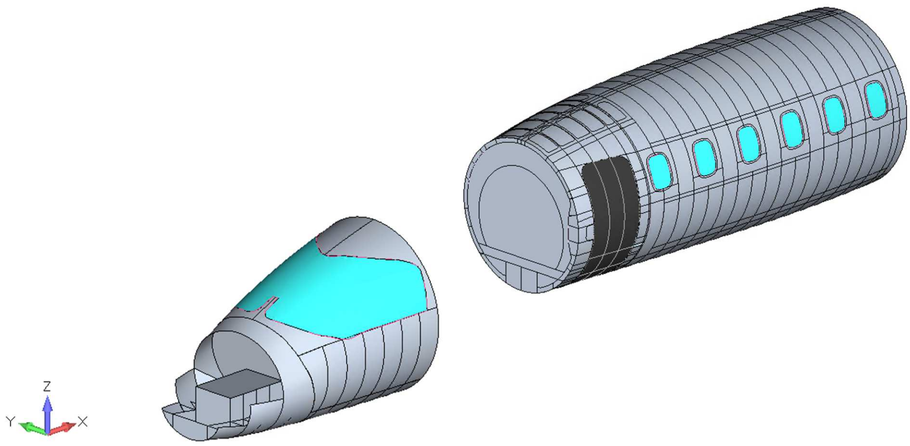

Fig. 4.3 Two-dimensional geometrical representation of the fuselage region including cockpit and passenger cabin.

geometrical middle surface. The approach is appropriate for the present fuselage structure, since the characteristic thicknesses of the skin, frames, stringers, bulkheads, window frames and floor components are much smaller than their in-plane dimensions.

The resulting two-dimensional geometrical model of the cockpit–cabin fuselage region is shown in Fig. 4.3. The model includes the cockpit section, with a length of approximately 2.3 m, and the passenger cabin, characterised by a maximum diameter of approximately 1.87 m and a length of approximately 4.7 m.

Figure 4.4 shows the internal structural components of the passenger cabin with the external skin removed for clarity. The two bulkheads delimiting the passenger cabin are visible in Fig. 4.4a, while Fig. 4.4b provides a detailed view of the internal cabin structure, including frames, stringers, window frames, floor components and local reinforcements associated with the passenger door and emergency exit window.

For the cockpit region, Fig. 4.5 shows the two-dimensional mid-surface geometry used for the subsequent shell discretisation. Consistently with the structural idealisation adopted in the reference Piaggio FE model, the circumferential stiffening members in this region are represented by one-dimensional elements rather than by shell components. Therefore, they are not included in the

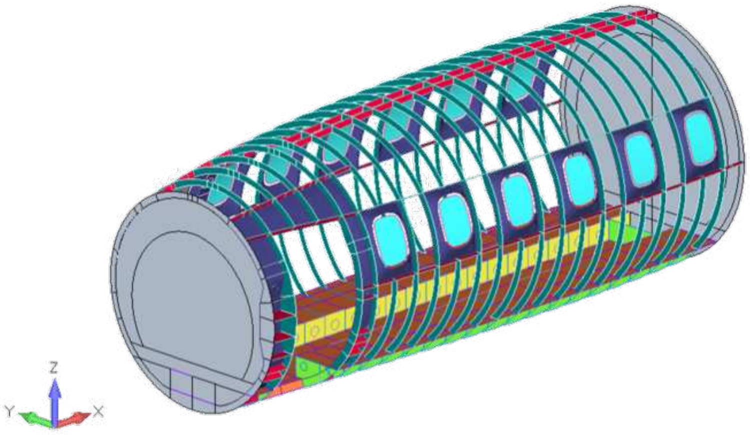

(a) Detail view of the two bulkheads delimiting the passenger cabin.

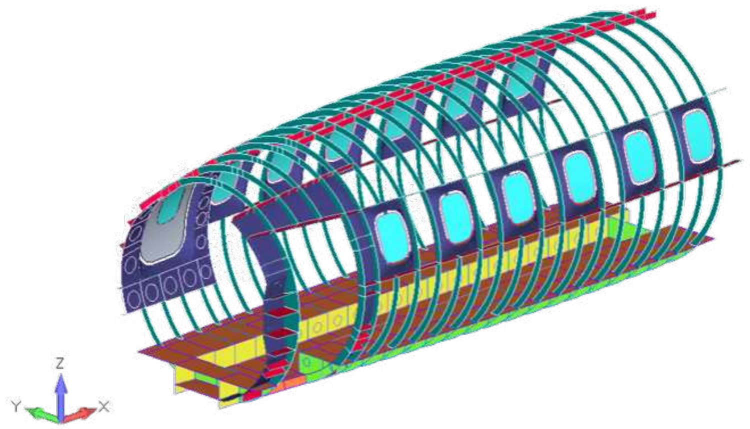

(b) Internal structural components of the passenger cabin.

Fig. 4.4 Two-dimensional structural representation of the passenger cabin, with the external skin removed for clarity.

mid-surface geometry, which displays only the components to be discretised with shell elements.

Within this idealisation, the fuselage skin is discretised using shell elements. This component constitutes the primary structural interface between the external pressure field and the internal acoustic cavity and is therefore central to the subsequent vibroacoustic analysis. The local skin regions bounded by frames and longitudinal stiffeners define the bay topology used later for the component-level mesh convergence studies.

The stringers and frames are modelled through a combination of shell and one-dimensional elements. Their main thin-walled portions are described by shell elements, while additional sectional stiffness contributions are introduced through one-dimensional elements where required. This approach preserves the equivalent stiffness representation of the reference Piaggio FE model while allowing the shell mesh to be refined according to the dynamic resolution requirements of the present work.

The passenger floor is modelled as a continuous structural component along the fuselage longitudinal direction and is connected to the surrounding fuselage barrel. It contributes to the stiffness distribution of the lower fuselage region and defines the lower boundary of the main cabin acoustic domain. The bulkheads provide the longitudinal structural and acoustic boundaries of the cockpit–cabin assembly. Window frames, the passenger door region, the emergency exit window and the associated reinforcements introduce local stiffness variations and geometrical discontinuities, which are relevant to both the structural response and the acoustic cavity shape.

A specific modelling assumption concerns the structural components located below the passenger floor, visible in the lower region of Fig. 4.2b as the green and blue under-floor members. The CAD geometry of these under-floor components includes perforated members with flanged openings. In the reference FE model provided by Piaggio Aerospace, these components are represented as non-perforated shell parts with equivalent properties. This idealisation is assumed to provide a statically equivalent representation of the actual perforated members at the level of the global structural model. The same representation is therefore adopted in the present work. The corresponding material data, thicknesses and equivalent shell properties are taken from the Piaggio model and assigned to the

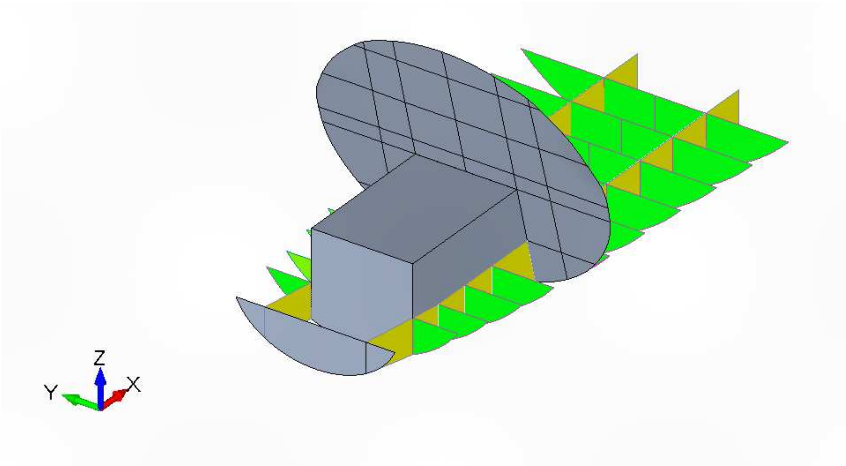

(a) First view of the shell-based structural components of the cockpit region.

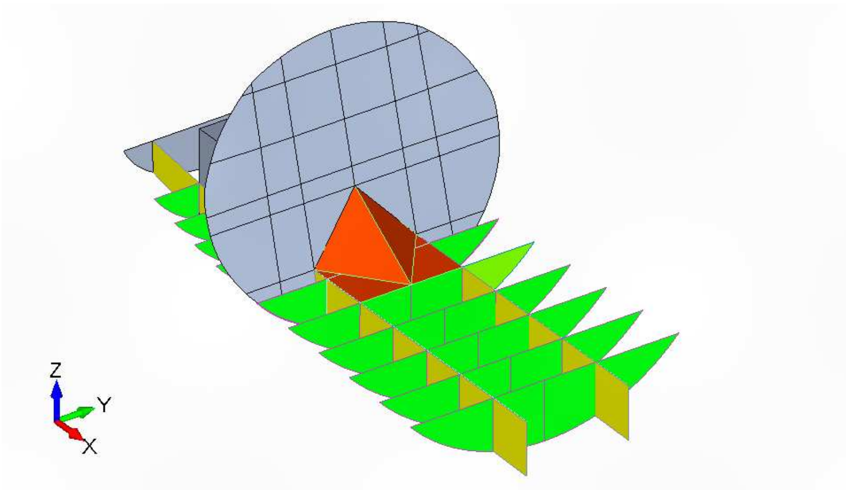

(b) Second view of the shell-based structural components of the cockpit region.

Fig. 4.5 Two-dimensional shell representation of the cockpit region from two different viewpoints, with the external skin removed for clarity. Circumferential stiffeners represented by one-dimensional elements are not displayed in these mid-surface views.

continuous shell representation. This assumption is consistent with the level of detail adopted for the coupled structural–acoustic model. The acoustic domain is limited to the passenger cabin volume above the floor, whereas the under-floor cavities are not explicitly represented. As a consequence, retaining the perforations in the under-floor structural members would introduce additional geometrical detail in the structural model without a corresponding acoustic counterpart. The non-perforated representation is therefore adopted as the most coherent idealisation with respect to both the reference structural model and the acoustic domain considered in this work.

4.3.2 Structural Mesh-Sizing Methodology

The structural mesh is defined not only to reproduce the geometrical features of the fuselage, but also to provide an adequate spatial resolution of the structural deformation patterns involved in the subsequent vibroacoustic analyses. The discretisation is therefore selected to capture both global fuselage deformation mechanisms and local bending-dominated patterns within the target frequency range.

The mesh-sizing procedure is performed at component level for the main structural regions of the fuselage, namely skin panels, stringers, frames, floor and under-floor stiffening members. This approach is adopted because these components differ in geometry, thickness, boundary conditions and stiffness distribution, and therefore exhibit different local modal behaviour.

Two main assumptions underlie the local convergence studies. First, the convergence analyses are aimed at defining the spatial resolution required by the shell discretisation. For this reason, they are generally performed on the shell-like portions of the components, without explicitly including the corresponding one-dimensional stiffening elements. The latter are subsequently introduced in the complete fuselage model according to the equivalent sectional properties derived from the Piaggio reference FE model. From a mesh-sizing point of view, this represents a conservative assumption for the shell discretisation, since the less stiff plate-like component may exhibit lower natural frequencies and more pronounced local deformation patterns within the investigated frequency range. If the selected shell mesh is able to resolve these deformation patterns, the same discretisation is expected to remain adequate once the component is stiffened by the corresponding one-dimensional elements in the complete fuselage model. Second, the local models are not analysed as isolated free components. Boundary conditions are assigned in order to reproduce, in an idealised manner, the support provided by the surrounding fuselage structure. When the actual restraint conditions are uncertain or varied along the fuselage, the less constrained configuration is selected. This provides a conservative basis for mesh sizing, since a less restrained component tends to exhibit lower natural frequencies and more pronounced deformation patterns within the frequency range of interest.

The mesh definition is based on two complementary criteria. Analytical wavelength estimates are used only for components whose geometry and boundary conditions allow a simplified plate-like idealisation. For curved or geometrically complex components, the element size is instead determined through numerical modal convergence analyses on representative models.

Frequency Range and General Resolution Criterion

As introduced in Section 4.1, the coupled vibroacoustic response is investigated up to the third BPF harmonic, corresponding to $f_{\text{exc,max}} = 450$ Hz. However, the structural mesh is sized with respect to the higher target convergence frequency $f_{\text{conv}} = 900$ Hz, equal to twice the maximum excitation frequency. This frequency margin allows the neighbouring higher-frequency modal content to be represented, since modes located above the excitation band may still affect the response through their residual flexibility. The element size is therefore selected to capture the relevant structural modal content up to f_{conv}, both in terms of natural frequencies and associated mode shapes.

The limiting requirement is associated with the shortest relevant bending wavelength or, equivalently, with the highest local modal order that has to be represented within the target frequency range. In general terms, the element size must satisfy

$$h_e \leq \frac{\lambda_{\min}}{N}, \tag{4.4}$$

where h_e is the characteristic element size, $\lambda_{\min}$ is the shortest structural wavelength to be resolved, and N is the number of elements per wavelength. In this work, the preliminary wavelength-based criterion is applied by requiring at least six linear elements per bending wavelength.

The analytical estimates of the bending wavelengths are obtained using the plate formulation reported in Appendix A. This formulation provides the approximate natural frequencies and the corresponding characteristic wavelengths along the principal in-plane directions for a rectangular plate-like component with assigned boundary conditions.

The application of this criterion depends on the geometry of the component under consideration. For components with sufficiently regular and planar geometry, analytical estimates of the relevant modal orders and bending wavelengths can be used to obtain a preliminary mesh size. This approach is adopted for the stringer segment, which is geometrically regular over the span between two adjacent frames and can therefore be idealised, as a first approximation, as a flat plate-like component.

For components with non-planar or geometrically non-regular configurations, such as the curved fuselage skin bays, frames and under-floor structural members, the analytical wavelength criterion cannot be applied in a straightforward manner. Since these components cannot be reduced to regular flat plate-like domains, the mesh size is defined through numerical modal convergence studies. Progressively refined discretisations are compared up to the target convergence frequency in terms of natural frequencies and corresponding mode shapes. The refined reference solution is selected as the finest discretisation for which the modal response is sufficiently stabilised, with unchanged dominant mode shapes and negligible frequency variations with respect to the previous refinement level.

The percentage frequency error of each candidate mesh is evaluated with respect to this refined reference solution as

$$\Delta f_{\mathrm{i}}^{(h)} = \frac{\left| f_{\mathrm{i}}^{(h)} - f_{\mathrm{i}}^{(ref)} \right|}{f_{\mathrm{i}}^{(ref)}} \times 100, \tag{4.5}$$

where $f_{\mathrm{i}}^{(h)}$ is the natural frequency of the i-th tracked modal family obtained with the mesh size h, and $f_{\mathrm{i}}^{(ref)}$ is the corresponding frequency obtained with the refined reference mesh.

The selected mesh is retained when the relevant modal families up to f_{conv} exhibit frequency errors lower than 1% and preserve the same dominant mode shapes.

Stringer Mesh Definition

The mesh definition of the longitudinal stringers is first addressed through an analytical wavelength-based criterion, since the stringer segment between two adjacent frames can be idealised, as a first approximation, as a regular flat plate-like component.

The local restraint conditions of the stringers vary along the fuselage because of the presence of window reinforcements and other local structural details. For the mesh-sizing study, a single conservative boundary-condition configuration is adopted. The two short edges, corresponding to the intersections with adjacent frames, and the long edge connected to the fuselage skin are modelled as simply supported, while the opposite long edge is left free. This assumption represents a less constrained configuration than the locally reinforced cases and is therefore conservative for the shell mesh definition.

The analytical estimate is performed through a MATLAB routine implementing the closed-form formulation reported in Appendix A. The routine assigns the selected boundary conditions along the two principal directions and computes the approximate natural frequencies f_{ij}, together with the corresponding bending wavelengths λ_x and λ_y. The results obtained for the representative stringer segment are reported in Table 4.1. The modes located in the neighbourhood of $f_{\mathrm{conv}} = 900$ Hz identify the limiting modal orders, namely $i_{\max} = 5$ and $j_{\max} = 2$, and the corresponding minimum bending wavelengths. Assuming six linear elements per wavelength, the resulting preliminary element sizes are $h_{\mathrm{x}} = 0.0137m$ and $h_{\mathrm{y}} = 0.0074m$.

Table 4.1 Analytical estimate of natural frequencies, bending wavelengths and preliminary element sizes for the representative stringer segment.

i	j	f_{ij} [Hz]	λ_x [m]	λ_y [m]	$h_x = \lambda_x/6$ [m]	$h_y = \lambda_y/6$ [m]
1	1	97.72	0.4120	0.0800	0.0687	0.0133
2	1	229.51	0.2060	0.0800	0.0343	0.0133
3	1	415.70	0.1373	0.0800	0.0229	0.0133
4	1	665.09	0.1030	0.0800	0.0172	0.0133
1	2	970.20	0.4120	0.0444	0.0687	0.0074
5	1	981.13	0.0824	0.0800	0.0137	0.0133
2	2	1110.64	0.2060	0.0444	0.0343	0.0074
3	2	1329.98	0.1373	0.0444	0.0229	0.0074

It should be noted that this analytical procedure provides only a preliminary estimate of the required mesh resolution. The formulation approximates the plate deformation by means of two independent beam-like modal shapes along the principal directions, thus providing two separate characteristic wavelengths, λ_x and λ_y. The final element size is therefore selected through the numerical convergence study reported below.

Five square shell meshes are considered in the numerical convergence study, with characteristic element sizes equal to 28, 14, 7, 3.5, and 1.75 mm. The finest mesh, $h_{\text{ref}} = 1.75$ mm, is adopted as the reference solution. For each mesh, the same modal deformation patterns are identified and compared. The corresponding natural frequencies and percentage errors are reported in Tables 4.2 and 4.3, respectively.

Table 4.2 Natural frequencies obtained for the representative stringer segment using different square element sizes.

Mode	$h = 1.75$ mm	$h = 3.5$ mm	$h = 7$ mm	$h = 14$ mm	$h = 28$ mm
Mode 1	97.15	97.04	96.54	95.29	90.56
Mode 2	227.46	227.14	225.78	222.40	209.50
Mode 3	411.12	410.43	407.75	401.30	377.79
Mode 4	657.09	655.87	651.45	641.57	611.47
Mode 5	967.67	962.25	941.83	891.42	741.70

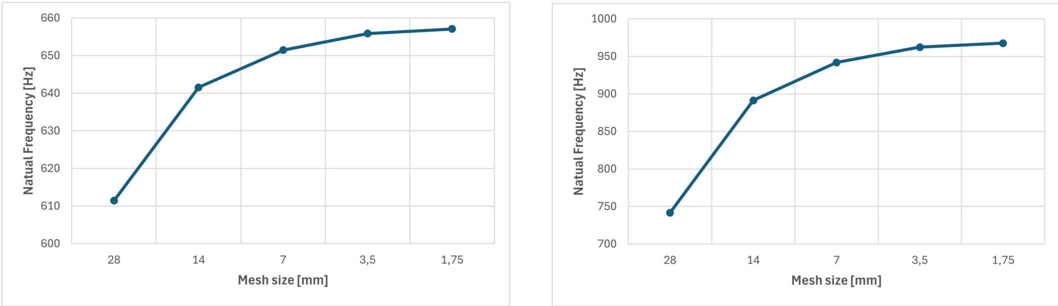

(a) Mode 4 (b) Mode 5

Fig. 4.6 Convergence trends of the stringer natural frequencies located in the neighbourhood of $f_{\mathrm{conv}} = 900$ Hz as a function of the square element size: (a) Mode 4; (b) Mode 5.

Table 4.3 Percentage errors of the natural frequencies with respect to the refined reference mesh $h_{\mathrm{ref}} = 1.75$ mm.

Mode	$h = 3.5$ mm	$h = 7$ mm	$h = 14$ mm	$h = 28$ mm
Mode 1	0.11	0.63	1.91	6.78
Mode 2	0.14	0.74	2.22	7.90
Mode 3	0.17	0.82	2.39	8.11
Mode 4	0.19	0.86	2.36	6.94
Mode 5	0.56	2.67	7.88	23.35

The convergence trends of the two modal families closest to f_{conv} are shown in Fig. 4.6. Their proximity to the target convergence frequency makes them suitable indicators for assessing the adequacy of the selected stringer mesh size.

The results show that the square mesh with $h = 7$ mm provides frequency errors lower than 1% for all the modal families below f_{conv}. The additional mode located immediately above the target frequency is retained as a supplementary check of the convergence trend in the neighbourhood of 900 Hz; although its frequency error is slightly larger, the corresponding deformation pattern remains unchanged. Therefore, considering the convergence of all modes within the target frequency range and the computational cost of the complete fuselage model, a square shell element size $h_{\mathrm{stringer}} = 7mm$ is retained for the stringer shell portions.

The hybrid shell/one-dimensional stringer representation is also checked numerically. Since the one-dimensional stiffening contribution increases the natural frequencies associated with the same dominant mode shapes, the plate-only convergence study is retained as a conservative basis for the shell mesh definition.

Skin Mesh Definition

A dedicated mesh-sizing procedure is adopted for the fuselage skin, since it is a curved shell component rather than a flat plate. The relevance of curvature effects is first assessed through the ring frequency associated with the local cylindrical curvature of the fuselage skin,

$$f_{\text{ring}} = \frac{1}{2\pi R}\sqrt{\frac{E}{\rho\,(1-\nu^2)}}, \tag{4.6}$$

where R is the local shell radius, E is Young's modulus, ρ is the material density and ν is Poisson's ratio. For the fuselage geometry considered in this work, the estimated ring frequency is of the order of, and slightly higher than, the target convergence frequency $f_{\text{conv}} = 900$ Hz. This indicates that curvature-induced membrane–bending coupling may still affect the skin modal behaviour within the frequency range considered. For this reason, analytical formulations based on an equivalent flattened panel are not used for the skin mesh definition. Instead, the element size is selected through numerical modal convergence analyses performed directly on representative curved skin panels.

The representative region selected for the skin mesh-sizing procedure is the fuselage barrel located in correspondence with the maximum fuselage diameter. In this context, the barrel denotes the portion of fuselage skin bounded by two adjacent frames and extending over the full circumference. This choice is conservative for the numerical convergence study, since the larger diameter leads to larger circumferential bay dimensions and therefore to lower local natural frequencies.

The barrel is further subdivided into several skin bays by the longitudinal stiffeners, which split the full circumferential skin region into separate curved panels. Since the resulting bays differ in circumferential size and, in some cases, in local skin thickness, separate numerical convergence analyses are carried out for the relevant bay configurations around the cross-section. In the local convergence models, the bay edges are modelled as simply supported in order to represent, in an idealised and conservative manner, the restraint provided by the surrounding frames and longitudinal stiffeners.

For each representative skin bay, a local modal convergence study is performed by progressively refining the mesh in the circumferential direction. The element size in the longitudinal direction is kept fixed and equal to 7 mm, consistently with the mesh requirement previously defined for the stringer shell portions. The analyses performed on the different bay configurations showed that a circumferential element size equal to 10 mm ensures a maximum frequency error lower than 1% with respect to the refined reference mesh for the relevant modes up to $f_{\text{conv}} = 900$ Hz. The corresponding mode shapes also remained unchanged in terms of dominant deformation pattern.

Frame Mesh Definition

Since the frames are connected to the skin and intersect the longitudinal stringers, their mesh definition must be compatible with the discretisation already selected for the adjacent components. The resulting frame discretisation is therefore defined by

$$h_\theta = 10 \text{ mm}, \qquad h_x = 7 \text{ mm}. \tag{4.7}$$

This mesh choice is verified through local numerical convergence analyses performed on representative frame segments. The analysed segment is bounded by two adjacent stringer intersections. The skin-side edge and the two transverse edges at the stringer intersections are modelled as simply supported, while the opposite long edge is left free. The free-edge condition represents the less constrained configuration, since some frame portions may receive additional support from local reinforcements, particularly in the window region. It is therefore adopted as a conservative assumption for the convergence assessment.

Floor and Under-Floor Structural Components

The modelling assumptions for the floor and under-floor structural components have been discussed in Section 4.3.1. As previously introduced, the under-floor members are represented as non-perforated shell components, consistently with the reference FE model provided by Piaggio Aerospace and with the level of detail adopted for the acoustic domain.

The mesh characterisation of these components requires additional considerations, since they are panels oriented in both axial and circumferential planes. Therefore, the discretisation cannot be defined only in terms of the global axial and circumferential directions, but must also account for the local in-plane directions of the corresponding panels. Keeping the previously defined axial and circumferential element sizes unchanged, dedicated numerical convergence analyses are performed to define the element size along these additional local directions, while accounting for geometrical transitions, intersections between adjacent members and local thickness variations.

4.3.3 Structural Element Types and Property Definitions

The structural discretisation adopted in this work is based on a hybrid FE mesh composed of shell elements and one-dimensional structural elements. The mesh convergence studies discussed in the previous sections refer to the shell discretisation of the thin-walled fuselage components, which are modelled using linear NASTRAN shell elements, namely `CQUAD4` four-node quadrilateral elements and `CTRIA3` three-node triangular elements. These elements use a 6 degree-of-freedom per node formulation.

The local stiffness enrichment is introduced through one-dimensional structural elements. The adopted element types are:

- `CROD`: two-node rod element, used to represent members with axial and torsional stiffness;

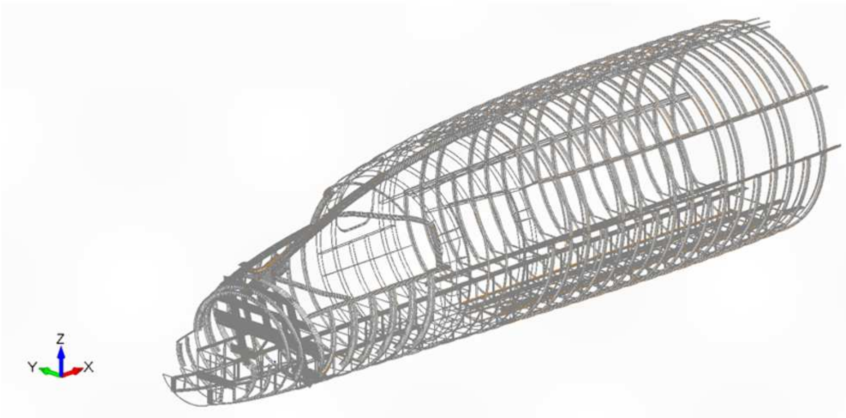

Fig. 4.7 Representation of the one-dimensional structural elements adopted in the finite element model.

- `CBAR`: two-node beam-type element with six degrees of freedom per node, used for stiffening members with assigned sectional properties and orientation;
- `CBEAM`: two-node beam element with six degrees of freedom per node, used where the definition of sectional properties, orientation and offsets requires a more detailed beam representation.

The properties of the one-dimensional elements are assigned according to the corresponding rod, bar and beam definitions available in the Piaggio Aerospace reference model. In this way, the refined mesh developed in the present work preserves the structural idealisation and equivalent sectional properties of the reference model, while providing the spatial resolution required for the vibroacoustic analyses.

The final structural discretisation consists of approximately 1.6×10^6 shell elements, locally enriched with one-dimensional structural members. The complete structural mesh includes about 1.6×10^6 nodes, corresponding to approximately 9.6×10^6 structural degrees of freedom. A graphical representation of the one-dimensional structural members included in the model is shown in Fig. 4.7.

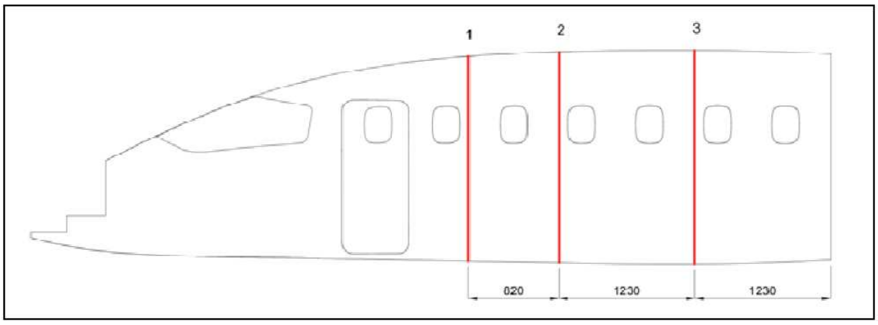

Fig. 4.8 Instrumented fuselage frames positions.

4.3.4 Structural Natural Frequencies and Model Validation

The dynamic behaviour of the numerical structural model is assessed through modal correlation with available free–free experimental natural frequencies and mode shapes.

The reference experimental data are obtained from a modal test campaign conducted jointly by the Department of Aerospace Engineering at the University of Naples Federico II and Piaggio Aerospace, as presented by Polito et al. [85]. In order to reproduce free-free boundary conditions, the test article was dynamically isolated from the environment by means of a dedicated truss-like portal structure, from which the fuselage barrel was suspended using a combination of bungee cords and springs. The suspension system was specifically designed to ensure a clear separation between rigid-body and elastic modes. The structure was excited using an electrodynamic shaker, connected to the fuselage through a stinger to ensure predominantly axial force transmission, while the input force was measured by a piezoelectric transducer located at the shaker–structure interface. The excitation signals consisted of sine sweeps and burst random inputs within the 0–400 Hz frequency range. The structural response was measured using mono-axial piezoelectric accelerometers, with a total of 72 measurement locations distributed along the fuselage barrel over three frames, each instrumented with 24 sensors (Fig. 4.8). In the same study, a simplified FE model of the fuselage barrel was also developed using one-dimensional elements only. This modelling approach is based on the observation that, in the low-frequency regime where the first elastic modes occur, the dynamic behaviour of stiffened cylindrical structures is primarily governed by frame motion, while the skin panels mainly act as distributed mass attached to the frames. Accordingly, beam-type 1D elements were adopted for the structural representation, while the skin contribution was represented through concentrated mass elements distributed along the frames. The model was discretised using 38 grid points per frame and 21 additional grid points to represent the floor section.

It should be noted that the experimental test article did not include the rear pressurization bulkhead nor the bulkhead separating the passenger cabin from the cockpit. Accordingly, these components are removed from the numerical model developed in the present work to ensure consistency with the tested configuration.

A further aspect concerns the modelling of the floor structure. In the experimental setup, some uncertainty exists regarding the structural continuity of the floor, which appears to be locally discontinuous. In the present numerical model, instead, the floor is represented as a continuous structural component along the longitudinal direction. This modelling assumption modifies the local stiffness distribution of the lower fuselage region and is expected to influence the modal response, particularly for modes involving significant deformation of the floor region.

Polito et al. report five elastic modes from the experimental modal analysis; however, only the first three are considered sufficiently reliable for validation in terms of both natural frequencies and mode shapes. These modes are therefore used as the experimental reference set for the correlation with the present FE model.

A free-free eigenvalue analysis is carried out in MSC Nastran using SOL 103. The numerical modes are extracted over the frequency range covered by the experimental reference data, and the corresponding mode shapes are examined in order to identify the modes associated with the first three experimental modes. The resulting global free-free modes are shown in Fig. 4.9.

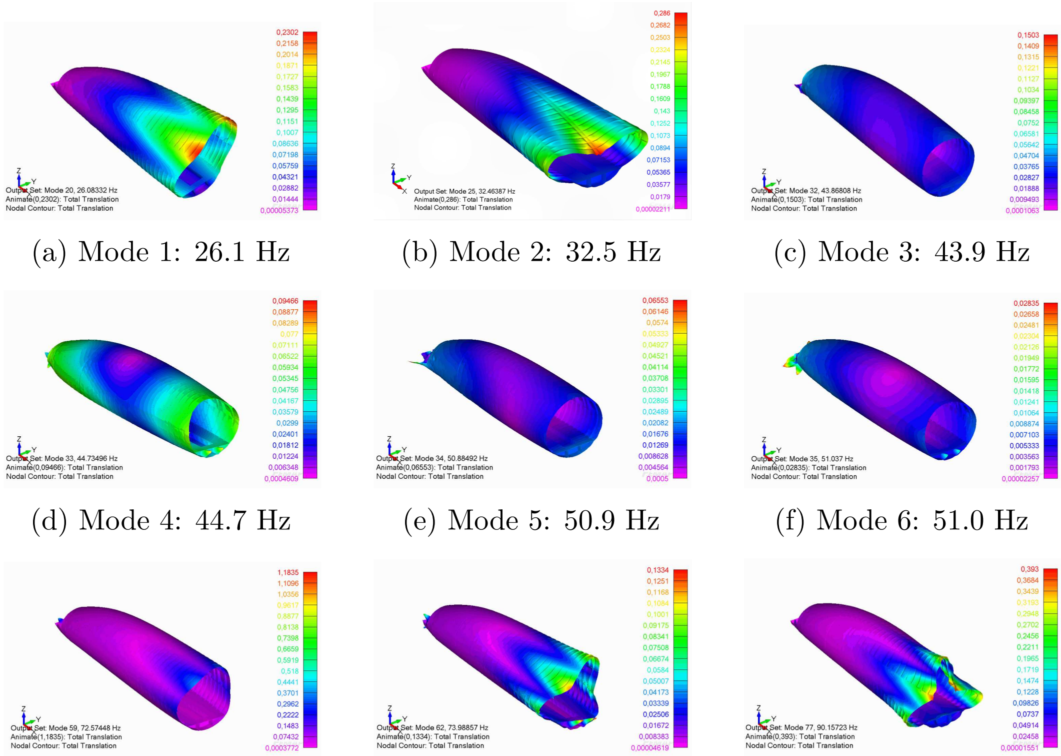

(a) Mode 1: 26.1 Hz (b) Mode 2: 32.5 Hz (c) Mode 3: 43.9 Hz

(d) Mode 4: 44.7 Hz (e) Mode 5: 50.9 Hz (f) Mode 6: 51.0 Hz

(g) Mode 7: 72.6 Hz (h) Mode 8: 74.0 Hz (i) Mode 9: 90.1 Hz

Fig. 4.9 First nine free-free global natural modes of the Piaggio P180 structural model.

Since the experimental mode shapes are referred to the instrumented fuselage barrel (see Fig. 4.8), the numerical results were post-processed over the same structural portion. This allows a direct and physically consistent comparison between numerical and experimental deformation patterns. The contour plots of the normalized mode shapes for the three identified modes, restricted to the instrumented fuselage barrel, are reported in Fig. 4.10.

The associated natural frequencies are reported in Table 4.4. The experimental values and the numerical results of the simplified 1D FE model are taken from the study by Polito et al. [85]. The table also reports the percentage errors of the present FE model with respect to both the experimental measurements and the simplified 1D reference model.

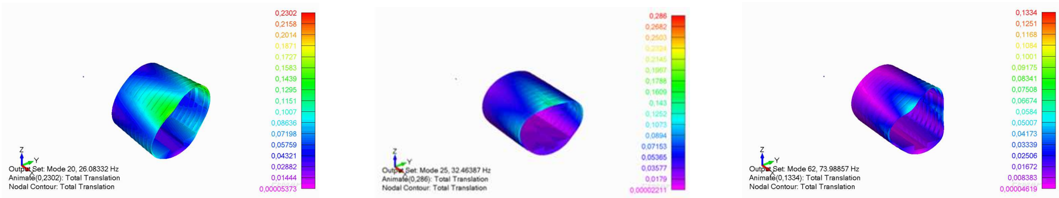

(a) First identified mode at 26.1 Hz

(b) Second identified mode at 32.5 Hz

(c) Third identified mode at 74.0 Hz

Fig. 4.10 Contour plots of the normalized mode shapes for the three numerical modes identified as corresponding to the experimental ones, restricted to the instrumented fuselage barrel.

Table 4.4 Comparison of natural frequencies between the present FE model and the reference experimental and numerical results. Percentage errors are computed with respect to the experimental values and to the 1D FE model, respectively.

	$f_{n,1}$ [Hz]	$f_{n,2}$ [Hz]	$f_{n,3}$ [Hz]
Present FE model	26.1	32.5	74.0
Experimental Analysis (EMA)	32.7	36.5	66.2
Simplified 1D FE model (1D FEA)	25.9	31.3	62.0
Error vs EMA [%]	20.2	11.0	11.8
Error vs 1D FEA [%]	0.8	3.8	19.4

Figure 4.11 compares the three experimental mode shapes with the corresponding numerical mode shapes obtained from the present FE model. The comparison is performed on the same instrumented fuselage barrel used in the experimental campaign, in order to assess the consistency of the identified deformation patterns.

The first correlated mode is predicted at 26.1 Hz, compared with the experimental value of 32.7 Hz, and corresponds to a global ovalisation of the fuselage cross-section. The numerical model correctly reproduces the dominant deformation mechanism observed experimentally, including the global ovalisation pattern and the location of the main nodal regions along the instrumented barrel. Differences are observed mainly in the lower fuselage region, where the idealisation of the passenger floor as a continuous structural component affects the local curvature of the mode shape. The frequency error is 20.2 %,

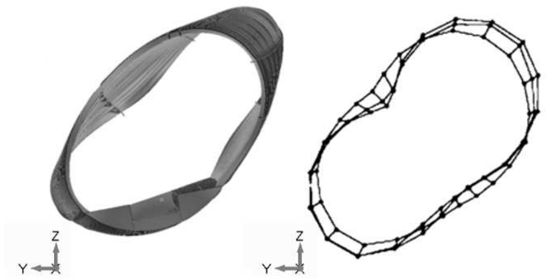

(a) First mode - Numerical: 26.1 Hz, Experimental: 32.7 Hz

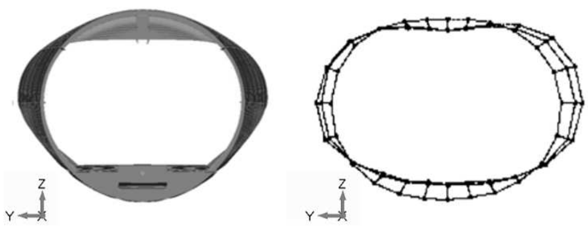

(b) Second mode - Numerical: 32.5 Hz, Experimental: 36.5 Hz

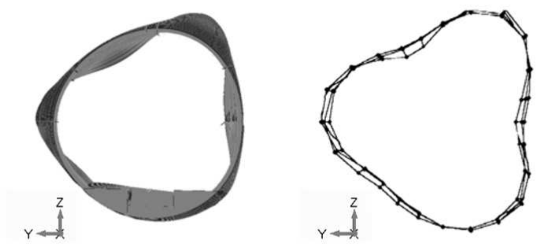

(c) Third mode - Numerical: 74.0 Hz, Experimental: 66.2 Hz

Fig. 4.11 Comparison of numerical (left) and experimental (right) mode shapes and natural frequencies: (a) first mode, (b) second mode, and (c) third mode.

corresponding to an absolute difference of approximately 6.6 Hz. Although this is the largest discrepancy among the correlated modes, the associated mode-shape agreement indicates that the numerical model captures the correct global deformation mechanism. The remaining frequency difference can be attributed to the combined effect of modelling assumptions, uncertainties in the mass and stiffness distribution of the test article and the practical limitations associated with reproducing ideal free-free boundary conditions in the experimental setup.

The second mode is predicted at 32.5 Hz compared with the experimental value of 36.5 Hz. The numerical model accurately captures the circumferential deformation pattern, reproducing the characteristic distribution of the lobes and the associated phase relationships observed in the experimental mode shape. The agreement between numerical and experimental results is very good in terms of global deformation behaviour, with only minor localized discrepancies in the floor region, where the numerical mode shape shows a reduced curvature.

The third mode exhibits a three-lobed deformation pattern and is predicted at 74.0 Hz, compared with the experimental value of 66.2 Hz. In contrast with the first two modes, the numerical frequency is overestimated. This mode involves a more pronounced deformation of the lower fuselage region; therefore, it is more sensitive to the modelling assumptions adopted for the passenger floor and the under-floor structural members. The reduced curvature observed in the numerical mode shape in the lower fuselage region is consistent with a locally stiffer representation of this part of the structure. Nevertheless, the overall three-lobed deformation mechanism and the upper-fuselage modal pattern remain well reproduced, confirming the correct correlation with the experimental mode.

Overall, the comparison demonstrates a strong correlation in terms of mode shapes, confirming that the numerical model captures the dominant structural deformation mechanisms of the cockpit–cabin fuselage assembly. The discrepancies observed in the natural frequencies, which remain within approximately $\pm 20\%$, are considered acceptable in light of the modelling assumptions and experimental uncertainties.

These discrepancies are mode-dependent and can be attributed to the combined influence of several factors. The representation of the floor as a continuous structural component, together with the non-perforated idealisation of some under-floor members, may locally modify the stiffness and mass distribution of the lower fuselage region. This effect is expected to be more relevant for modes involving significant deformation of the floor and lower fuselage. Additional differences may arise from uncertainties in the actual mass and stiffness distribution of the tested structure, including local reinforcements, joints, manufacturing details, paint and surface finishing layers not explicitly represented in the numerical model. A further contribution may be associated with the mass of the measurement instrumentation, which is not included in the numerical model. Finally, residual differences can also be related to the practical limitations associated with reproducing ideal free-free boundary conditions in the experimental setup.

It is also worth noting that the natural frequencies predicted by the present model are in close agreement with those obtained from the simplified 1D FE model reported by Polito et al., especially for the first two correlated modes, for which the differences remain below 4%. A larger discrepancy is observed for the third mode, for which the present model predicts a higher natural frequency than both the experimental result and the simplified 1D model. This difference is consistent with the higher sensitivity of the third mode to the lower fuselage and floor region, where the present model adopts a continuous floor representation and a different level of structural detail with respect to the simplified 1D formulation.

The correlation of the mode shapes, together with the consistency with the available experimental and numerical reference data, indicates that the present structural model is suitable for the subsequent low-frequency vibroacoustic analyses.

4.4 Acoustic Finite Element Model

The acoustic FE model is developed in order to reproduce the interior acoustic field of the Piaggio P180 Avanti EVO passenger cabin within the frequency range relevant to the propeller tonal excitation.

The acoustic discretisation is defined starting from the internal volume enclosed by the structural FE model. Particular attention is devoted to the accurate representation of the main cabin cavity, the geometric discontinuities introduced by the passenger floor, and the small enclosed air volumes located in the vicinity of the cabin windows. These secondary cavities are retained because their local acoustic modes may fall within the frequency range of interest and may therefore contribute to local pressure amplification phenomena.

The following sections describe the definition of the acoustic domain, the mesh-sizing criterion adopted for the fluid discretisation, the acoustic element properties and the modal verification performed to assess the consistency of the acoustic model.

4.4.1 Acoustic Cavity Definition and Modelling Assumptions

The interior acoustic analyses presented in this thesis focus on the air volume enclosed between the forward and aft pressurisation bulkheads of the passenger cabin. The acoustic domain is therefore limited to the passenger cabin region, including the door area, while the cockpit volume is not included in the present acoustic cavity.

The main acoustic cavity extends from the passenger floor level to the upper fuselage skin and includes the aisle and seating region. As a consequence, the lower part of the acoustic domain is characterised by a stepped geometry generated by the presence of the cabin floor. In addition, the continuously varying fuselage cross-section of the Piaggio P180 Avanti EVO causes the cavity to deviate from an ideal cylindrical shape (Fig. 4.12).

Further deviations from a regular geometry are introduced by local structural features such as emergency exit window (Fig. 4.13a) and the passenger door

(a) (b)

Fig. 4.12 Acoustic cavity geometry: (a) lateral view of the passenger cabin, including the door region; (b) rear view of the cavity, highlighting the non-circular cross-sectional shape.

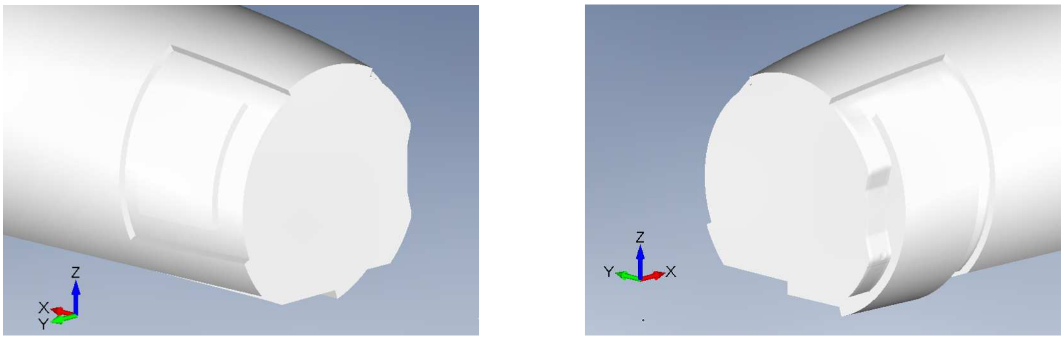

(a) (b)

Fig. 4.13 Acoustic cavity details: (a) emergency exit window region; (b) door region. The omitted recessed cavities around the openings are visible as local missing regions.

(Fig. 4.13b). These regions generate local geometric irregularities and cross-sectional variations, especially in the forward part of the cabin.

In the present model, the small recessed acoustic volumes surrounding the passenger door and the emergency exit frame are neglected in order to limit the geometrical complexity of the acoustic domain.

In addition to the main cabin cavity, the acoustic model also includes the small enclosed air volumes located around the passenger windows. These cavities are bounded by the fuselage skin, the adjacent frames and stringers, and the local window-frame structure. Their inclusion is motivated by the possibility of local acoustic resonances within the investigated frequency range (Fig. 4.14).

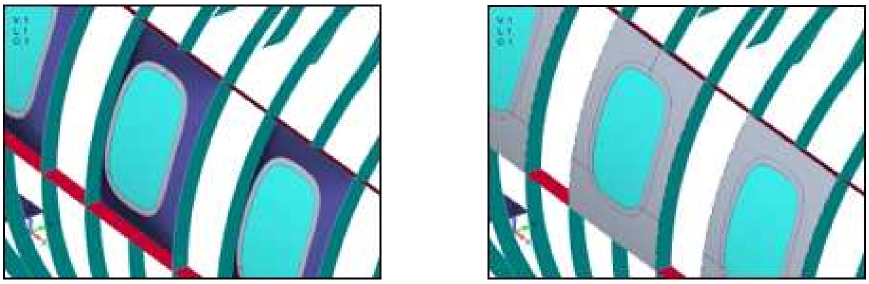

(a) Structural modelling of stringers and frames around a window frame

(b) Structural modelling of the fuselage skin around the window frames

Fig. 4.14 Structural configuration in the vicinity of the cabin windows: (a) detail of adjacent stringers and frames, with the window frames highlighted; (b) enclosing fuselage skin.

The complete acoustic domain therefore consists of the main passenger cabin cavity, with an overall length of approximately 4.7 m and an average diameter of approximately 1.87 m, together with 13 additional local cavities surrounding the passenger windows. Six of these cavities are located on the fuselage side where the passenger door is installed, while seven are located on the opposite side, corresponding to six standard windows and the emergency exit window.

4.4.2 Acoustic Mesh-Sizing Methodology

The spatial resolution of the acoustic FE mesh is defined according to the acoustic wavelength criterion. For a harmonic acoustic field propagating in air, the wavelength is given by

$$\lambda_a = \frac{c_0}{f}, \tag{4.8}$$

where $c_0 = 343$ m/s is the speed of sound in air and f is the frequency. The acoustic mesh-sizing procedure is based on the extended convergence frequency already adopted for the structural model $f_{conv} = 900$ Hz. By requiring nine linear elements per acoustic wavelength, the maximum admissible acoustic element size becomes

$$h_{a,\max} = \frac{\lambda_a}{9} = \frac{c_0}{9 f_{\mathrm{conv}}} = \frac{343}{9 \times 900} \simeq 42 \text{ mm.} \tag{4.9}$$

Since the admissible acoustic element size is significantly larger than the characteristic structural element size, a non-uniform acoustic mesh strategy is adopted. A finer discretisation is used close to the fluid–structure interfaces to preserve compatibility with the structural mesh, while the mesh is gradually coarsened towards the cavity core according to the acoustic wavelength criterion.

The acoustic domain is therefore subdivided into three regions:

1. an interface-matching layer adjacent to the structural boundaries, where the acoustic mesh matches the structural mesh along the fluid–structure interfaces;
2. a transition region, where the acoustic element size is gradually increased moving away from the structural boundaries;
3. a core acoustic region, where a more uniform discretisation with the target acoustic element size is adopted.

This strategy allows the structural vibration field to be accurately transferred to the acoustic domain at the coupled boundaries, while avoiding an excessive refinement of the internal fluid volume. The mesh transition is generated gradually in order to avoid abrupt variations in element size, which could negatively affect the accuracy of the acoustic pressure field (Fig. 4.15).

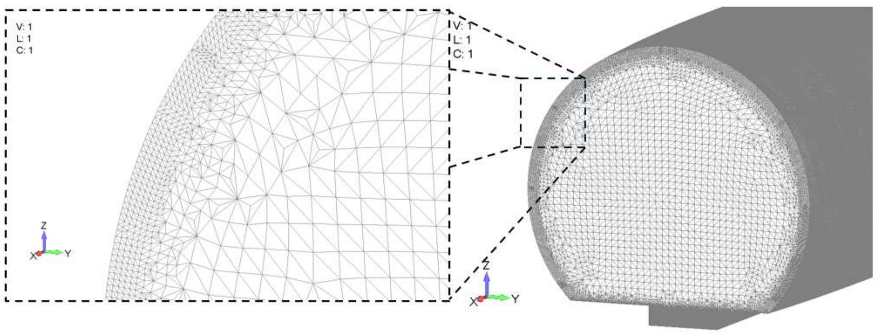

Fig. 4.15 Acoustic finite element model of the Piaggio P180 cabin cavity and detailed view of the transition region.

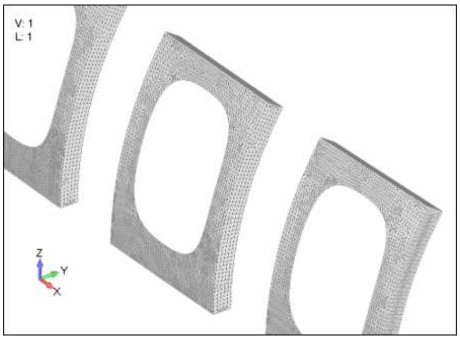

Fig. 4.16 Acoustic finite element model of a local cavity in the vicinity of a cabin window.

Due to the limited dimensions of the local cavities surrounding the cabin windows, no mesh coarsening is introduced in these regions. For each window cavity, the acoustic mesh is generated to match the structural discretisation at the boundaries, and the same characteristic element size is maintained throughout the small cavity volume.

4.4.3 Acoustic Element Type and Property Definition

The acoustic domain is discretised using 3D linear acoustic finite elements. Both the main cabin cavity and the local window cavities are modelled as inviscid, compressible fluid domains. The acoustic medium is assumed to be homogeneous air under standard atmospheric conditions, with speed of sound $c_0 = 343\ \mathrm{m\,s^{-1}}$ and density $\rho_0 = 1.225\ \mathrm{kg\,m^{-3}}$.

The fluid volume is discretised using NASTRAN `CTETRA` acoustic elements, and the corresponding fluid properties are assigned through a `MAT10` material definition. The use of tetrahedral acoustic elements allows the complex cabin geometry, including the local window cavities and geometrical transitions, to be represented consistently within the finite element acoustic domain.

The final acoustic discretisation comprises approximately 15×10^6 acoustic elements and about 3×10^6 acoustic degrees of freedom.

4.4.4 Acoustic Natural Frequencies and Model Verification

The acoustic FE model is verified by comparing the numerically computed acoustic eigenfrequencies with analytical solutions for an ideal cylindrical cavity. Although the actual Piaggio P180 cabin cavity deviates from a perfect cylinder because of its varying cross-section, the presence of the floor, local discontinuities and secondary window cavities, the cylindrical approximation provides a useful reference for assessing the consistency of the acoustic discretisation.

For the analytical comparison, the passenger cabin is idealised as an equivalent rigid-walled cylindrical cavity. The equivalent cylinder is defined by preserving the same longitudinal length as the actual cabin cavity, while its diameter is taken as the average diameter of the passenger cabin cross-section.

The acoustic eigenvalue problem is solved numerically (MSC NASTRAN, SOL 107 - SEMODES) under the assumption of an inviscid fluid bounded by rigid walls.

Both longitudinal modes and modes with transverse pressure variations are considered in the comparison.

Longitudinal Acoustic Modes

Longitudinal acoustic modes are characterised by pressure oscillations mainly occurring along the fuselage axis, with an approximately uniform pressure distribution over the cross-section.

For an ideal rigid-walled cylindrical cavity of length L, the corresponding natural frequencies are given by

$$f_n = \frac{c_0}{2L} n, \qquad n = 1, 2, 3, \ldots \tag{4.10}$$

where n is the longitudinal mode order.

The numerical eigenfrequencies associated with the first longitudinal modes are reported in Table 4.5, together with the corresponding analytical values and

Table 4.5 Analytical and numerical natural frequencies of the first seven longitudinal acoustic modes.

Mode	**Analytical** [Hz]	**FE Analysis** [Hz]	**Difference** [%]
$n = 1$	36.8	37.8	2.7
$n = 2$	73.6	73.7	0.1
$n = 3$	110.4	109.8	0.5
$n = 4$	147.2	146.7	0.3
$n = 5$	184.0	183.3	0.4
$n = 6$	220.8	219.6	0.5
$n = 7$	257.6	253.7	1.5

the percentage differences between the two solutions. The percentage difference is computed as

$$\Delta f = \frac{|f_{\mathrm{FE}} - f_{\mathrm{AF}}|}{f_{\mathrm{AF}}} \times 100 \tag{4.11}$$

where f_{FE} denotes the finite element acoustic eigenfrequency and f_{AF} denotes the corresponding analytical frequency of the equivalent rigid-walled cylindrical cavity.

The numerical results show very good agreement with the analytical reference. The maximum deviation remains below 3% for the modes considered, confirming the adequacy of the acoustic spatial discretizations and the correct assignment of the fluid material properties. Exact agreement with the analytical solution is not expected, since the actual acoustic cavity is not cylindrical.

As shown in the contour plots of Fig. 4.17, the first two longitudinal modes exhibit pressure maxima at both bulkheads, in agreement with the ideal cylindrical solution. However, for higher-order modes this behaviour progressively disappears, and the pressure field no longer presents antinodes at the end boundaries. The deviations from the ideal solution are mainly caused by the non-circular cross-section, the longitudinal variation of the fuselage geometry, the presence of the cabin floor and the local discontinuities associated with openings and secondary cavities. These geometrical features introduce a coupling between axial and transverse pressure variations, especially for higher-order modes.

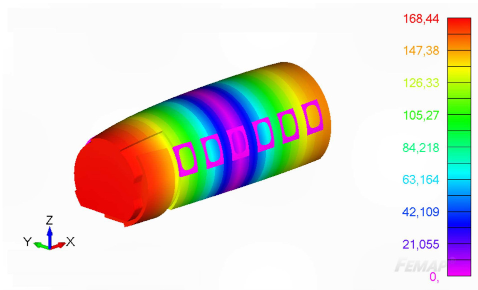

(a) 37.8 Hz

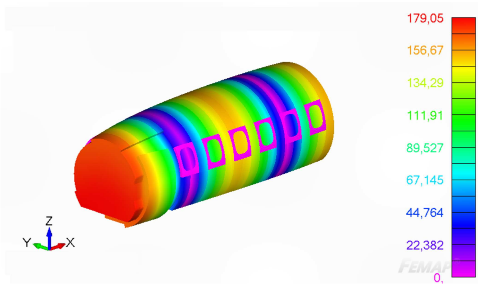

(b) 73.7 Hz

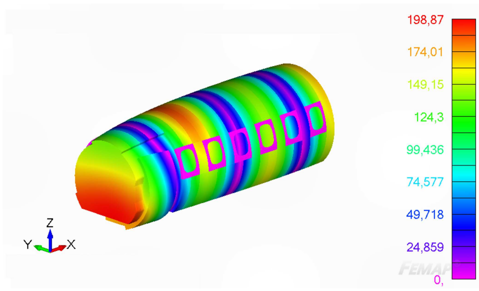

(c) 109.8 Hz

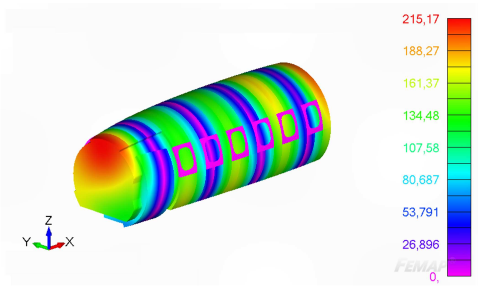

(d) 146.7 Hz

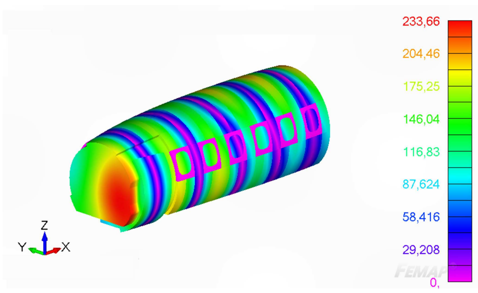

(e) 183.3 Hz

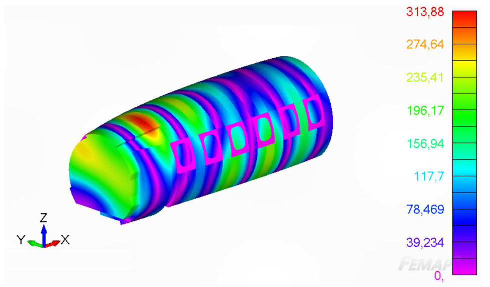

(f) 219.6 Hz

Fig. 4.17 First six numerical longitudinal acoustic mode shapes and corresponding natural frequencies.

Modes with Transverse Components

The acoustic modal verification is further extended to modes involving transverse pressure variations.

For an ideal rigid-walled cylindrical cavity, these modes are described by analytical solutions of the Helmholtz equation expressed in terms of Bessel functions in the cross-sectional plane and sinusoidal functions along the axial direction. The corresponding modal shapes are characterised by axial, radial and circumferential modal indices, denoted by the triplet

$$(n_x, n_r, n_\theta), \tag{4.12}$$

where n_x denotes the number of axial nodal planes, n_r identifies the radial order, and n_θ denotes the circumferential order of the pressure distribution. In a perfectly cylindrical cavity, the geometrical symmetry of the cross-section leads to degenerate modal pairs associated with orthogonal orientations of the same transverse pressure pattern.

The actual Piaggio P180 cabin cavity differs from this ideal configuration. The presence of the passenger floor breaks the cross-sectional symmetry with respect to the horizontal plane, while a certain degree of symmetry is approximately retained with respect to the vertical longitudinal plane. In addition, the cross-section varies along the cabin length and local geometrical discontinuities are introduced by the door region, the emergency exit window and the secondary window cavities. These features modify the acoustic modal field and cause a splitting of theoretically degenerate modal pairs.

For this reason, the comparison between analytical and numerical modes with transverse components cannot be interpreted as a one-to-one exact validation of the real cavity against the ideal cylindrical solution. Rather, it provides a verification of the acoustic mesh consistency and of the ability of the numerical model to reproduce the expected modal families within the considered frequency range.

Table 4.6 reports the comparison between analytical frequencies and finite element results for selected acoustic modes up to approximately 300 Hz. The percentage difference is computed as

$$\Delta f = \frac{|f_{\mathrm{FE}} - f_{\mathrm{AF}}|}{f_{\mathrm{AF}}} \times 100 \tag{4.13}$$

where f_{FE} denotes the finite element acoustic eigenfrequency and f_{AF} denotes the corresponding analytical frequency of the equivalent rigid-walled cylindrical cavity.

Modes marked with an asterisk are characterised by a vertical nodal plane. These modes are generally less affected by the loss of horizontal symmetry induced by the cabin floor and therefore exhibit a closer agreement with the analytical cylindrical reference.

The results reported in Table 4.6 show that the FE model correctly reproduces the main transverse modal families expected for a cylindrical cavity. The agreement is particularly good for modes whose nodal structure is compatible with the residual symmetry of the actual cabin geometry. In particular, modes characterised by a vertical nodal plane generally exhibit smaller discrepancies with respect to the analytical solution.

The largest differences are observed for modal pairs that are degenerate in the ideal cylindrical cavity but become separated in the numerical model. This behaviour is physically consistent with the loss of cross-sectional symmetry introduced by the cabin floor and by the non-circular shape of the real acoustic domain. Therefore, the observed frequency splitting should not be interpreted as a numerical error, but rather as a direct consequence of the actual cabin geometry.

At increasing frequency, the identification of a unique correspondence between numerical and analytical modes becomes progressively more complex. Higher-order modes involve multiple nodal planes and combined axial, radial and circumferential pressure variations. In this frequency range, the pressure field is more strongly affected by geometrical irregularities, local changes in cross-section and the presence of secondary cavities. As a consequence, some numerical modes do not have a direct counterpart in the ideal cylindrical solution. The analytical classification reported in the comparison should therefore be regarded as an indication of the closest reference modal family, rather than as a strict one-to-one modal correspondence.

Table 4.6 Comparison between analytical and finite element natural frequencies for selected acoustic modes with transverse components. The modal indices (n_x, n_r, n_θ) denote the axial, radial and circumferential modal orders, respectively. Modes marked with an asterisk are characterised by a vertical nodal plane.

Mode	**Analytical** [Hz]	**FE Analysis** [Hz]	**Difference** [%]
$(0,1,0)^*$	107.5	103.5	3.7
$(0,1,0)$	107.5	114.3	6.3
$(1,1,0)^*$	113.6	114.8	1.1
$(1,1,0)$	113.6	123.9	9.1
$(2,1,0)^*$	130.2	130.6	0.3
$(2,1,0)$	130.2	138.7	6.5
$(3,1,0)^*$	154.1	152.9	0.8
$(3,1,0)$	154.1	160.6	4.2
$(0,2,0)$	178.3	176.2	1.2
$(0,2,0)^*$	178.3	179.6	0.7
$(4,1,0)^*$	182.3	180.4	1.0
$(1,2,0)$	182.1	186.1	2.2
$(4,1,0)$	182.3	187.3	2.7
$(1,2,0)^*$	182.1	189.7	4.2
$(2,2,0)^*$	192.9	198.5	2.9
$(2,2,0)$	192.9	202.3	4.9
$(3,2,0)^*$	209.7	210.7	0.5
–	–	213.9	–
$(5,1,0)^*$	213.1	217.0	1.8
$(3,2,0)$	209.7	217.8	3.9
$(0,0,1)$	223.7	224.4	0.3
$(4,2,0)$	231.2	232.2	0.4
$(1,0,1)$	226.7	233.6	3.0
...	...	...	...
$(5,0,1)$	289.7	295.3	1.9
$(4,3,0)$	286.1	298.6	4.4

The contour plots reported in Fig. 4.18 show the first eight non-axial acoustic modes. These results clearly highlight the frequency splitting of modal pairs that would be degenerate in a perfectly cylindrical cavity. Modes characterised by a vertical nodal plane retain a pressure distribution closer to the ideal analytical pattern, whereas their paired counterparts are more strongly affected by the asymmetry introduced by the cabin floor.

Selected higher-frequency pressure fields are reported in Fig. 4.19. Although the modal patterns become progressively more complex, the acoustic pressure distributions remain smooth and well resolved over the main cabin cavity. This confirms that the adopted acoustic mesh is sufficiently refined to capture the transverse pressure variations occurring within the frequency range considered.

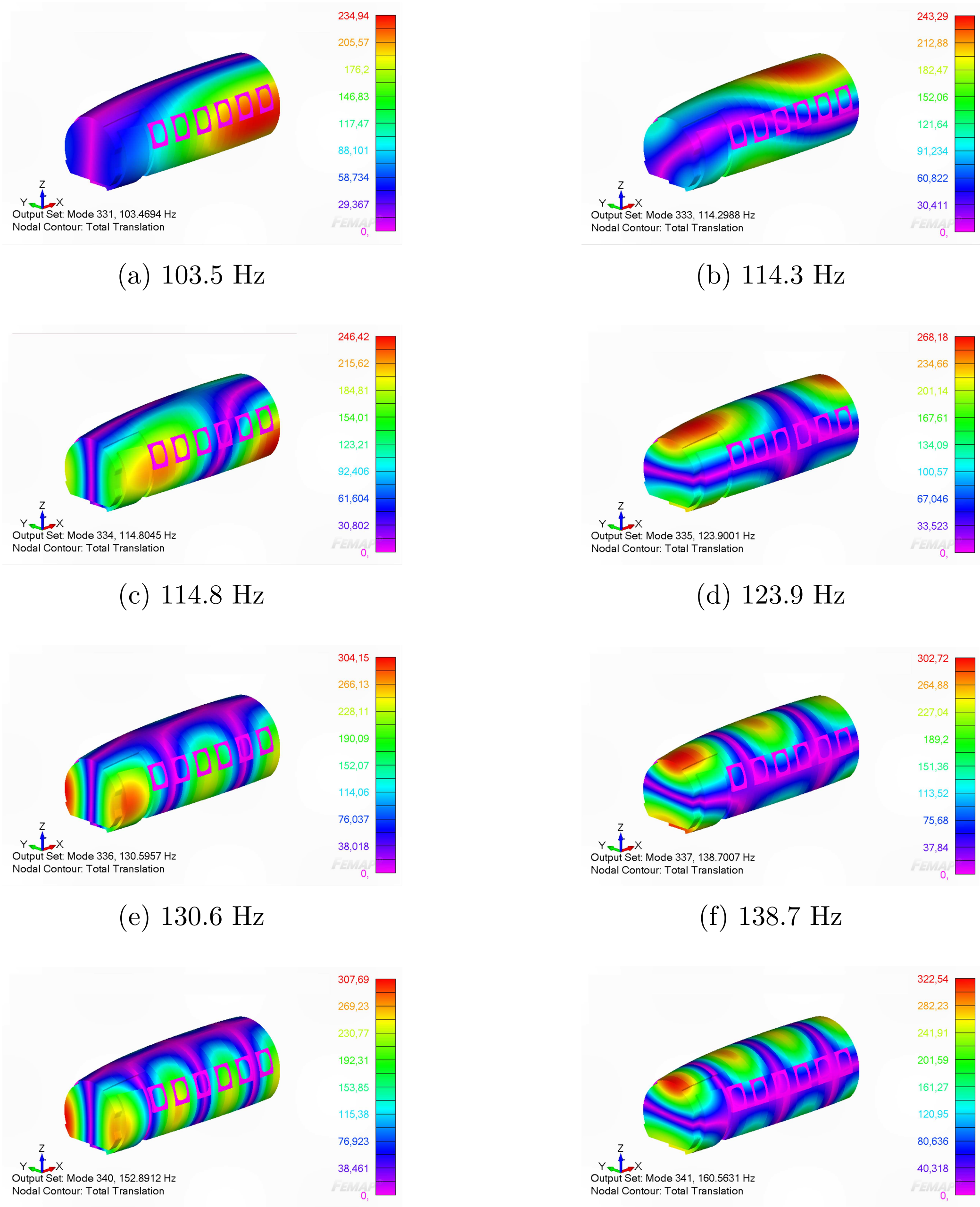

(a) 103.5 Hz (b) 114.3 Hz

(c) 114.8 Hz (d) 123.9 Hz

(e) 130.6 Hz (f) 138.7 Hz

(g) 152.9 Hz (h) 160.6 Hz

Fig. 4.18 Contour plots of the acoustic pressure field for the first eight non-axial numerical modes.

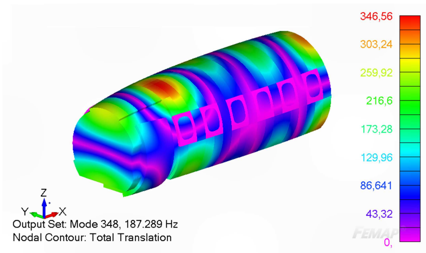

(a) 187.3 Hz

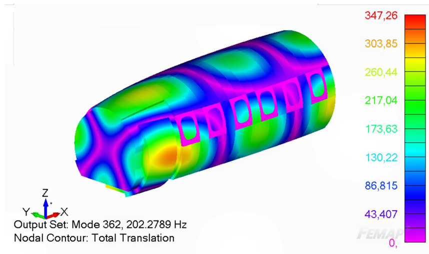

(b) 202.3 Hz

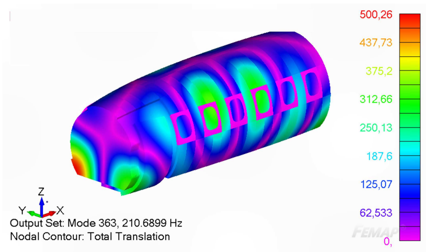

(c) 210.7 Hz

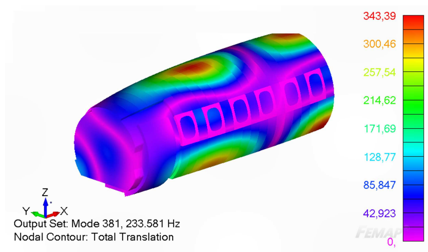

(d) 233.6 Hz (view 1)

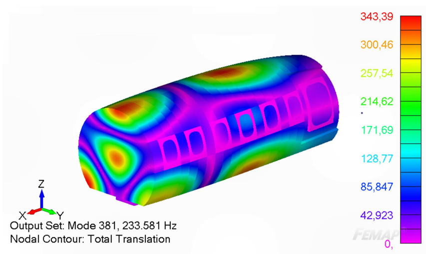

(e) 233.6 Hz (view 2)

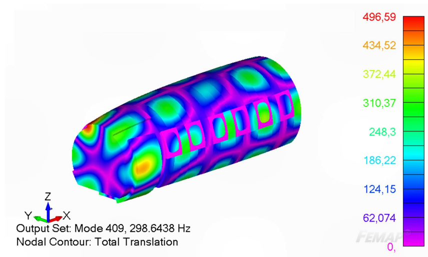

(f) 298.6 Hz

Fig. 4.19 Contour plots of the acoustic pressure field for selected higher-order non-axial numerical modes. The mode at 233.6 Hz is shown from two different views to highlight its three-dimensional pressure distribution.

Local Acoustic Modes of Window Cavities

In addition to the global acoustic modes of the main passenger cabin cavity, the acoustic model also includes the local air volumes associated with the window regions. The inclusion of these cavities in the acoustic FE model is motivated by the presence of local acoustic resonances within the frequency range of interest.

Figure 4.20 reports representative local acoustic modes identified in the window-related cavities. The modes in Figs. 4.20a–4.20b are associated with the cavity

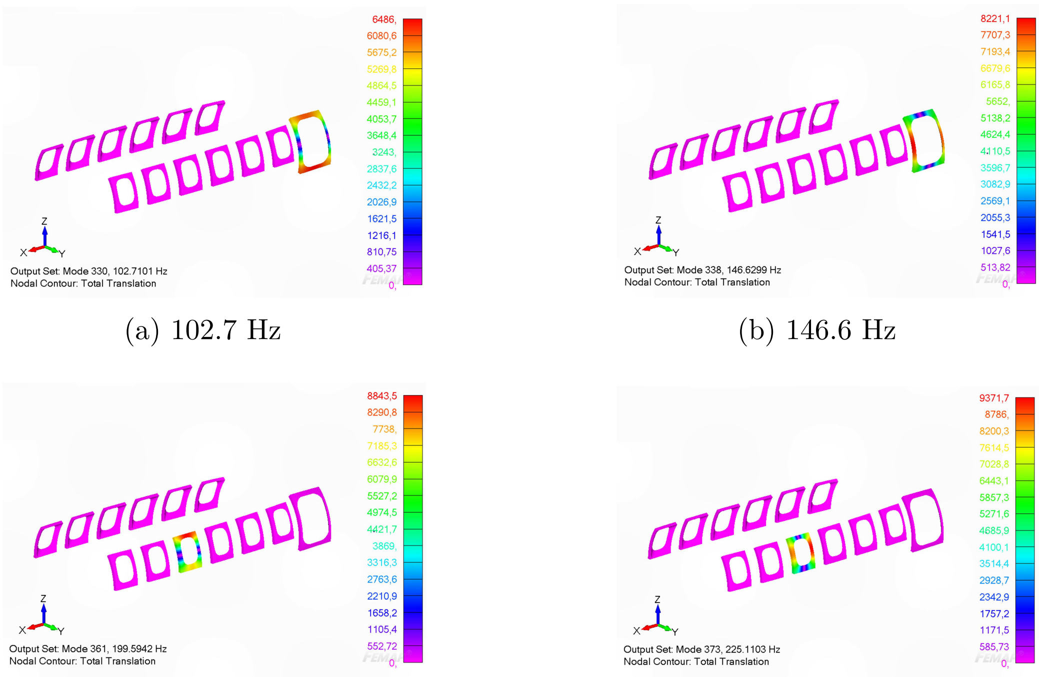

(a) 102.7 Hz

(b) 146.6 Hz

(c) 199.6 Hz

(d) 225.1 Hz

Fig. 4.20 Contour plots of the acoustic pressure field for the first two acoustic modes of the cavity around the emergency exit window (a) - (b) and the window cavities (c) - (d).

surrounding the emergency exit window, whereas those in Figs. 4.20c–4.20d correspond to the standard window cavities.

These results confirm that the window-related cavities introduce additional local acoustic modal content within the frequency range considered. Although spatially confined, these modes may locally modify the pressure field in the vicinity of the windows.

Chapter 5

Preliminary Verification of Structural–Acoustic Coupling

Following the structural modal correlation and the acoustic modal verification presented in the previous chapter, a preliminary verification of the coupled vibroacoustic model is carried out.

A forced frequency-response analysis is performed on a reduced model of the Piaggio P180 Avanti EVO fuselage, restricted to the passenger-cabin region. The objective of this analysis is not to reproduce a specific experimental or operational condition, but to verify the numerical implementation of the structural–acoustic coupling and to assess whether the coupled model produces a physically consistent vibroacoustic response. For this purpose, a controlled harmonic pressure excitation is applied to the fuselage skin. The resulting structural displacement and acoustic pressure fields are analysed in order to identify the main coupling mechanisms, including acoustic cavity resonances, structural modal participation and receiver-dependent pressure distributions. The corresponding NR is then evaluated as a preliminary indicator of exterior-to-interior transmission behaviour.

5.1 Coupled Vibroacoustic Analysis

A frequency response analysis (MSC Nastran SOL 111) is carried out to investigate the coupled vibroacoustic behaviour of the Piaggio P180 passenger cabin model (cockpit excluded). Both bulkheads are omitted, and fully clamped boundary conditions are applied at the fore and aft fuselage frames. The internal acoustic cavity is assumed to be fully enclosed by acoustically rigid boundaries, with no absorbing treatments included. The excitation frequency range extended from 25 Hz to 301 Hz with a uniform increment of 3 Hz, ensuring sufficient resolution to capture closely spaced resonances and structural–acoustic modal interactions occurring in the low-frequency regime. A spatially uniform, in-phase pressure field of amplitude 0.1 Pa is applied normal to all fuselage skin elements. This loading does not represent a specific physical source, but provides a controlled harmonic excitation over the analysed frequency range to assess the transmission behaviour of the coupled system.

The solution is obtained using a modal superposition approach, retaining all structural and acoustic eigenvectors up to 600 Hz, i.e. approximately twice the maximum forcing frequency, in order to limit modal truncation effects. The governing coupled vibroacoustic equations are presented in Chapter 2. A constant modal damping ratio of 2% is introduced in the numerical model, consistent with typical values for lightly damped aluminium airframe structures. The analysis is performed on CIRA HPC node (36-core Intel Xeon, 256 GB RAM) using MSC Nastran shared-memory parallelisation. The full analysis required approximately 17 hours of wall-clock time.

To support interpretation of the forced response, a preliminary eigenvalue analysis (MSC NASTRAN, SOL 103) is performed under identical boundary conditions. The resulting structural and acoustic natural frequencies and mode shapes are used as a reference framework for interpreting the forced vibroacoustic response discussed in the following. The first structural mode, occurring at 87 Hz, is shown in Figure 5.1.

Figure 5.2 shows structural displacements and acoustic pressure fields at two representative excitation frequencies, selected to highlight the dominant coupling mechanisms.
At 37 Hz, corresponding to the first longitudinal acoustic mode of the cavity (see Section 4.4.4), the pressure field exhibits a half-wavelength standing wave pattern, characterised by a nodal plane at mid-cabin and a progressive increase in pressure amplitude towards the fore and aft ends of the acoustic cavity, where pressure maxima are observed. Structural deformation remains limited, with a

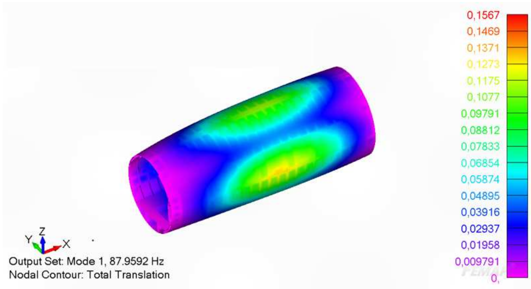

Fig. 5.1 First structural mode of the Piaggio P180 Avanti EVO passenger cabin at 87 Hz, obtained under fully clamped boundary conditions at the fore and aft fuselage frames and with bulkheads removed.

maximum displacement of approximately 8×10^{-9} m. The maximum acoustic pressure inside the cabin is about 0.0025 Pa, corresponding to approximately 39 dB after conversion from peak amplitude to root mean square (RMS) values. At 87 Hz, coinciding with the first global structural bending mode of the passenger cabin, the fuselage undergoes larger deformation compared to the 37 Hz case. The maximum displacement reaches approximately 5×10^{-8}, i.e. about one order of magnitude higher. As expected, the displacement contour closely matches the first structural mode shape previously identified (Figure 5.1), with regions of maximum and minimum displacement consistent with the modal distribution. The acoustic pressure field, strongly coupled with the structural response, exhibits pressure extrema located in proximity of the structural antinodes. The maximum acoustic pressure inside the cabin reaches approximately 0.0097 Pa, corresponding to about 50.7 dB.

These results demonstrate that the coupled model correctly captures the interaction between structural deformation and the acoustic pressure field, reproducing the expected vibroacoustic coupling mechanisms.

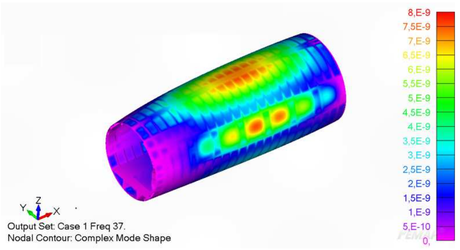

(a) Total displacement (m), 37 Hz

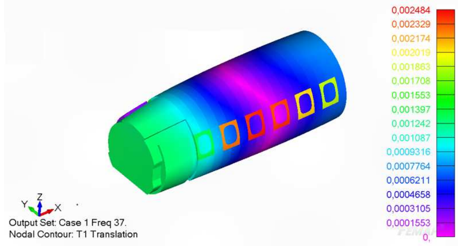

(b) Acoustic pressure (Pa), 37 Hz

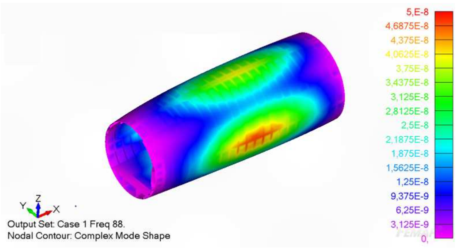

(c) Total displacement (m), 87 Hz

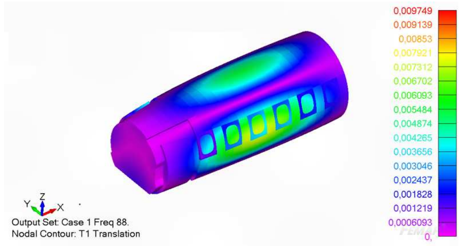

(d) Acoustic pressure (Pa), 87 Hz

Fig. 5.2 Contour plots of the forced response at two resonance frequencies:
37 Hz (first acoustic cavity mode): (a) structural total displacement, (b) acoustic pressure;
87 Hz (first structural mode): (c) structural total displacement, (d) acoustic pressure.

5.1.1 Noise Reduction Evaluation

The forced vibroacoustic response is further analysed in terms of NR, in order to quantify the transmission characteristics of the airframe in the 25–301 Hz frequency range. The evaluation is performed at fluid nodes belonging to a horizontal plane corresponding to the nominal ear height of a seated passenger, with each seat treated as a discrete receiver.

For each location, the interior pressure magnitude $|p(f)|$, obtained from the previously computed forced analysis, is used to evaluate the corresponding sound pressure levels $|L_{in}(f)|$ according to:

$$L(f) = 20\log_{10}\left(\frac{|p_{rms}(f)|}{p_{\text{ref}}}\right), \qquad p_{\text{rms}}(f) = \frac{|p(f)|}{\sqrt{2}}, \qquad p_{\text{ref}} = 20\ \mu\text{Pa}, \quad (5.1)$$

The NR at each receiver is then defined as:

$$\mathrm{NR}(f) = L_{\mathrm{out}}(f) - L_{\mathrm{in}}(f), \tag{5.2}$$

where $L_{out}(f)$ is the SPL associated with the imposed external pressure amplitude $p_{out}(f) = 0.1$ Pa.
The selected amplitude value (0.1 Pa) represents a convenient reference level, as the analysis focuses on relative noise attenuation rather than absolute SPL. To obtain a spatially representative indicator, the pressure field on a longitudinal plane at ear height is averaged in an RMS sense:

$$p_{\mathrm{rms},avg}(f) = \sqrt{\frac{1}{N}\sum_{i=1}^{N}\frac{|p_i(f)|^2}{2}}. \tag{5.3}$$

The NR spectra computed at the seven passenger locations indicated in Figure 5.3 are shown in Fig. 5.4, together with the value averaged over the ear-level plane. According to Eq. 5.2, the ordinate shows NR in decibels, namely the difference between exterior and interior SPL, while the abscissa spans 25 Hz to 301 Hz. A Makima interpolation is applied to improve visual readability without introducing artificial narrow-band features. It should be noted that minima in NR correspond to increased interior pressure levels, indicating efficient transmission of acoustic energy into the cabin. Conversely, higher NR values are associated with reduced interior pressure levels, reflecting improved attenuation performance of the airframe.

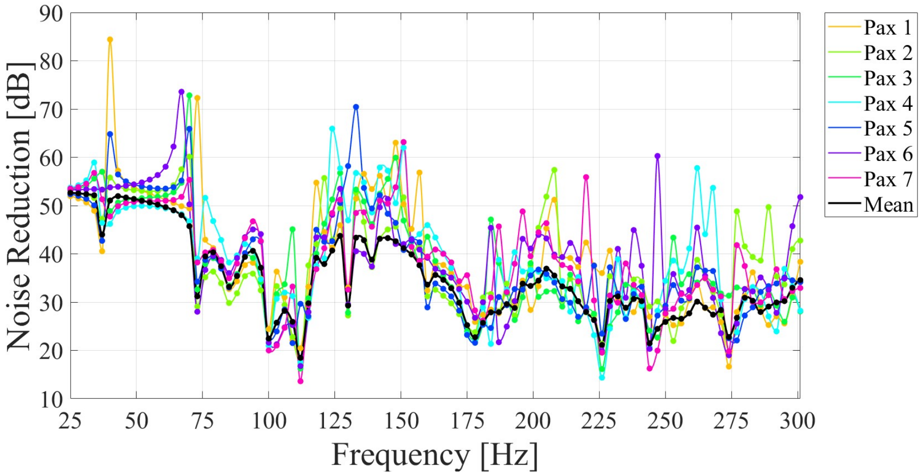

Fig. 5.4 Noise reduction spectra of the Piaggio P180 passenger cabin airframe evaluated at the seven passenger receiver locations shown in Fig. 5.3. Curves labelled Pax 1 to Pax 7 refer to individual receivers, while the black curve labelled as Mean represents the spatially averaged response over the ear-level plane.

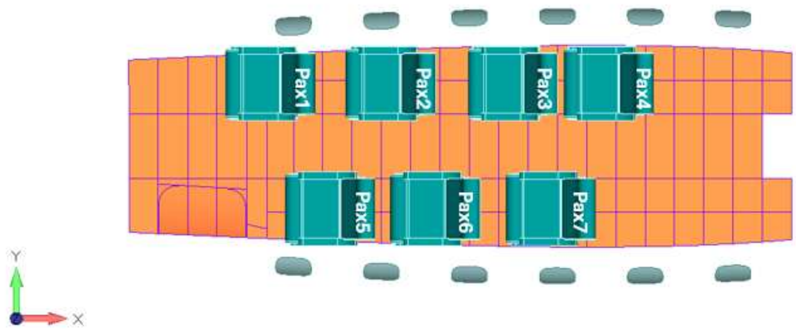

Fig. 5.3 Passenger cabin seating layout, with seats represented according to the actual geometry and position of the Piaggio P180 Avanti EVO cabin configuration.

In the sub-resonant regime, up to approximately 87 Hz, corresponding to the first structural natural frequency, the response is governed by the stiffness-controlled behaviour of the structure. As shown in Figure 5.4, the mean NR (black curve) decreases from about 52 dB at 25 Hz to approximately 35 dB in proximity of the first structural bending frequency at 87 Hz. Superimposed on this response are peaks and troughs associated with low-order acoustic eigenmodes of the cabin. As expected, pronounced maxima in SPL, and corresponding minima in NR, occur at 37 Hz and 73 Hz, corresponding to the first and second longitudinal acoustic modes, respectively. At 37 Hz, as previously shown in Figure 5.2b, the pressure field exhibits a single nodal plane approximately located at mid-cabin (Figure 5.5a). Seat 3, located in the vicinity of this nodal region, experiences the lowest pressure levels among all passenger locations at this frequency, and consequently the highest NR. In contrast, seats positioned near pressure antinodes exhibit reduced NR. At 73 Hz, corresponding to the second longitudinal acoustic mode of the cavity, the pressure field is characterised by two nodal planes (Figure 5.5b). Passengers located away from these nodal regions, i.e. near pressure antinodes, experience higher pressure levels and consequently reduced NR. In contrast, Passenger 1, positioned along one of the nodal planes, experiences the lowest pressure levels and therefore the highest NR, reaching approximately 72 dB. This represents the maximum NR observed for this passenger over the analysed frequency range, except for the peak value of about 84 dB at 40 Hz.

Once the excitation frequency approaches and exceeds the first structural bending natural frequency of the fuselage, structural participation becomes more significant and the response is increasingly governed by coupled structural–acoustic interactions. A marked reduction in NR is observed in the vicinity of the first structural natural frequency across all passenger locations. It should be noted that the minimum NR occurs at approximately 85 Hz, slightly below the structural natural frequency ($\approx 87\,\mathrm{Hz}$). This shift can be attributed to the combined effects of structural damping and fluid–structure coupling, which modify the resonance condition of the coupled system.

From 90 Hz to 180 Hz, the NR response exhibits pronounced variability in the frequency domain, with sharp peaks and dips whose amplitude is strongly dependent on the receiver position. A particularly deep minimum occurs at 130 Hz, corresponding to an acoustic cavity natural mode characterised by one longitudinal and two transverse nodal planes. The corresponding pressure contour clearly reflects this modal shape (Figure 5.5c). At this frequency, Passenger 5, located within a nodal region, exhibits the highest NR among all seating positions. Passenger 4, also positioned close to a nodal plane, shows similarly elevated NR value. Conversely, seats located in antinodal regions experience significantly reduced NR, due to increased local pressure amplitudes. Above approximately 180 Hz, the response is dominated by higher-order structural and acoustic modes. The longitudinally averaged NR stabilises between 20 dB and 37 dB, although pronounced maxima and minima persist. For instance, at 244 Hz, corresponding to an acoustic cavity natural frequency, the acoustic field exhibits a spatial distribution consistent with the corresponding mode, characterised by multiple transverse and one longitudinal nodal planes, resulting in the subdivision of the cabin into several lobed regions (Figure 5.5d). Due to the increased number of nodal planes, the spatial variation in NR is significantly reduced. As a result, relatively low NR values are observed across all passenger locations.

In conclusion, the forced vibroacoustic analysis and the corresponding evaluation of the airframe performance in terms of NR provide a physically consistent numerical framework for the subsequent numerical–experimental validation and further frequency-domain simulations. Over the entire 25–301 Hz frequency range, the mean NR remains above approximately 20 dB for the idealised excitation condition considered here. This result should not be interpreted as a definitive prediction of the aircraft transmission performance, but rather as an indication that the coupled model produces physically consistent vibroacoustic response. In particular, maxima in the internal SPL, and consequently minima in NR, occur in correspondence with structural and acoustic resonant conditions. At a given excitation frequency, local variations of several decibels are observed depending on the spatial distribution of the acoustic field. This behaviour confirms the importance of receiver position and acoustic modal structure in low-frequency cabin-noise prediction.

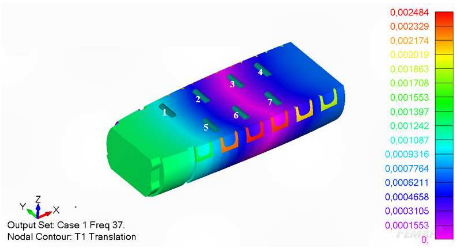

(a) Acoustic pressure (Pa), 37 Hz

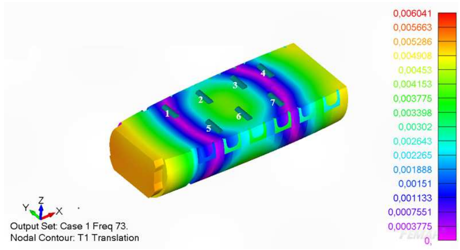

(b) Acoustic pressure (Pa), 73 Hz

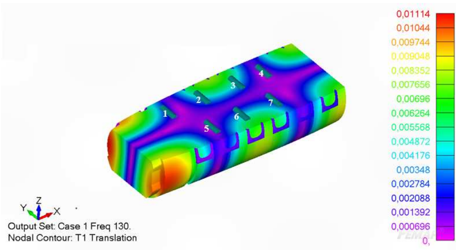

(c) Acoustic pressure (Pa), 130 Hz

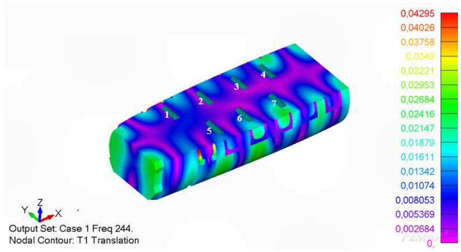

(d) Acoustic pressure (Pa), 244 Hz

Fig. 5.5 Contour plots of acoustic pressure on a plane at ear height for four excitation frequencies corresponding to acoustic cavity natural frequencies: (a) 37 Hz, (b) 73 Hz, (c) 130 Hz, and (d) 244 Hz.

Chapter 6

Numerical–Experimental Validation of the Vibroacoustic Model

Following the preliminary verification of the coupled structural–acoustic model presented in Chapter 5, the present Chapter addresses the numerical–experimental validation of the vibroacoustic model through comparison with data from a full-scale laboratory acoustic test campaign.

The experimental data used for validation are obtained from the same full-scale Piaggio P180 fuselage barrel test article considered for the structural modal correlation presented in Section 4.3.4. In the acoustic test campaign, the fuselage was excited by an external loudspeaker, while the interior response was measured at discrete microphone locations inside the cabin. Two different cabin configurations are considered. The first corresponds to a body-in-white condition, in which no acoustic treatments are present while the second configuration includes the application of sound-absorbing material on the cabin inner surfaces. The validation is performed in terms of NR, by comparing the experimental measurements with the corresponding numerical predictions at the same receiver locations. The comparison between these two configurations allows the predictive capability of the numerical model to be assessed both for the baseline vibroacoustic response of the fuselage and for the effect of acoustic absorption on the internal noise field.

6.1 Experimental Test Case Description

As part of a collaborative research program between Piaggio Aero Industries and the University of Naples Federico II, a full-scale fuselage barrel of the Piaggio P180 Avanti EVO was used as test article for an extensive experimental campaign (Fig. 6.1). The approximately 7 m long fuselage barrel was installed at the DIAS Laboratory of the University of Naples, where both modal [85] and acoustic tests were conducted.

Fig. 6.1 Piaggio P180 fuselage barrel in the DIAS Lab.

During the acoustic test, the excitation was provided by an external loudspeaker, operating over a frequency range up to 5120 Hz. A flush mounted external microphone was positioned in close proximity to the loudspeaker, facing the fuselage, in order to measure the external incident SPL. The variation in SPL between the external and internal environments was evaluated using internal microphones arranged according to two different measurement configurations, allowing the NR provided by the fuselage structure to be quantified. Considering the sensitivity limits of microphones and the maximum frequency capability of the loudspeaker, the experimental output — processed in one-third octave bands — shows centre frequencies spanning from 80 Hz to 4000 Hz, providing a consistent basis for comparison with the numerical model.

6.1.1 Test Article and Geometrical Configuration

As shown in Fig. 6.1, Piaggio P180 fuselage was stripped of the forward and main wings, as well as of the aft fuselage extending from the aft pressure bulkhead to the tail cone. The remaining fuselage barrel - made up of conventional aluminium alloy - was also partially deprived of the cabin floor, resulting in a partially bare structural configuration. The test article has an overall length of approximately 7 m and a maximum diameter of 1.95 m. The cockpit was separated from the passenger cabin by a lightweight closing panel, while an additional closing panel was installed at the aft end of the barrel. The instrumented acoustic cavity therefore corresponded to the air volume enclosed between these two closing panels. Their role in the experimental setup was primarily to delimit and seal the internal acoustic cavity, rather than to provide significant structural stiffness to the fuselage barrel. As a result, the cavity was fully sealed, ensuring that the sound pressure measured inside the cabin was primarily associated with structure-borne transmission mechanisms driven by fuselage vibrations, rather than by direct airborne transmission.

6.1.2 Experimental Boundary Conditions

Two experimental configurations were investigated, namely the body-in-white condition and the trimmed configuration with acoustic treatment. It is worth noting that both tests were conducted under the same structural and excitation conditions. In particular, the suspension system, the acoustic excitation provided by the external loudspeaker, the position of the microphones, and the measured output quantities were kept unchanged. As a result, any variation in the measured acoustic response can be directly attributed to the presence of the absorbing material. A visual comparison between the two configurations is provided in Figure 6.2, which illustrates the untreated fuselage (body-in-white) and the configuration with acoustic treatment applied to the cabin inner surfaces.

(a) White body – view 1 (b) White body – view 2 (c) White body – view 3

(d) Trimmed – view 1 (e) Trimmed – view 2 (f) Trimmed – view 3

Fig. 6.2 Comparison between the body-in-white and trimmed configurations.
Top row: untreated fuselage (body-in-white).
Bottom row: configuration with acoustic treatment (Isover PB).
The three views correspond to: view 1 — longitudinal view of the cabin ceiling extending toward the rear pressure bulkhead; view 2 — internal lateral view of the fuselage; view 3 — internal view showing the floor, sidewalls, and rear pressure bulkhead.

Body-in-White Configuration

Free–free boundary conditions for the fuselage barrel were achieved by means of a truss-like portal structure, to which the test article was suspended using bungee cords and springs. This suspension system ensures a negligible influence on the dynamic behaviour of the test article. For safety reasons, a set of saddles was also employed (see Figure 6.1).

In the baseline configuration, no acoustic absorbing materials were installed inside the cabin, and the fuselage was tested in a body-in-white condition. Under these assumptions, the internal surfaces behave as nearly reflective boundaries, and the acoustic response is primarily governed by cavity resonances and structural–acoustic coupling mechanisms.

Trimmed Configuration with Acoustic Treatment

In a second experimental configuration, the internal surfaces of the cabin were partially covered with sound-absorbing material, in order to investigate the potential for NR improvement with respect to the baseline body-in-white condition. During the experimental test campaign, the selection of the acoustic treatment was driven by the need to evaluate alternative solutions to the conventional insulation system typically adopted in aircraft cabins. In this context, glass wool panels (Isover PB) were chosen due to their favorable acoustic absorption properties, low cost, and ease of installation. This material, widely used in both civil and industrial applications, exhibits a porous fibrous structure capable of dissipating acoustic energy through viscous and thermal losses within its porous microstructure.

In the trimmed configuration the acoustic treatment is applied to the cabin side-wall surfaces. This configuration involves the installation of approximately $13\,\mathrm{m}^2$ of glass wool panels, corresponding to an additional mass of about $26\,\mathrm{kg}$. The acoustic properties of the material were experimentally characterised by means of impedance tube measurements (Kundt's tube). The resulting frequency-dependent absorption coefficient $\alpha(f)$ is reported in Fig. 6.3.

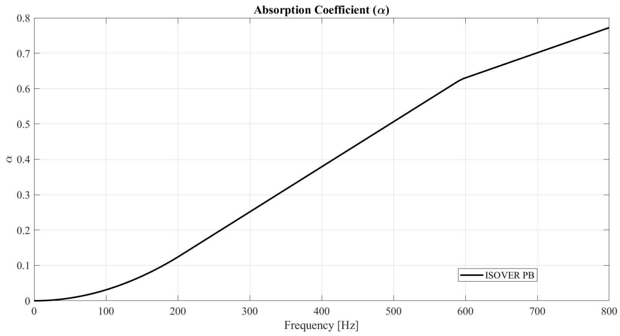

Fig. 6.3 Frequency-dependent sound absorption coefficient $\alpha(f)$ of the ISOVER PB glass wool, obtained from impedance tube measurements.

6.1.3 Acoustic Excitation and Measurement Setup

Acoustic excitation was provided by a loudspeaker emitting a white noise signal with a maximum SPL of 121 dB. The loudspeaker was positioned on the west side of the fuselage, at a distance of a few centimeters from the fuselage surface, ensuring direct exposure of the structure to the incident acoustic field (Fig. 6.4a).

A single reference microphone was positioned externally, at a distance of 250 mm from the loudspeaker. Directly facing the loudspeaker, it measured the incident SPL (see Figure 6.4b).

(a) (b)

Fig. 6.4 Experimental setup: (a) loudspeaker employed to generate the external acoustic excitation; (b) external reference microphone used to measure the incident acoustic pressure field.

The acoustic response inside the fuselage was recorded using multiple microphones arranged according to two measurement configurations (Fig. 6.5). In both configurations, the microphone layouts are annotated with identification labels assigning a unique number to each sensor. This numbering is consistently used throughout the numerical results section (Section 6.3) to refer to the corresponding measurement locations.

In the first configuration (see Fig. 6.5a), a cross-shaped array of five microphones was positioned in the fuselage section corresponding to the loudspeaker. This arrangement ensured that both the external reference and internal measurements were aligned with the incident acoustic field produced by the loudspeaker. In the second configuration (see Fig. 6.5b), four internal microphones were positioned along the longitudinal axis of the fuselage, each located 50 cm from the windows. The microphone height was set at 950 mm to approximate the ear level of a seated passenger. Microphone 5 was the closest to the loudspeaker plane, with a relative distance of 287 mm. The spacing between adjacent microphones was uniform, equal to 927 mm.

To maximize acoustic isolation, all openings created for microphone wiring were sealed with a compliant rubber material, preventing unintended sound transmission into the cabin.

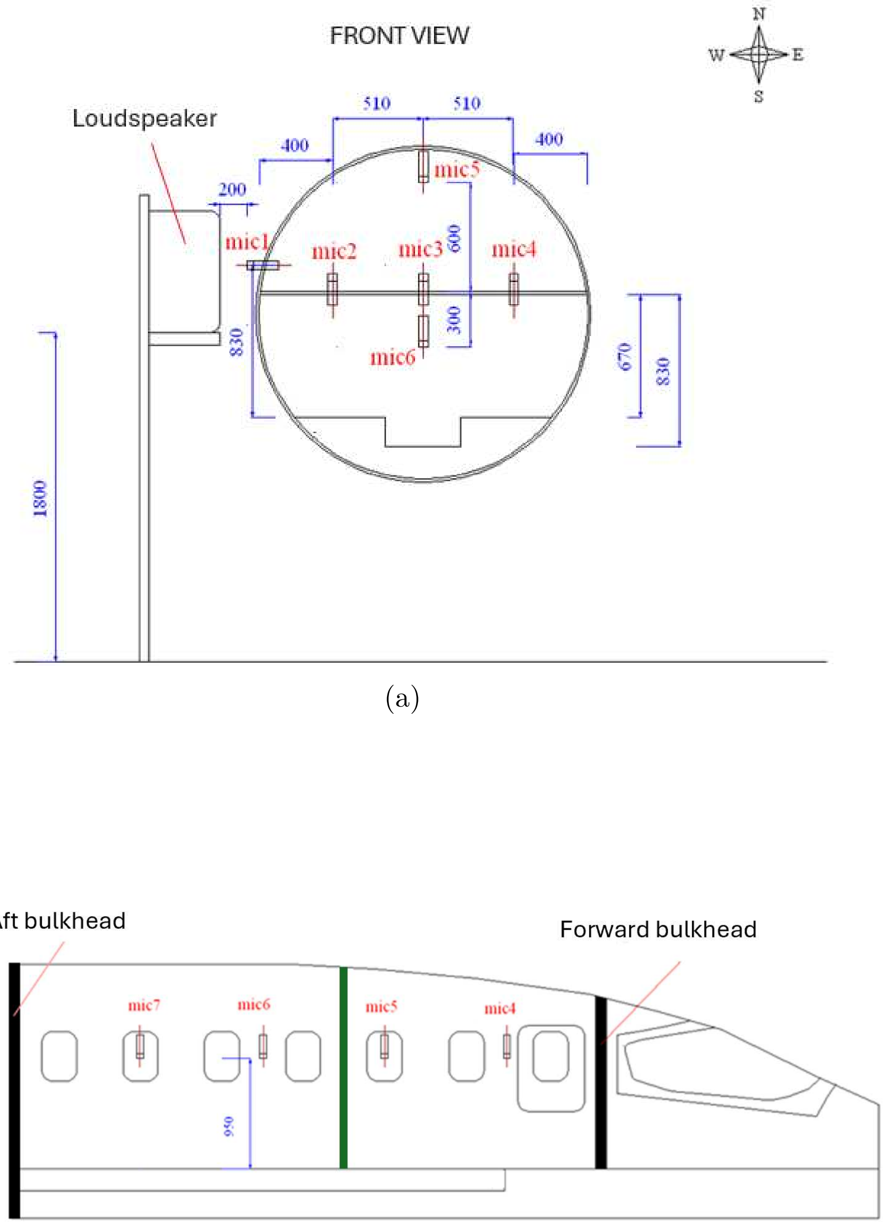

(b)

Fig. 6.5 Internal microphone configurations adopted during the acoustic test campaign: (a) cross-shaped microphone arrangement located on a diametral fuselage section directly facing the external loudspeaker; (b) longitudinal microphone configuration with sensors distributed along the cabin axis at passenger ear height; the green line represents the diametral section corresponding to configuration (a), providing a spatial reference for the position of the external acoustic excitation.

6.1.4 Experimental Output Data

The primary experimental output considered in this study is the SPL recorded by the external reference microphone. Over the frequency range of the acoustic excitation, the SPL exhibited a maximum value of approximately 100 dB, providing a reference for the incident acoustic field.

For the internal microphones, only the NR was measured, defined as the difference between the externally measured SPL and the acoustic response at each internal location:

$$\mathrm{NR}(f) = SPL_{\mathrm{external}}(f) - SPL_{\mathrm{internal}}(f), \tag{6.1}$$

NR values were available in one-third octave bands up to a maximum centre frequency of 4000 Hz.

6.2 Numerical Model Description

The numerical model described in Chapter 4, is further refined to accurately reproduce the experimental setup adopted during the acoustic test campaign presented in Section 6.1. Particular attention is devoted to the definition of boundary conditions and acoustic excitation in order to ensure consistency between numerical predictions and experimental measurements. The coupled vibroacoustic response of the Piaggio P180 passenger cabin is resolved through a frequency response analysis (SOL 111) in MSC Nastran. In accordance with the reliability range of the numerical results, the numerical–experimental comparison is performed over one-third octave bands from the centre frequency of 80 Hz. The maximum centre frequency is selected as 250 Hz.

6.2.1 Numerical Boundary Conditions

The fuselage barrel is modelled under free–free structural boundary conditions, consistently with the experimental suspension system. In the experimental setup, the forward and aft closing panels were primarily introduced to delimit and seal the internal acoustic cavity, rather than to provide significant structural stiffness to the fuselage barrel. For this reason, they are not included as structural components in the finite element model. Their effect is instead represented at the acoustic level through boundary conditions applied to the closing surfaces of the cavity.

Body-in-White Configuration

In the body-in-white numerical configuration, no acoustic absorbing materials are introduced on the cabin inner surfaces. The closing surfaces of the acoustic cavity are initially modelled as acoustically rigid boundaries, corresponding to perfectly reflecting walls. This assumption provides a baseline representation of the untreated configuration, while the influence of alternative impedance assumptions at the closing panels is investigated through the sensitivity analysis described in Section 6.2.4.

Trimmed Configuration with Acoustic Treatment

In order to reproduce the presence of acoustic treatment applied to the internal cabin surfaces (see Figure 6.2), the boundary conditions of the acoustic domain are modified to account for energy dissipation at the walls. The acoustic treatment, consisting of glass wool panels (Isover PB), is modelled using `CAABSF` elements.

From a numerical standpoint, the `CAABSF` elements are assigned to the boundary faces of the tetrahedral acoustic elements defining the cavity. Each absorber element shares the same fluid nodes as the corresponding boundary face and is characterised by a complex acoustic impedance:

$$Z(f) = Z_R(f) + iZ_I(f) \tag{6.2}$$

According to [75], the relationship between the normal-incidence absorption coefficient $\alpha(f)$ and the complex impedance is given by:

$$\alpha(f) = \frac{4\left(\frac{Z_R}{\rho c}\right)}{\left(\frac{Z_R}{\rho c}+1\right)^2 + \left(\frac{Z_I}{\rho c}\right)^2} \tag{6.3}$$

where ρ is the air density and c is the speed of sound.

Since only the experimentally measured absorption coefficient $\alpha(f)$ is available, the reconstruction of the complex impedance is not unique, as both the real and imaginary parts of $Z(f)$ would be required. In the present work, a simplified impedance reconstruction is therefore adopted by fixing the real part of the impedance to the characteristic impedance of air, namely $Z_R = \rho c$.

This assumption should be interpreted as a modelling approximation rather than as a complete description of the porous material. In more detailed equivalent-fluid models for fibrous or porous absorbers, the acoustic impedance is a complex frequency-dependent quantity governed by material parameters such as flow resistivity, porosity and tortuosity, as well as by installation conditions including thickness, backing and possible air gaps. Since these data are not available for the present configuration, they are not introduced explicitly in the model.

Under the assumption $Z_R = \rho c$, Eq. (6.3) allows the magnitude of the imaginary component $Z_I(f)$ to be derived from the measured absorption coefficient at each frequency. In the present implementation, the positive root is retained. Therefore, the impedance assigned to the `CAABSF` elements reproduces the measured normal-incidence absorption coefficient under the adopted simplifying assumption.

Although this reconstruction cannot fully represent the detailed frequency-dependent behaviour of the glass wool panels, it provides a physically consistent and computationally efficient representation of the acoustic treatment for the purposes of the present numerical–experimental comparison. A more refined characterisation would require direct impedance measurements or the adoption of equivalent-fluid material models, which are beyond the scope of this work.

6.2.2 Equivalent Acoustic Loading Definition

To reproduce the acoustic excitation produced by the external loudspeaker during the experimental campaign, an equivalent pressure boundary condition is applied to the portion of fuselage skin facing the source. The loaded area A has an extent of approximately 0.04 m^2 consistently with the estimated vibrating surface of the loudspeaker.

The excitation is represented by a spatially uniform, in-phase harmonic pressure distribution applied normal to the selected fuselage surface. This approximation is justified by the close proximity of the loudspeaker to the fuselage and by the relatively long acoustic wavelengths in the frequency range of interest, for which the incident pressure field can be considered nearly uniform over the reference loaded area. The imposed pressure amplitude is set equal to 2.8 Pa, corresponding to the peak value associated with the maximum external SPL measured during the experimental tests, equal to approximately 100 dB in RMS terms.

It should be emphasised, however, that this numerical excitation does not reproduce the complete acoustic field generated by the loudspeaker in the experimental setup. In the test, the energy transmitted into the structure depends on the actual spatial distribution of the incident field, the effective radiating area, the source–structure interaction and possible reflections in the laboratory environment. These quantities are not fully available from the experimental data.

Since the acoustic energy introduced into the numerical model cannot be assumed to match completely that introduced by the experimental source, the comparison in terms of NR is interpreted primarily in terms of frequency-dependent trends rather than as a direct band-by-band validation of absolute levels.

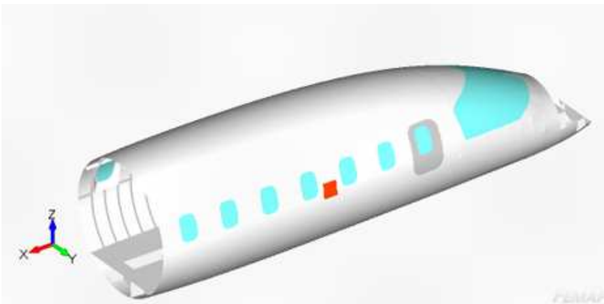

Fig. 6.6 Numerical model of the Piaggio P180 fuselage showing the pressure-loaded area (in red) corresponding to the surface facing the experimental loudspeaker.

6.2.3 Numerical Output Quantities

The acoustic pressure is evaluated at selected nodes inside the cabin whose spatial locations coincide with the positions of the internal microphones adopted during the experimental campaign. This one-to-one correspondence allows the numerical receiver locations to be consistent with the experimental measurement points.

The numerical internal SPL spectra are used to analyse the spatial distribution of the acoustic field and to identify the modal mechanisms responsible for the predicted response. However, since the experimental database provides NR values rather than independent internal SPL spectra, the validation is carried out in terms of NR. According to Eq. 6.1, the numerical NR is computed at each receiver as the difference between the reference external SPL and the internal acoustic pressure level predicted by the coupled numerical model. The reference external level is taken as 100 dB, corresponding to the RMS pressure associated with the peak pressure amplitude $p = 2.8$ Pa imposed as an equivalent acoustic load on the fuselage area A. In accordance with the experimental data, numerical results are processed in one-third octave bands. The comparison is restricted to the frequency range from 80 Hz to 250 Hz.

6.2.4 Sensitivity Analysis

A sensitivity analysis is performed to quantify the influence of the main modelling assumptions affecting the numerical–experimental comparison in terms of NR. In particular, two aspects are considered: the extension of the pressure-loaded fuselage area and the acoustic impedance assigned to the closing panels of the cavity.

Forced Area Extension

The sensitivity to the extension of the pressure-loaded area is investigated by considering three different excitation configurations. The reference case corresponds to a loaded area $A = 0.04\,\mathrm{m}^2$, consistent with the estimated effective radiating surface of the loudspeaker facing the fuselage. Two additional cases are analysed by halving and doubling this area, resulting in $A/2 = 0.02\,\mathrm{m}^2$ and $2A = 0.08\,\mathrm{m}^2$, respectively. For all cases, the pressure distribution is assumed spatially uniform and in phase over the excited surface. These three configurations define a sensitivity envelope associated with the uncertainty in the effective spatial distribution of the incident acoustic field.

Acoustic Impedance Boundary Conditions

The sensitivity to the acoustic boundary conditions at closing bulkheads is investigated by introducing different values of normal acoustic impedance at the corresponding cavity boundary. Three impedance conditions are considered:

1. a perfectly rigid boundary $(Z \to \infty)$,
2. a characteristic air impedance $Z = \rho c$ where ρ is the air density and c is the speed of sound, and
3. an intermediate impedance value $Z = 5000\ \mathrm{kg/m^2 \cdot s}$

Only the real part of the impedance is considered, i.e. a purely resistive boundary condition is assumed, neglecting any reactive (imaginary) component.

The impedance properties are introduced by means of `CAABSF` frequency-dependent fluid acoustic absorber elements. All the analyses are carried out for a fixed excitation area equal to the reference value ($A = 0.04\,\mathrm{m^2}$), in order to isolate the effect of the acoustic impedance from that of the excitation geometry.

6.3 Numerical Results and Experimental Correlation

This section presents the numerical–experimental correlation obtained for the Piaggio P180 fuselage under external acoustic excitation.

First, a representative numerical reference configuration is examined in terms of internal SPL and acoustic pressure contour plots. These results are not used for a direct SPL validation, but to interpret the modal mechanisms governing the predicted cabin response. The numerical–experimental comparison is then carried out in terms of NR, using the sensitivity envelope associated with the pressure-loaded area and the impedance sensitivity at the closing panels. Finally, the effect of acoustic treatment is analysed by comparing the body-in-white and trimmed configurations.

6.3.1 Reference Case: Internal Acoustic Pressure Response

The results presented in this section refer to a reference numerical setup in which the excitation area is fixed and equal to $0.04\,\mathrm{m}^2$, and rigid acoustic boundary conditions are assumed for the bulkheads. Results are shown at acoustic fluid nodes corresponding to the microphone positions of Configuration 1 (Figure 6.5a) and Configuration 2 (Figure 6.5b).

Configuration 1

To illustrate the effect of receiver position relative to the acoustic excitation, the numerically predicted SPL are presented for all microphones of Configuration 1. Figure 6.7a presents the SPL spectra for microphones 2, 3, and 5, which are located in proximity to the fuselage region directly exposed to the acoustic excitation. Conversely, Figure 6.7b shows the SPL spectra for microphones 4 and 6 positioned farther from the loaded area. At these locations, the predicted pressure levels are generally lower when compared to those shown in Figure 6.7a, and the resonance peaks appear globally attenuated, reflecting the spatial decay of the acoustic field inside the cavity. The response directly reflects the spatial distribution of the acoustic pressure field, resulting from the superposition of the cavity modes excited at a given forcing frequency. To facilitate the interpretation of the pressure levels predicted at the five microphone locations shown in Figure 6.7, contour plots of the acoustic pressure field are presented on a cut plane corresponding to the cross-section monitored in Configuration 1 (see Figure 6.8), at selected excitation frequencies corresponding to the observed peak values.

At an excitation frequency of 73 Hz, the first peak in the SPL response is observed. This frequency is close to the second longitudinal acoustic mode of the cavity (Fig. 4.17b), characterised by the presence of two vertical nodal planes, one of which is visible in the cut section shown in Figure 6.8a. At this resonance frequency, the pressure levels predicted at the five microphones are comparable, consistent with the axial nature of the mode, for which the pressure field is nearly uniform over the cross-section at a fixed axial position. Microphone 2 exhibits the lowest pressure level (approximately 45 dB), while

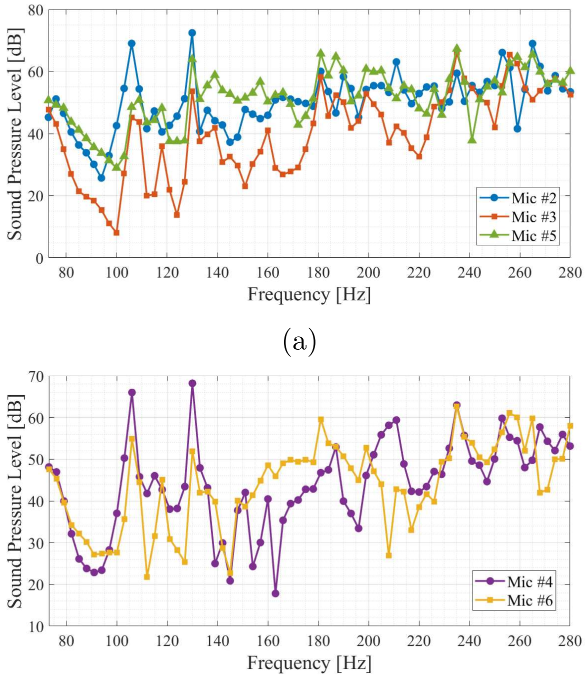

(a)

(b)

Fig. 6.7 Predicted sound pressure level at all internal microphones for Configuration 1 (see Fig. 6.5a for microphone labeling): (a) Microphones 2, 3, and 5. (b) Microphones 2 and 6.

the remaining microphones show similar SPL values, ranging from 47.6 dB (microphone 6) to 50.7 dB (microphone 5).

Within the analysed frequency range, the excitation frequencies of 106 Hz and 130 Hz, both close to acoustic natural frequencies of the cavity, are associated with pronounced pressure levels at all five microphone locations. In particular, at 130 Hz, microphones 2 and 4 attain their absolute maximum values.

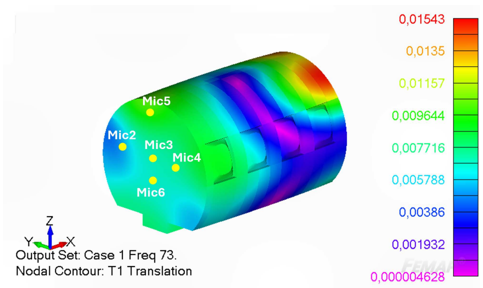

(a) 73 Hz

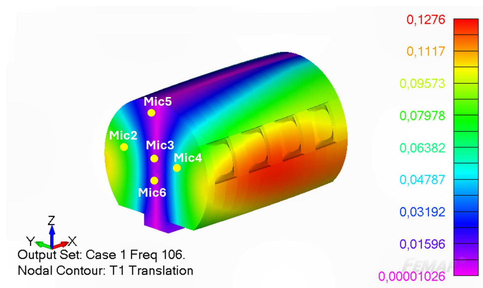

(b) 106 Hz

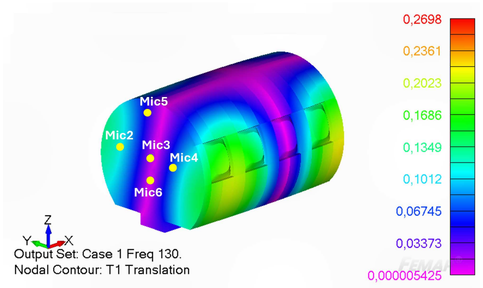

(c) 130 Hz

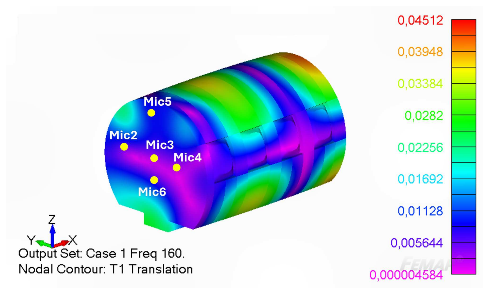

(d) 160 Hz

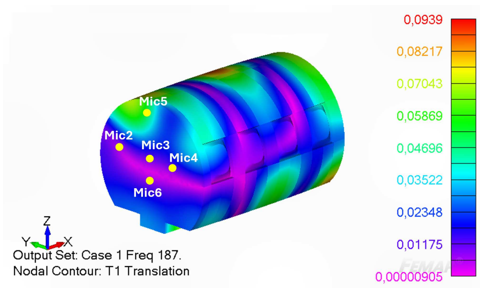

(e) 187 Hz

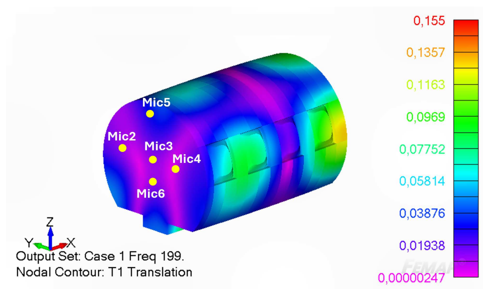

(f) 199 Hz

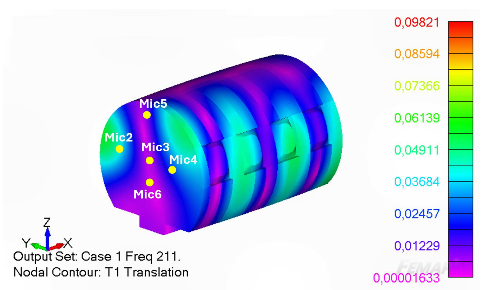

(g) 211 Hz

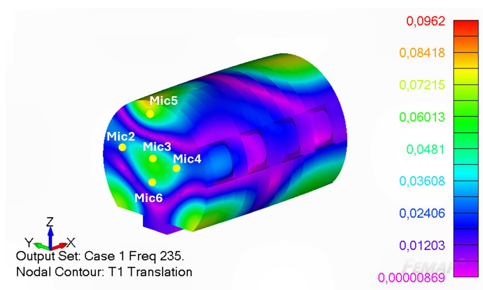

(h) 235 Hz

Fig. 6.8 Acoustic cavity pressure field distribution on a cut plane corresponding to Configuration 1 for eight excitation frequencies.

At an excitation frequency of 106 Hz, close to the first transverse acoustic natural frequency at 103.5 Hz (Fig. 4.18a), the pressure distribution is characterised by a single vertical nodal plane (XZ-oriented), as shown in Figure 6.8b. At this resonance condition, all five microphones exhibit clearly pronounced pressure peaks. In particular, microphones 2 and 4, located far from the nodal plane, experience the highest SPL among the monitored receivers, with SPL values of 69.0 dB and 66.0 dB, respectively. Conversely, microphones 6, 5, and 3, positioned closer to the nodal plane, exhibit lower pressure levels, equal to 54.8 dB, 48.6 dB, and 45.1 dB, respectively.

When the excitation frequency is increased to 130 Hz, the pressure distribution shown in Figure 6.8c closely resembles the acoustic mode shape associated with the mixed cavity mode (2,1,0), whose natural frequency is 130.2 Hz (see Figure 4.18e). At this frequency, microphone 2 experiences the highest pressure level within the analysed frequency range, reaching 72.4 dB. Microphone 4 also attains its absolute maximum, with a value of 68.2 dB. A relatively high pressure level is recorded at microphone 5, which is also located away from the nodal plane, reaching 63.9 dB. Microphones 3 and 6 exhibit relative maxima, however, being located closer to the nodal region, they show lower pressure levels compared to the other microphones, equal to 53.6 dB and 51.9 dB, respectively.

At an excitation frequency of 160 Hz, the pressure field distribution reported in Figure 6.8d is consistent with the acoustic mode (3,1,0), characterised by a natural frequency of 160.6 Hz (see Figure 4.18h). In this case, the highest pressure level is recorded at microphone 5, reaching 50.3 dB, followed by microphone 6 with 48.6 dB and microphone 2 with 45.9 dB. Microphones 3 and 4, located close to the horizontal nodal plane of the mode, exhibit lower pressure levels of 41.1 dB and 40.5 dB, respectively.

At an excitation frequency of 187 Hz, relative pressure maxima are observed at microphones 5, 3, and 4. The pressure distribution shown in Figure 6.8e reveals the presence of an XY-oriented nodal plane, together with two YZ-oriented nodal planes. This pattern is consistent with the acoustic mode associated with the cavity natural frequency at 187.3 Hz (see Figure 4.19a), which is characterised by four YZ-oriented planes, although only two of them are visible in the considered cross-section. The XY nodal plane intersects microphone 2, which therefore experiences a relative minimum, with a pressure level of 46.6 dB. Microphones 3, 4, and 6, located close to this nodal region, exhibit similar pressure levels of approximately 53 dB. In contrast, microphone 5 is located in an antinodal region of the pressure field and reaches a relative maximum of 64.7 dB.

At an excitation frequency of 199 Hz, pressure peaks are observed at microphones 5, 3 and 6. The corresponding pressure distribution, shown in Figure 6.8f, exhibits nodal structures consistent with the modal pattern associated with the cavity natural frequency at 202.3 Hz (see Figure 4.19b). Microphone 5, located away from nodal regions, records the highest pressure level, reaching 60.8 dB, followed by microphone 2 at 54.2 dB. Microphones 3 and 6 show comparable values of 52.8 dB, while microphone 4, positioned closer to a nodal region, exhibits the lowest pressure level, equal to 46.1 dB.

As the excitation frequency increases, additional SPL peaks are observed at 211 Hz and 235 Hz.

At 211 Hz, close to the cavity natural frequency at 210.7 Hz (Figure 4.19c), the pressure field exhibits a pattern consistent with this mode (Figure 6.8g). Microphones 2 and 4, located far from the vertical nodal plane, experience high pressure levels, reaching 63.1 dB and 59.3 dB, respectively. Microphone 5 shows a relative minimum (51.3 dB), while microphones 3 and 6, located closer to nodal regions, exhibit lower pressure levels of 42.2 dB and 42.8 dB, respectively.

Within the analysed frequency range, the excitation frequency of 235 Hz corresponds to the highest pressure levels observed at microphones 3, 5 and 6. The pressure distribution shown in Figure 6.8h is consistent with a radial cavity mode associated with the natural frequency at 233.6 Hz (see Figures 4.19d–4.19e). Microphones 5 and 3 are located in antinodal regions of the pressure field and reach their absolute maximum values, equal to 67.3 dB and 66.0 dB, respectively. Microphones 4 and 6 experience nearly identical values of 62.7 dB, corresponding to the absolute maximum for microphone 6. Finally, microphone 2 exhibits a well-defined relative maximum, reaching 59.4 dB.

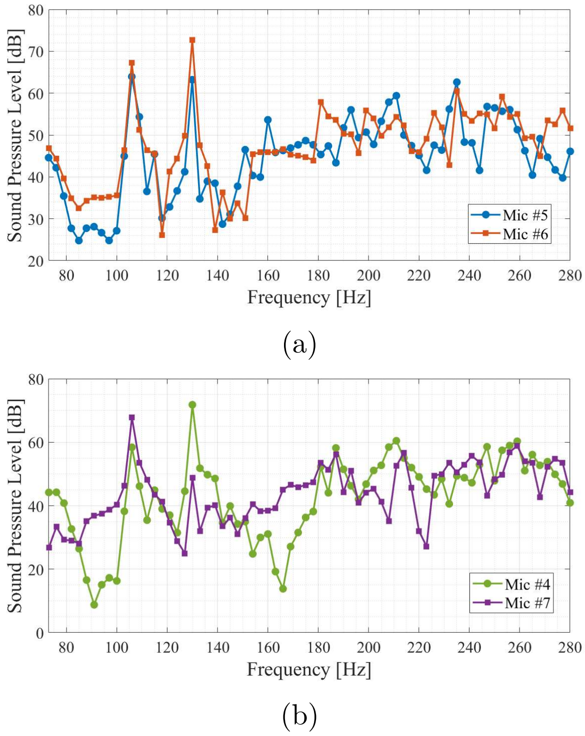

Fig. 6.9 Predicted sound pressure level at all internal microphones for Configuration 2 (see Fig. 6.5b for microphone labeling): (a) Microphones 5 and 6. (b) Microphones 4 and 7.

Configuration 2

To investigate the longitudinal distribution of the internal acoustic field, the SPL of all microphones in Configuration 2 (see Figure 6.5b) are analysed.

In the following, the numerical results are grouped based on the microphones' distance from the loudspeaker-facing plane. Microphones 5 and 6, located immediately to the right and left of the excitation plane, are considered together (Figure 6.9a), while the more distant microphones 4 and 7 are grouped and shown in Figure 6.9b. As for Configuration 1, to better understand the relationship between the SPL values at the different microphone locations shown in Figure 6.9, contour plots of the acoustic pressure distribution are reported for the cutting plane corresponding to the longitudinal section monitored in Configuration 2 (Figure 6.10), at selected excitation frequencies. Due to the longitudinal orientation of the section, these contour plots provide direct insight into the axial development of the acoustic field, enabling the identification of modal patterns associated with the excitation frequencies, including mixed modes.

As already observed for Configuration 1, an acoustic resonance is activated at an excitation frequency of 73 Hz. The pressure distribution shown in Figure 6.10a highlights the presence of two YZ-oriented nodal planes, characteristic of the second longitudinal acoustic mode at 73.3 Hz (see Figure 4.17b). Microphones 6, 5, and 4, located farther from these nodal planes, exhibit relatively higher pressure levels, equal to 46.9 dB, 44.6 dB, and 44.2 dB, respectively. In contrast, microphone 3, positioned along one of the nodal planes, experiences a pronounced relative minimum, with a pressure level of 26.8 dB.

As observed for Configuration 1, in Configuration 2 the excitation frequencies of 106 Hz and 130 Hz correspond to pronounced pressure maxima, with all four microphones reaching their absolute maximum values within the analysed frequency range.

At an excitation frequency of 106 Hz, a global acoustic resonance is observed, with the corresponding pressure distribution shown in Figure 6.10b. The plane containing the microphones under investigation is approximately parallel to the dominant nodal plane of the corresponding transverse cavity mode. Moving along the fuselage axis toward the forward bulkhead, a gradual reduction in SPL is observed. At this frequency, microphones 7 and 6 exhibit comparable pressure levels, equal to 67.8 dB and 67.2 dB, respectively, while microphone 5 reaches a slightly lower value of 63.9 dB. These represent the highest pressure levels recorded by microphone 7 and microphone 5 within the analysed frequency range. Microphone 4, located closer to a nodal region, records a lower pressure level of 58.4 dB.

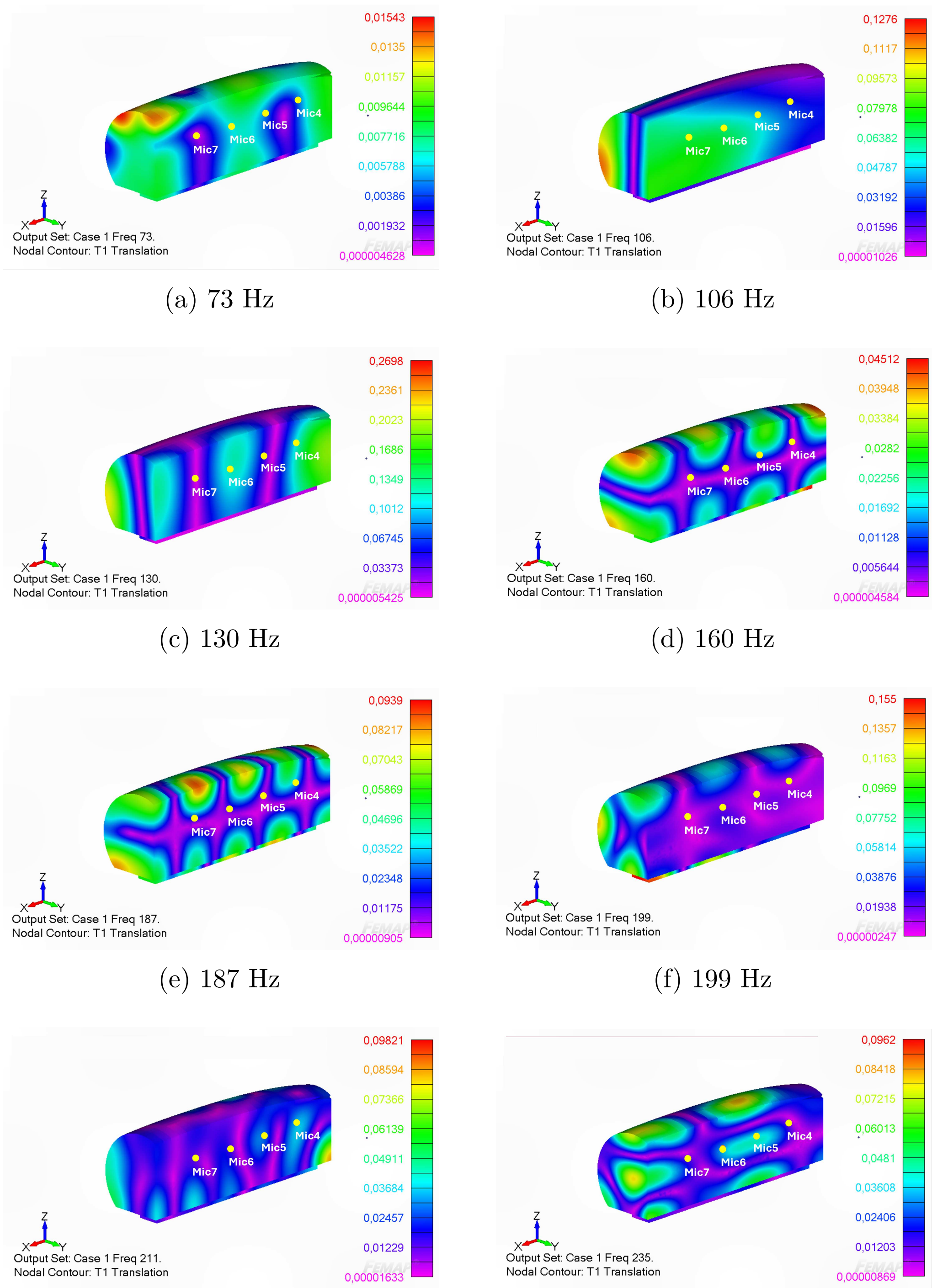

(a) 73 Hz (b) 106 Hz

(c) 130 Hz (d) 160 Hz

(e) 187 Hz (f) 199 Hz

(g) 211 Hz (h) 235 Hz

Fig. 6.10 Acoustic cavity pressure field distribution on a cut plane corresponding to Configuration 2 for eight excitation frequencies.

When the excitation frequency is increased to 130 Hz, the pressure field distribution reported in Figure 6.10c clearly reveals the presence of two YZ-oriented nodal planes, consistent with the acoustic cavity mode excited at this frequency (Fig. 4.18h). Microphone 6, located approximately midway between the two vertical nodal planes, exhibits the highest pressure level among the four microphones, reaching 72.7 dB, which corresponds to its absolute maximum within the analysed frequency range. It is followed by microphone 4, which also attains its absolute maximum at this frequency, with a value of 71.8 dB. Microphone 5 records its second-highest pressure level, equal to 63.2 dB. Finally, microphone 7, located in close proximity to a nodal plane, exhibits the lowest SPL among the four receivers, with a value of 48.8 dB.

At an excitation frequency of 160 Hz, the pressure distribution shown in Figure 6.10d clearly exhibits the modal pattern associated with the cavity natural frequency at 160.6 Hz, characterised by the presence of three nodal planes parallel to the YZ plane and one XY-oriented nodal plane. At this frequency, microphone 5 exhibits a relative maximum, reaching a pressure level of 53.6 dB, followed by microphone 6 with a value of 45.9 dB. Microphones 7 and 4, located closer to the nodal regions, record lower pressure levels of 38.5 dB and 31.1 dB, respectively.

At an excitation frequency of 187 Hz, the pressure distribution shown in Figure 6.10e corresponds to the modal pattern associated with the cavity resonance at 187.3 Hz (see Figure 4.19a). This mode can be interpreted as the successive modal shape with respect to that observed at 160 Hz, characterised by the addition of one nodal plane along the axial direction. The resulting pattern exhibits four nodal planes parallel to the YZ plane and one nodal plane parallel to the XY plane. At this frequency, microphones 4 and 7 exhibit relative maxima, reaching pressure levels of 58.2 dB and 56.3 dB, respectively. Microphone 6 records a lower value of 53.6 dB, while microphone 5, located closer to a nodal region, exhibits a relative minimum of 43.3 dB.

At an excitation frequency of 199 Hz, the pressure distribution shown in Figure 6.10f allows a clearer identification of the modal pattern associated with this frequency. In particular, two YZ-oriented nodal planes and two transversal nodal structures can be distinguished, which were only partially visible in the corresponding cross-sectional view of Configuration 1 (Figure 6.8f). At this frequency, microphones 6 and 5 exhibit relative maxima, reaching pressure levels of 55.8 dB and 50.7 dB, respectively. Microphones 4 and 7 do not exhibit distinct local maxima or minima showing SPL values of 46.8 dB and 44.2 dB, respectively.

The pressure distribution obtained at an excitation frequency of 211 Hz is shown in Figure 6.10g. This longitudinal section allows a clear identification of the modal pattern associated with the acoustic resonance at 210.7 Hz (see Figure 4.19c). At this resonance frequency, microphones 4, 5, and 6 exhibit relative maxima, reaching SPL values of 60.4 dB, 59.4 dB, and 54.4 dB, respectively. Microphone 7, located closer to one of the nodal planes, records a lower pressure level of 52.5 dB.

Figure 6.10h shows the pressure distribution at an excitation frequency of 235 Hz, corresponding to an acoustic cavity resonance characterised by the presence of one radial and one vertical nodal plane (Figs. 4.19d-4.19e). At this frequency, microphones 5 and 6 exhibit the highest pressure levels, corresponding to relative maxima of 62.6 dB and 60.5 dB, respectively. In contrast, microphones 7 and 4, located closer to nodal regions, record lower pressure levels of 50.5 dB and 49.4 dB, respectively.

Discussion

The results obtained for both measurement configurations confirm that the local acoustic response inside the cabin is primarily governed by the spatial distribution of the excited cavity modes. The evolution of the SPL cannot be interpreted solely in terms of distance from the excitation plane; rather, it must be understood in relation to the position of each receiver with respect to modal nodal and antinodal regions. The numerical model successfully reproduces these spatial pressure patterns, demonstrating its capability to capture the coupled structural–acoustic dynamics of the fuselage and to represent the underlying modal mechanisms governing the cabin sound field.

A further key aspect to be recalled in the interpretation of the results is that the occurrence of pronounced resonant responses in forced vibroacoustic systems does not depend solely on the proximity between the excitation frequency and an acoustic natural frequency. It is well established that significant resonance amplification arises only when the spatial distribution of the excitation is compatible with the modal shape of the cavity mode being activated.

In the present case, the applied acoustic loading is distributed over a fuselage panel whose normal direction is aligned with the cabin transverse axis, resulting in an excitation pattern predominantly oriented along the y-direction and so associated with an XZ-oriented excitation plane. This spatial characteristic of the load plays a crucial role in determining which cavity modes are effectively excited. This explains why, at excitation frequencies of 106 Hz and 130 Hz — close to acoustic natural frequencies associated with modes exhibiting a vertical nodal plane parallel to the XZ plane — the internal pressure response shows pronounced peaks typical of resonant behaviour, with SPL values at the microphone locations exceeding 70 dB.

6.3.2 Sensitivity Analysis: Effect of Excitation Area

This section investigates the sensitivity of the predicted NR to the extent of the excited fuselage area through a direct comparison between numerical predictions and experimental results for the body-in-white configuration. Results are presented for both measurement configurations, considering a rigid acoustic boundary condition for the bulkheads. For each configuration, the NR is evaluated by comparing three different excitation areas: the reference area A, a reduced area $A/2$ and an enlarged area $2A$. Results are reported in one-third octave bands, considering centre frequencies in the range 80–250 Hz.
For both Configurations 1 and 2, it can be readily observed that varying the extent of the excited area does not significantly modify the frequency-dependent trend of the numerical NR curves. Instead, the curves maintain an almost identical spectral shape and mainly undergo a nearly rigid vertical shift over the entire frequency range. This behaviour indicates that the excitation area primarily controls the overall amplitude of the acoustic pressure inside the cavity, while the modal pattern governing the spectral distribution of the response remains essentially unchanged. Therefore, the response corresponding to the reference case with area A, discussed in detail in Section 6.3.1, can be reliably used to interpret the frequency-dependent behaviour of the $A/2$ and $2A$ cases, since the frequencies at which the peaks occur — associated with the excitation of cavity modes — remain unchanged, while the differences are

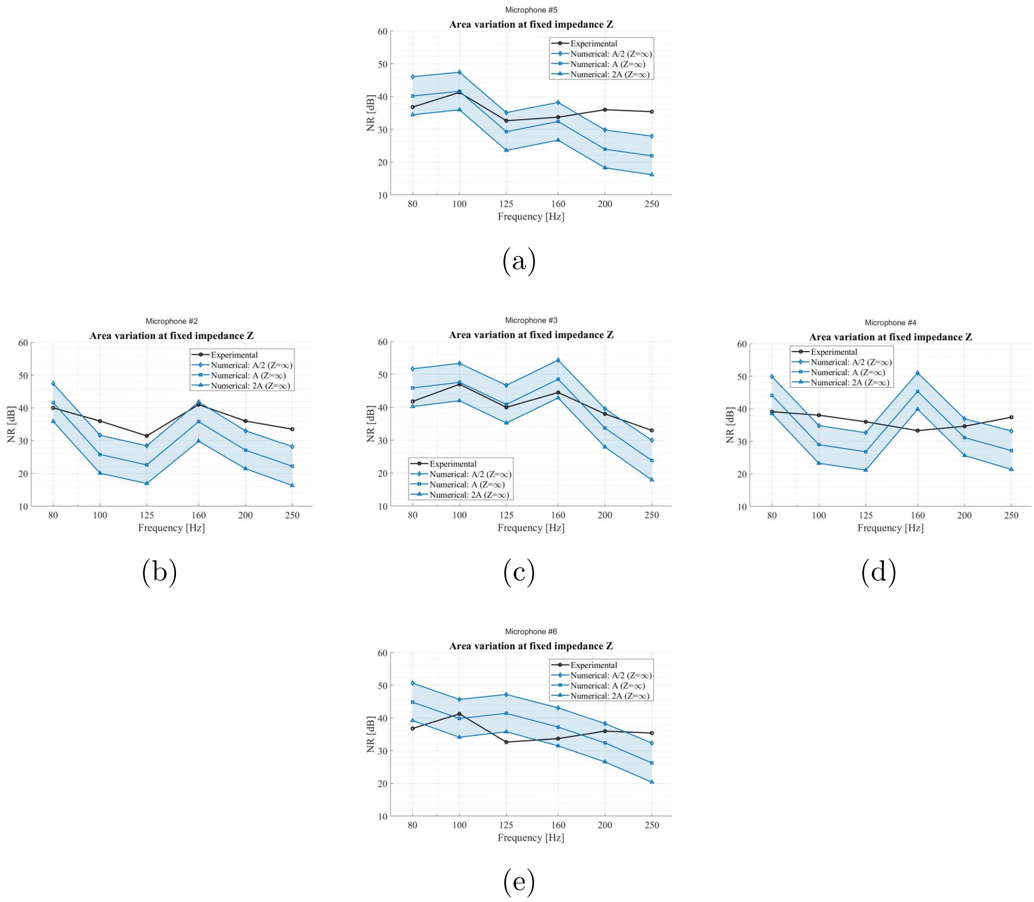

Fig. 6.11 Noise reduction for the five receiver locations of Configuration 1: (a) Microphone 5; (b) Microphone 2; (c) Microphone 3; (d) Microphone 4; (e) Microphone 6. Experimental results are shown in black, while numerical predictions are reported in blue for three different excitation area extensions: $A/2$, A and $2A$. Results presented in one-third octave bands.

essentially limited to a global level offset of the SPL.

Configuration 1

Figure 6.11 shows the predicted NR spectra at all microphone locations in Configuration 1, with the five subfigures arranged according to the cross-shaped spatial layout adopted in the experimental setup (see Figure 6.5a), together with the corresponding experimental curves.

A first qualitative assessment of the results shows good agreement with the experimental data for microphones 2, 3, and 5, namely the receivers located closest to the acoustic excitation. For these locations, the numerical model reproduces the main frequency-dependent NR trends, and the experimental values are mostly contained within the sensitivity envelope associated with the excitation-area uncertainty.

More specifically, for microphone 2 (see Figure 6.11b), the best agreement between numerical and experimental NR is obtained when the excitation area is set to $A/2$. In this case, the NR exhibits a pronounced minimum of 28.4 dB at 125 Hz. This behaviour is consistent with the high internal SPL observed in this frequency range, which includes the dominant cavity resonance around 130 Hz (see Fig. 6.7a). At a centre frequency of 100 Hz, the predicted NR is equal to 31.6 dB, again reflecting the elevated SPL associated with the nearby acoustic resonance. Conversely, at 160 Hz, the NR reaches a maximum value of 41.8 dB, corresponding to the relatively low internal pressure levels in this frequency band. This value is in very good agreement with the experimental result of approximately 41 dB. For higher centre frequencies (200 Hz and 250 Hz), both experimental and numerical NR exhibit a decreasing trend.

For microphone 3 (see Figure 6.11c), the best correspondence with the experimental NR is obtained when the excitation area is equal to the reference value A. At a centre frequency of 125 Hz, the NR exhibits a relative minimum of 40.9 dB, compared with an experimental value of approximately 40 dB, due to the increased internal SPL in this frequency range. The numerical absolute maximum of the NR is observed at a centre frequency of 160 Hz, where the internal pressure levels are generally low. The predicted value of 48.5 dB is slightly higher than the corresponding experimental value of 44.5 dB. For frequencies higher than 160 Hz, the NR decreases as the internal SPL increases, consistently with the frequency-dependent pressure response discussed in the previous section. This trend is consistent with the experimental observations.

For microphone 5 (see Figure 6.11a), the excitation area that provides the best agreement with the experimental data is again equal to the reference value A, at least up to 160 Hz. At a centre frequency of 125 Hz, the NR exhibits a relative minimum, reflecting the resonance peak associated with the cavity mode around 130 Hz. At 100 Hz and 160 Hz, the numerical and experimental results are in very close agreement, with values of 41.6 dB and 32.4 dB predicted numerically, compared to experimental values of 41.3 dB and 33.7 dB, respectively. At higher centre frequencies (200 Hz and 250 Hz), although the numerical results remain nearly constant — consistently with the experimental observations — all three sensitivity curves yield lower values than the experimental data, thus underestimating the NR.

A different behaviour is observed for microphones 4 and 6, which are located farther from the excitation region. In particular, microphone 4 is positioned diametrically opposite to the external loudspeaker, whereas microphone 6 is located closest to the cabin floor. For microphone 4 (see Figure 6.11d), the experimental NR shows a relatively smooth variation over the investigated frequency range, whereas the numerical results exhibit a much stronger frequency dependence, with pronounced minima and maxima. This indicates that, at this location, the predicted response is strongly affected by the local modal distribution of the cavity, while the corresponding experimental response appears less sensitive to these variations. Since microphone 4 is located far from the excitation region, its response is governed to a larger extent by the reflected field and by the overall cavity dynamics, making the correlation more sensitive to possible discrepancies in the modelled boundary conditions and internal geometric details.

A similar discrepancy is observed for microphone 6 (see Figure 6.11e), where the numerical model fails to accurately reproduce the overall trend of the experimental data. This behaviour can be attributed to the increased importance of the reflected acoustic field at locations farther from the source, where the response becomes strongly dependent on the boundary conditions of the cavity.

In particular, the representation of the floor plays a critical role. In the numerical model, the floor is assumed to be continuous over the entire cavity, thereby introducing additional reflections and effectively defining a closed acoustic domain. However, during the experimental campaign, the floor was not continuous: portions of the surface were absent or discontinuous, and no detailed information was available to enable a faithful reconstruction of its geometry and continuity. As a result, the acoustic cavity defined in the numerical model differs from the actual experimental configuration, particularly in the region close to the floor. This discrepancy alters the reflected acoustic field and the global modal characteristics of the cavity, leading to differences

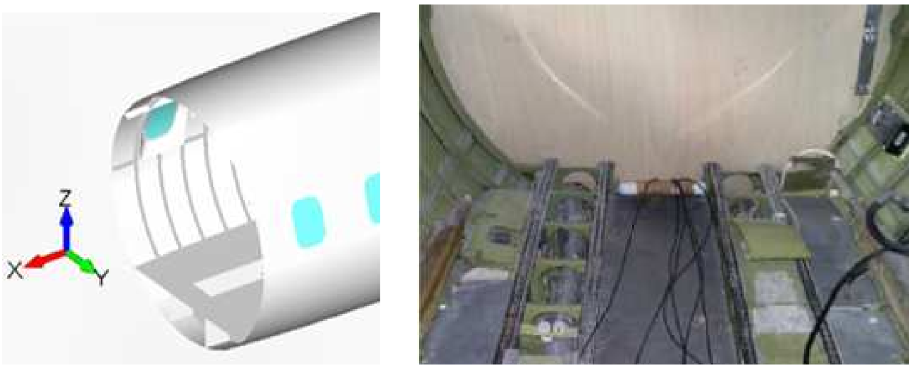

(a) (b)

Fig. 6.12 Comparison between the floor representation adopted in the numerical model and the experimental configuration: (a) continuous floor surface assumed in the numerical model; (b) discontinuous floor observed in the experimental setup. The difference affects the reflected acoustic field and the global modal characteristics of the cavity, particularly in regions close to the floor.

in the predicted NR. These differences are more pronounced at microphone locations in proximity to the floor and, more generally, at positions farther from the source, where the response is increasingly dominated by the reflected acoustic field rather than the direct contribution. A comparison between the numerical and experimental representations of the floor is shown in Figure 6.12, where the idealised continuous surface adopted in the model is contrasted with the discontinuous configuration observed in the experimental setup.

Configuration 2

For Configuration 2, the numerical NR results are reported in Figure 6.13 for all four microphone locations (see Fig. 6.5b) together with the corresponding experimental measurements. Microphone 5 is the closest receiver to the excitation plane, whereas microphone 7 is the farthest from the source. Overall, the numerical predictions show a satisfactory agreement with the experimental data for all microphone locations in terms of frequency-dependent trends. In addition, most of the experimental results fall within the sensitivity envelope defined by the numerical predictions corresponding to excitation areas between $A/2$ and $2A$.

For microphone 5 (see Figure 6.13c), the excitation area equal to A provides the closest agreement with the experimental measurements. The largest

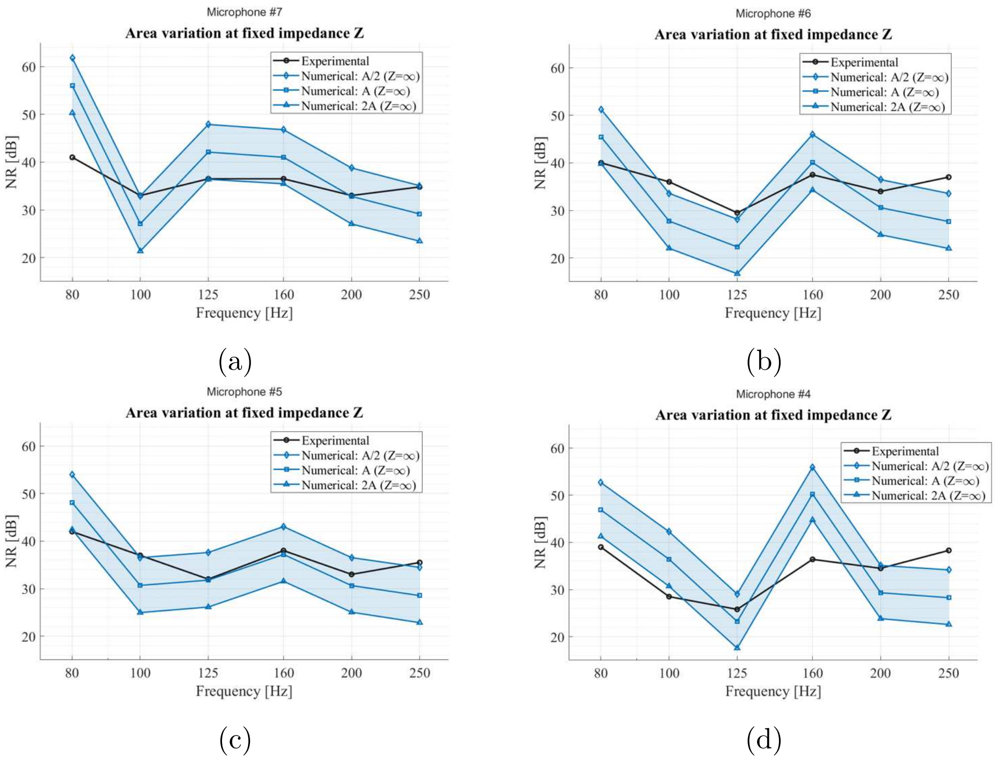

Fig. 6.13 Noise reduction for the four receiver locations of Configuration 2: (a) Microphone 7; (b) Microphone 6; (c) Microphone 5; (d) Microphone 4. Experimental results are shown in black, while numerical predictions are reported in blue for three different excitation area extensions: $A/2$, A and $2A$. Results presented in one-third octave bands.

discrepancy between numerical and experimental results is observed at the centre frequency of 100 Hz. At this frequency, the experimental curve exhibits a NR value of 37 dB, while the numerical prediction yields a NR of 31.7 dB. At the centre frequency of 125 Hz, the numerical and experimental NR curves are nearly superimposed. A similar agreement is observed at 160 Hz, where the numerical NR reaches a relative maximum of 37.2 dB, compared to 38 dB measured experimentally. This maximum is associated with lower SPL levels within this frequency band, resulting in increased NR.

For microphone 6 (see Figure 6.13b), located on the opposite side of microphone 5 along the longitudinal axis, the numerical results show very good agreement with the experimental trend, particularly when the excitation area is set to $A/2$. At 100 Hz and 125 Hz, numerical and experimental values are in close agreement (33.6 dB vs 36 dB at 100 Hz, and 28.1 dB vs 29.5 dB at 125 Hz). At 160 Hz, both numerical and experimental results exhibit a relative maximum, although here the experimental value is better approximated by the numerical prediction corresponding to area A. Between 160 Hz and 200 Hz, both curves show a decrease in NR, with experimental values falling within the sensitivity envelope defined by $A/2$ and A. At 250 Hz, a discrepancy is observed, as the experimental NR increases by approximately 3 dB, whereas the numerical prediction shows a comparable decrease.

For microphone 4 (see Figure 6.13d), the numerical results capture well the overall experimental trend, although no single excitation area can be identified as consistently representative across the entire frequency range. Both numerical and experimental curves show a decreasing behaviour from 80 Hz to 125 Hz, where a minimum is reached. At 160 Hz, both datasets exhibit a pronounced maximum, although the numerical predictions tend to overestimate the experimental values, with a difference of up to 8.4 dB for the excitation area $2A$. Between 160 Hz and 200 Hz, the numerical results show a marked decrease of 21 dB, whereas the experimental trend remains nearly constant. From 200 Hz to 250 Hz, the experimental NR increases by approximately 3.8 dB, while the numerical prediction shows a slight decrease.

For microphone 7 (see Figure 6.13a), the excitation area equal to $2A$ yields the best agreement with the experimental data, particularly at the centre frequencies of 125 Hz and 160 Hz. In agreement with the experimental trend, the numerical NR exhibits a minimum at 100 Hz and a decreasing trend between 160 Hz and 200 Hz. A discrepancy is observed in the 200–250 Hz range, where the numerical NR continues to decrease, whereas the experimental data show an increasing trend.

Quantitative indicators for numerical–experimental NR correlation

In order to complement the frequency-dependent NR comparisons discussed above, two quantitative indicators are introduced to evaluate the numerical–experimental agreement at all microphone positions: the mean absolute error and the Pearson correlation coefficient. The comparison is performed over the one-third octave bands included in the validation range.

For each microphone position and each loaded-area assumption, the mean absolute error is computed as

$$MAE_i = \frac{1}{N_f} \sum_{j=1}^{N_f} \left| NR_i^{num}(f_j) - NR_i^{exp}(f_j) \right|, \tag{6.4}$$

where i denotes the microphone position, f_j is the centre frequency of the j-th one-third octave band, and N_f is the number of frequency bands considered in the comparison.

The MAE provides a compact measure of the average absolute discrepancy between numerical and experimental NR levels. Since the objective of the comparison is mainly to assess the capability of the numerical model to reproduce the frequency-dependent NR trend, the Pearson correlation coefficient is also computed:

$$r_i = \frac{\sum_{j=1}^{N_f} \left(NR_i^{num}(f_j) - \overline{NR}_i^{num} \right) \left(NR_i^{exp}(f_j) - \overline{NR}_i^{exp} \right)}{\sqrt{\sum_{j=1}^{N_f} \left(NR_i^{num}(f_j) - \overline{NR}_i^{num} \right)^2} \sqrt{\sum_{j=1}^{N_f} \left(NR_i^{exp}(f_j) - \overline{NR}_i^{exp} \right)^2}}. \tag{6.5}$$

The Pearson coefficient provides an indicator of the agreement between the numerical and experimental frequency-dependent trends, independently of possible average offsets in the NR level. Therefore, the combined use of MAE and r allows the level mismatch and the trend agreement to be assessed separately.

Table 6.1 Quantitative indicators of numerical–experimental NR correlation for the loaded-area sensitivity analysis. Error metrics are computed over the one-third octave bands in the validation range.

Configuration	Microphone	Indicator	$A/2$	A	$2A$
1	Mic. 2	MAE [dB]	3.98	7.67	12.90
		r [-]	0.910	0.908	0.903
1	Mic. 3	MAE [dB]	6.22	3.83	6.35
		r [-]	0.952	0.952	0.952
1	Mic. 4	MAE [dB]	6.94	8.17	10.30
		r [-]	-0.157	-0.163	-0.171
1	Mic. 5	MAE [dB]	6.01	5.65	10.11
		r [-]	0.584	0.582	0.583
1	Mic. 6	MAE [dB]	7.93	5.76	6.55
		r [-]	0.123	0.121	0.120
2	Mic. 4	MAE [dB]	9.16	7.90	7.91
		r [-]	0.525	0.524	0.526
2	Mic. 5	MAE [dB]	4.61	3.80	7.57
		r [-]	0.824	0.823	0.821
2	Mic. 6	MAE [dB]	4.90	6.03	9.07
		r [-]	0.818	0.817	0.817
2	Mic. 7	MAE [dB]	8.09	6.14	6.56
		r [-]	0.952	0.952	0.952

The results reported in Table 6.1 show that no single loaded-area assumption provides the lowest error for all receivers. In Configuration 1, the best agreement is obtained with $A/2$ for microphone 2 and microphone 4, and with A for microphone 3, microphone 5 and microphone 6. In Configuration 2, the lowest errors are obtained with A for microphone 4, microphone 5 and microphone 7, while microphone 6 is better reproduced by $A/2$.

The Pearson coefficients are generally very similar for the three loaded-area assumptions at each microphone position. This indicates that changing the loaded area mainly affects the average NR level, while the frequency-dependent shape of the predicted spectra is only weakly modified.

The trend correlation is high for microphone 2 and microphone 3 in Configuration 1 and for microphone 5, microphone 6 and microphone 7 in Configuration 2. Conversely, microphone 4 in Configuration 1 shows a poor, slightly negative correlation, indicating that the experimental trend is not reproduced at this receiver. Lower correlation values are also observed for microphone 6 in Configuration 1.

Discussion

It is worth noting that increasing the excitation area while keeping the applied pressure amplitude constant leads to an increase in the acoustic energy injected into the cavity. Assuming a spatially uniform, in-phase pressure distribution over the loaded surface, this may result in an approximately proportional increase in the acoustic pressure at the receiver locations.
According to the definition of SPL:

$$\text{Sound Pressure Level [dB]} = 20 \log_{10} \left(\frac{p_{\text{rms}}}{p_{\text{ref}}} \right) \tag{6.6}$$

a doubling of the pressure amplitude yields an increase of approximately 6 dB. Conversely, halving the excitation area leads to a reduction of about 6 dB in terms of SPL. In the present case, the nearly uniform offset observed between the curves corresponding to different excitation areas is consistent with the spatially uniform, in-phase pressure distribution imposed over the loaded surface. As a consequence, the NR curves obtained for excitation areas equal to $A/2$ and $2A$ closely follow the reference curve corresponding to A, shifted upward or downward by approximately 6 dB, respectively. This behaviour is confirmed by the Pearson correlation coefficients reported in Table 6.1, which are almost identical for the three excitation areas at each microphone position. Therefore, the loaded-area variation mainly produces a vertical shift of the NR curves, while preserving their frequency-dependent trend.

In addition to this global level shift, the sensitivity analysis highlights the important role played by the spatial extent of the applied acoustic load. The results show that, while a reduced excitation area provides the best agreement with experimental NR values at receiver locations close to the loudspeaker-facing panel (e.g. microphone 2 in Configuration 1), a larger excited area is required to reproduce the experimental response at locations farther from the source. This behaviour can be explained by the different nature of the acoustic excitation in the experimental and numerical setups. In the experimental configuration, the loudspeaker generates an incident acoustic field that impinges on a relatively extended portion of the fuselage skin: additional regions of the fuselage are simultaneously excited, vibrate, and contribute to the structure-borne transmission of sound into the cabin. In contrast, the numerical model applies the acoustic pressure load only over a prescribed surface. When excitation is applied over a smaller surface area, structural regions outside the loaded zone are not directly excited and therefore do not contribute to the interior acoustic response. This simplification leads to an underestimation of the interior SPL at receiver locations located farther from the excitation region, where the reflected acoustic field becomes increasingly significant. Consequently, increasing the excitation area in the numerical model effectively compensates for the missing contribution of indirectly excited structural regions, allowing a more accurate reproduction of the experimentally observed interior pressure levels at distant microphones. In this sense, the excitation area should be interpreted as an effective modelling parameter accounting for the spatial distribution of the incident acoustic loading, while the applied pressure amplitude remains constant and equal to the reference value derived from the external microphone measurements.

Another important aspect to consider is that, while the direct field dominates the response at microphone locations close to the excitation — leading to a good agreement between numerical and experimental results — the contribution of the reflected field becomes increasingly significant for microphones located farther away. This effect is particularly evident in Configuration 1, where the discrepancies observed for microphones 4 (Fig. 6.11d) and 6 (Fig. 6.11e) can be attributed to differences between the modelled and actual boundary conditions, which affect the modal structure and so the spatial distribution of the acoustic field within the cabin. In particular, the representation of the floor in the numerical model may play a relevant role, as its assumed continuity introduces additional reflections that may not be fully representative of the experimental setup. In contrast, the improved agreement observed for Configuration 2 can be attributed to the spatial arrangement of the microphones, which are located close to the fuselage panel directly exposed to the acoustic excitation. As a result, the numerical model more accurately reproduces the experimental trends at locations dominated by the direct field. Conversely, at positions farther from the source, the increasing influence of the reflected field enhances the sensitivity of the response to modelling assumptions, particularly to discrepancies in the representation of the floor.

6.3.3 Modal truncation sensitivity analysis

A sensitivity analysis of the reduced-order model is performed to assess the influence of the retained modal basis on the coupled structural–acoustic response.

Three modal bases are considered, retaining structural and acoustic modes up to 450 Hz, 600 Hz and 900 Hz, respectively. The maximum analysis frequency is 280 Hz; however, a slightly conservative upper frequency of 300 Hz is considered for the definition of the modal truncation criteria. Therefore, the three modal bases correspond approximately to 1.5, 2 and 3 times the maximum frequency of interest, respectively. The 900 Hz basis represents the highest modal truncation frequency compatible with the adopted structural and acoustic mesh resolution and is therefore used as the reference solution.

The convergence assessment is first performed on a spatially averaged acoustic pressure response. In particular, the pressure field is averaged over a selected set of acoustic nodes located in the regions surrounding the two microphone configurations used for the validation. The selected set includes approximately 3.0×10^5 acoustic nodes, corresponding to about 10% of the total acoustic degrees of freedom.

The cumulative pressure error is computed with respect to the 900 Hz reference basis as

$$cum_{err} = \frac{\sum_{j=1}^{N_f} \left(\overline{p}^{BM}(f_j) - \overline{p}^{ref}(f_j)\right)^2}{\sum_{j=1}^{N_f} \left(\overline{p}^{ref}(f_j)\right)^2} \cdot 100, \tag{6.7}$$

where $\overline{p}^{BM}(f_j)$ is the spatially averaged acoustic pressure obtained at the frequency f_j with a given modal basis, $\overline{p}^{ref}(f_j)$ is the corresponding pressure obtained with the 900 Hz reference basis, and N_f is the number of narrow-band frequency points considered in the analysis.

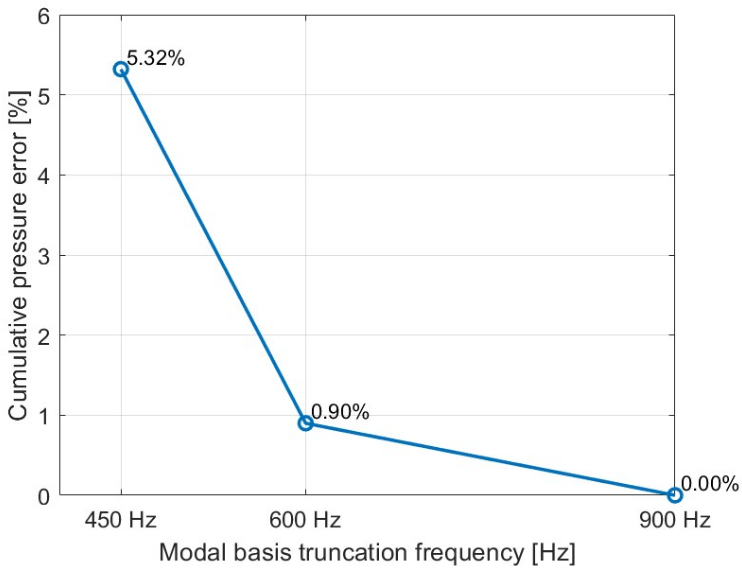

Fig. 6.14 Modal truncation sensitivity analysis based on the cumulative pressure error computed from the spatially averaged acoustic pressure over the selected cavity region. The 900 Hz modal basis is used as reference.

The cumulative pressure error obtained for the three modal bases is reported in Figure 6.14. The 900 Hz case has zero error because it is used as the reference solution. The error decreases from 5.32% for the 450 Hz basis to 0.90% for the 600 Hz basis. Therefore, extending the modal basis from 450 Hz to 600 Hz produces a clear reduction of the truncation error, whereas the further extension from 600 Hz to 900 Hz leads to only minor changes in the spatially averaged acoustic response.

In addition, the convergence behaviour is also checked at the microphone locations used in the numerical–experimental validation. The microphone-by-microphone cumulative errors are reported in Table 6.2. The 450 Hz basis shows larger receiver-dependent discrepancies, with higher errors mainly observed for microphones of Configuration 2. Conversely, the 600 Hz basis provides a clear reduction of the error at all microphone positions, with values always below 3%. This confirms that the improvement observed in the spatially averaged pressure response is also reflected at the receiver locations used for the numerical–experimental validation.

The modal truncation sensitivity analysis supports the use of a modal basis retained up to twice the maximum excitation frequency, corresponding to 600 Hz in the present simulations.

Table 6.2 Microphone-by-microphone cumulative pressure error for the modal truncation sensitivity analysis. The 900 Hz modal basis is used as reference.

Microphone	450 Hz	600 Hz	900 Hz
C1 Mic. 2	11.15	1.69	0.00
C1 Mic. 3	5.63	2.95	0.00
C1 Mic. 4	10.59	2.19	0.00
C1 Mic. 5	5.03	1.89	0.00
C1 Mic. 6	6.34	2.61	0.00
C2 Mic. 4	21.67	2.66	0.00
C2 Mic. 5	28.41	1.65	0.00
C2 Mic. 6	24.41	2.81	0.00
C2 Mic. 7	28.68	1.25	0.00

6.3.4 Sensitivity Analysis: Effect of Acoustic Impedance

This section examines the influence of different acoustic impedance values assigned to the closing bulkheads through a direct comparison between numerical predictions and experimental results for the body-in-white configuration. Three boundary conditions are considered: a perfectly rigid surface ($Z \to \infty$), a characteristic air impedance $Z = \rho c$, and an intermediate impedance value $Z = 5000\,\mathrm{kg/m^2 \cdot s}$. All results presented in this section are computed by fixing the excitation area to the reference value $A = 0.04\,\mathrm{m}^2$, in order to isolate the effect of the acoustic boundary conditions from that of the excitation area extent.

Configuration 1

Figure 6.15 shows the predicted NR spectra for microphones 2 and 3 of Configuration 1 under the three considered acoustic impedance conditions, together with the experimental NR curve measured for the body-in-white configuration.

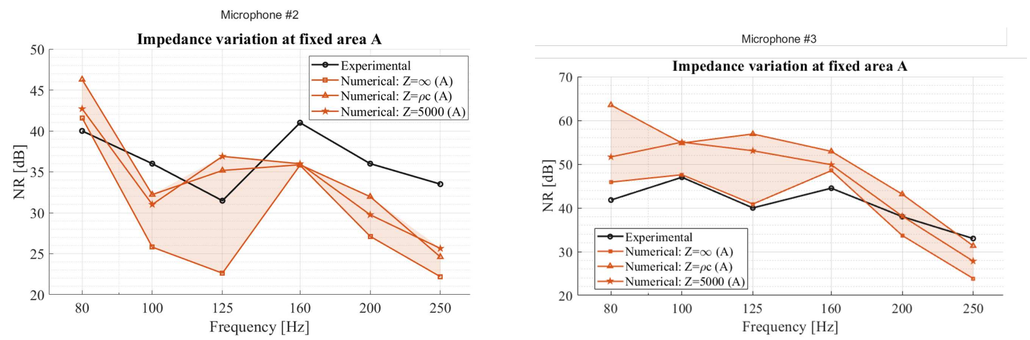

(a) (b)

Fig. 6.15 Noise reduction for two representative receiver locations of Configuration 1: (a) Microphone 2; (b) Microphone 3. Experimental results are shown in black, while numerical predictions are reported in red for three different impedance values: ($Z \to \infty$), $Z = \rho c$ and $Z = 5000$. Results presented in one-third octave bands.

For microphone 2 (Figure 6.15a), the NR predicted for all impedance values exhibits a decreasing trend when moving from the centre frequency of 80 Hz to 100 Hz. A similar behaviour is observed in the experimental data, although the reduction is less pronounced. At 125 Hz, different trends emerge depending on the impedance condition. For $Z = \rho c$ and $Z = 5000$, a local maximum in NR is observed, whereas a local minimum is predicted for the perfectly rigid condition ($Z \to \infty$), in agreement with the experimental trend. From 125 Hz to 160 Hz, both the experimental curve and the numerical prediction corresponding to the rigid boundary condition show a significant increase, reaching a maximum at 160 Hz. In particular, the increase is approximately 10 dB for the experimental data and about 13.5 dB for the perfectly rigid condition. In contrast, the curves corresponding to $Z = \rho c$ and $Z = 5000$ exhibit only minor variations, on the order of 1 dB. Finally, a decreasing trend is observed between 160 Hz and 250 Hz for both the experimental and numerical results across all impedance conditions.

As shown in Figure 6.15b, the boundary condition that best approximates the experimental results for microphone 3 is the rigid case ($Z \to \infty$). For the selected excitation area, the numerical predictions corresponding to the rigid boundary condition closely match the experimental values. In particular, both curves exhibit a local maximum at 100 Hz and a local minimum at 125 Hz, with nearly coincident values at these frequencies. Both the experimental data and the rigid-boundary prediction then show a pronounced maximum at 160 Hz, although the numerical result slightly overestimates the NR by approximately 4 dB. From 160 Hz to 250 Hz, all numerical curves exhibit a decreasing trend, in agreement with the experimental data. In contrast, the numerical curves corresponding to $Z = \rho c$ and $Z = 5000$ show a trend that differs from the experimental behaviour. They intersect at 100 Hz and then evolve almost in parallel up to 250 Hz showing a decreasing trend, with the $Z = \rho c$ case consistently yielding higher NR values than the $Z = 5000$ condition, as expected.

Predicting the variation of NR as a function of the acoustic impedance assigned to the closing bulkheads is inherently complex and cannot be reduced to a simple quantitative relationship. Although increasing impedance tends, in principle, to make the cavity boundaries more reflective, and therefore to increase the acoustic pressure levels inside the cabin, the resulting interior response is governed by more complex mechanisms. These include wave reflection, interference between incident and reflected components, partial cancellation or reinforcement of the acoustic field, and the frequency-dependent modification of nodal and antinodal regions within the cavity. As a consequence, the effect of impedance on NR cannot be interpreted through a simple monotonic relationship. For this reason, a qualitative analysis of the corresponding pressure field distributions is more informative than a purely quantitative comparison of NR values. Figure 6.16 shows the acoustic pressure field on the cut plane corresponding to the microphone plane of Configuration 1, for the three impedance conditions considered and for three representative excitation frequencies.

Although the present cavity geometry is far from being perfectly cylindrical, the forced response obtained under rigid-wall conditions still shows recognizable modal features, with well-defined nodal planes and pressure lobes. In particular, the third column of Figure 6.16, corresponding to $Z \to \infty$, displays pressure patterns associated with three excitation frequencies close to acoustic natural

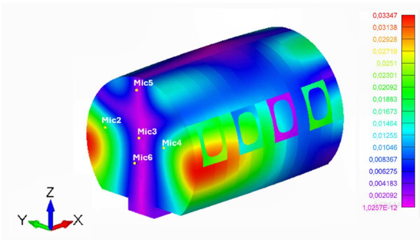

(a) 106 Hz, $Z = \rho c$

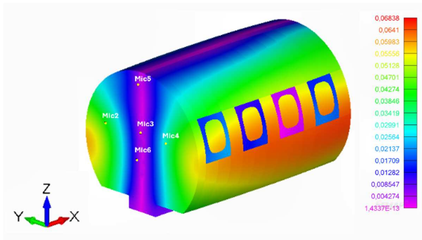

(b) 106 Hz, $Z = 5000$

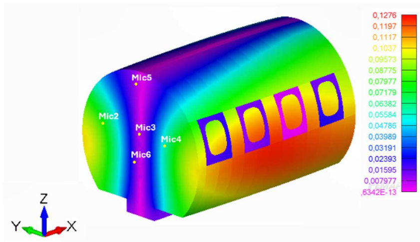

(c) 106 Hz, $Z \to \infty$

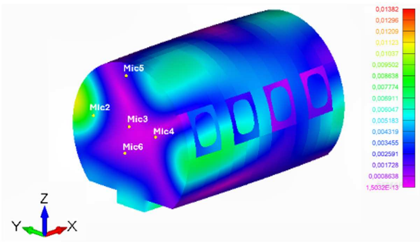

(d) 130 Hz, $Z = \rho c$

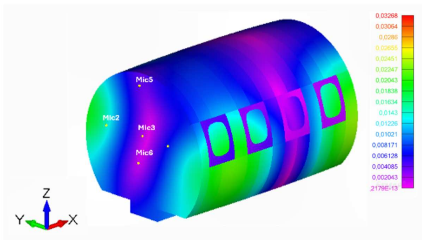

(e) 130 Hz, $Z = 5000$

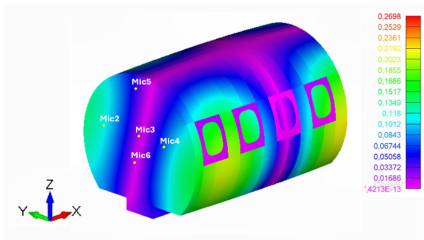

(f) 130 Hz, $Z \to \infty$

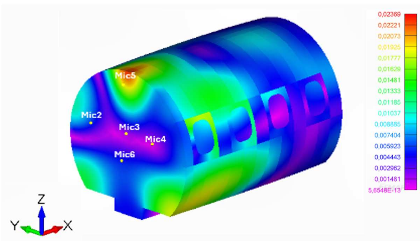

(g) 160 Hz, $Z = \rho c$

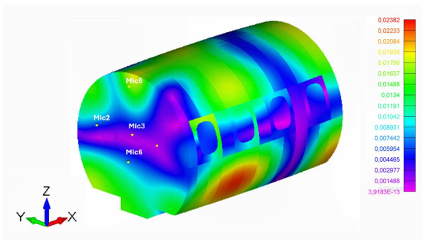

(h) 160 Hz, $Z = 5000$

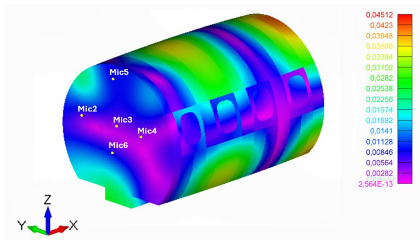

(i) 160 Hz, $Z \to \infty$

Fig. 6.16 Acoustic pressure field distribution on the cut plane corresponding to Configuration 1 for different acoustic impedance boundary conditions applied to the closing bulkheads. Rows correspond to excitation frequencies (106 Hz, 130 Hz, and 160 Hz), while columns correspond to increasing impedance values ($Z = \rho c$, $Z = 5000\,\mathrm{kg/(m^2 \cdot s)}$, and $Z \to \infty$).

frequencies of the cavity under rigid-wall boundary conditions, and therefore closely resembling the corresponding modal distributions.

The main purpose of Figure 6.16 is to assess, from a qualitative standpoint, how far the pressure distributions predicted for $Z = \rho c$ and $Z = 5000\,\mathrm{kg/(m^2 \cdot s)}$ deviate from the rigid-wall reference case.

At 106 Hz, the pressure distribution obtained for $Z = \rho c$ (Figure 6.16a) differs from that corresponding to the rigid-wall condition (Figure 6.16c). In particular, an additional nodal zone can be observed in the upper part of the section, approximately orthogonal to the dominant nodal plane characterizing the rigid case. For $Z = 5000\,\mathrm{kg/(m^2 \cdot s)}$ (Figure 6.16b), this feature is no longer evident, and the pressure distribution becomes significantly closer to that obtained for $Z \to \infty$.

A similar behaviour is observed at 130 Hz. For $Z = \rho c$, the region associated with low pressure levels is much more extended, so that it can no longer be interpreted as a well-defined nodal plane, but rather as a broad nodal area. The slightly inclined nodal plane that characterizes the rigid-wall case (Figure 6.16f) starts to become recognizable already for $Z = 5000\,\mathrm{kg/(m^2 \cdot s)}$ (Figure 6.16e), although less sharply defined.

At 160 Hz, the rigid-wall condition shows that the investigated section lies close to the YZ-oriented nodal plane associated with the acoustic mode excited in this frequency range. In this case, the pressure distribution obtained for $Z = \rho c$ (Figure 6.16g) already exhibits the onset of a nodal plane consistent with the pattern observed for $Z \to \infty$. The result for $Z = 5000\,\mathrm{kg/(m^2 \cdot s)}$ (Figure 6.16h) appears even closer to the rigid-boundary reference.

For all three analysed frequencies, although the spatial pressure distribution becomes progressively more similar to the rigid-wall case as the impedance increases, the variation of the absolute pressure levels with Z is not monotonic. At some frequencies, such as 106 Hz, a significant increase in pressure amplitude — of approximately one order of magnitude — is observed with increasing impedance. In contrast, at 160 Hz, the maximum pressure levels remain nearly unchanged when passing from $Z = \rho c$ to $Z = 5000$, and only slightly increase for the rigid-wall condition ($Z \to \infty$). These observations indicate that the effect of acoustic impedance on the interior pressure field cannot be interpreted solely in terms of increased reflectivity. Rather, it results from a complex interplay between wave reflection, modal distribution, and interference effects, leading to local amplification or cancellation of the acoustic field within the cavity. Overall, increasing the acoustic impedance tends to drive the spatial pressure distribution toward the rigid-wall modal patterns, while the corresponding pressure amplitudes remain strongly dependent on frequency and modal characteristics.

Configuration 2

Figure 6.17 shows the predicted NR spectra for microphones 5 and 7 of Configuration 2 under the three considered acoustic impedance conditions, together with the experimental NR curve measured for the body-in-white configuration.

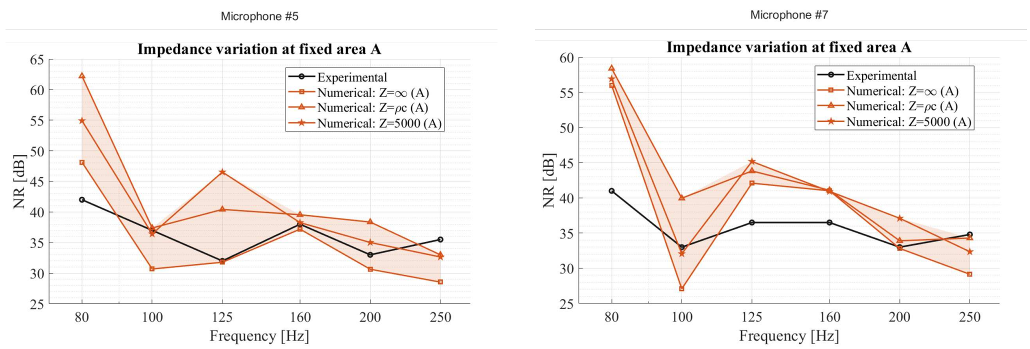

(a) (b)

Fig. 6.17 Noise reduction for two representative receiver locations of Configuration 2: (a) Microphone 5; (b) Microphone 7. Experimental results are shown in black, while numerical predictions are reported in red for three different Impedance values: $(Z \to \infty)$, $Z = \rho c$ and $Z = 5000$. Results presented in one-third octave bands.

For microphone 5 (Figure 6.17a), the NR decreases from 80 Hz to 100 Hz for all three impedance values, in agreement with the experimental trend, although the experimental curve exhibits a significantly less pronounced reduction. At the 125 Hz, the numerical curves corresponding to $Z = \rho c$ and $Z = 5000$ show a local maximum, while the rigid condition predicts a local minimum, consistently with the experimental observations. In particular, the numerical result for the rigid case is nearly coincident with the experimental value for the selected reference excitation area A. At 160 Hz, the curve corresponding to $Z = 5000$ coincides with the experimental value of approximately 38 dB. The numerical predictions for $Z \to \infty$ and $Z = \rho c$ are also close to the experimental data, showing differences of about -0.8 dB and +1.5 dB, respectively. From 160 Hz to 250 Hz, all numerical curves exhibit a decreasing trend, although less pronounced than that observed between 80 Hz and 100 Hz. The experimental curve, however, shows a local discontinuity at 200 Hz, where a relative minimum is reached.

For microphone 7 (Figure 6.17b), all three numerical curves exhibit a very similar trend, characterised by a pronounced minimum at 100 Hz and a maximum at 125 Hz, in agreement with the experimental data. In particular, all impedance cases show a decreasing trend between 80 Hz and 100 Hz, consistent with the experimental observations, although the reduction is more pronounced in the numerical predictions. Between 100 Hz and 125 Hz, both numerical and experimental curves increase. From 125 Hz to 160 Hz, the numerical curves exhibit a decreasing trend, while the experimental NR remains approximately constant. At 160 Hz, all numerical curves collapse to a value of about 40 dB, compared to an experimental value of approximately 36.5 dB. In this frequency range, the numerical results tend to overestimate the experimental data, with a maximum difference of about 5 dB at 125 Hz for the rigid boundary condition. At 200 Hz, both the experimental curve and the $Z = \rho c$ numerical curve exhibit a local minimum, whereas the other impedance cases show a nearly linear decrease from 160 Hz to 250 Hz.

Similarly to Configuration 1, Figure 6.18 provides a qualitative comparison of the acoustic pressure field at three excitation frequencies for the three considered impedance conditions, evaluated on the longitudinal plane corresponding to the microphone locations of Configuration 2.

At 106 Hz, the pressure distribution obtained for $Z = \rho c$ (Figure 6.18a) differs significantly from the rigid-wall case. In particular, the pressure field exhibits a quasi-radial distribution, with higher pressure levels concentrated in the central region of the section and decreasing toward the boundaries. In contrast, for $Z = 5000$ (Figure 6.18b), the pressure distribution becomes more consistent with that of the rigid-wall condition, showing a more uniform field divided into two main regions approximately separated in correspondence with microphones 5 and 6.

At 130 Hz, the pressure distribution for $Z = \rho c$ (Figure 6.18d) does not exhibit clearly defined vertical nodal planes, which are instead well visible in the rigid-wall case (Figure 6.18f) and already recognizable for $Z = 5000$ (Figure 6.18e). In the $Z = \rho c$ case, the nodal features appear less defined and tend to assume a more horizontal orientation.

At 160 Hz, the pressure distribution obtained for $Z = \rho c$ (Figure 6.18g) already exhibits the XY-oriented nodal plane clearly visible in the rigid-wall case (Figure 6.18i). In addition, the multiple vertical nodal planes characteristic of the rigid condition begin to appear, although not yet sharply defined. For $Z = 5000$ (Figure 6.18h), the pressure field becomes very close to the reference rigid-wall distribution, with well-defined lobes, except in the region closer to the aft bulkhead, where slight discrepancies persist.

Overall, the results indicate that increasing the acoustic impedance progressively drives the pressure field toward the rigid-wall modal behaviour, with a gradual recovery of well-defined nodal structures. As already observed for Configuration 1, the associated pressure amplitudes exhibit a strongly frequency-dependent response, with no monotonic variation with increasing impedance.

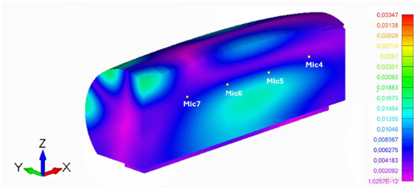

(a) 106 Hz, $Z = \rho c$

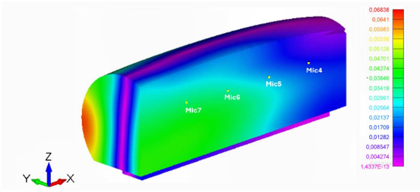

(b) 106 Hz, $Z = 5000$

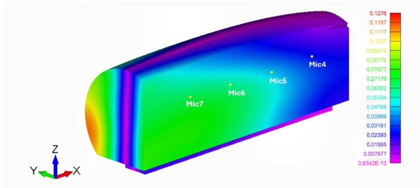

(c) 106 Hz, $Z \to \infty$

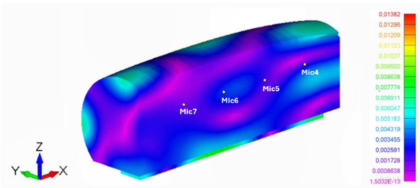

(d) 130 Hz, $Z = \rho c$

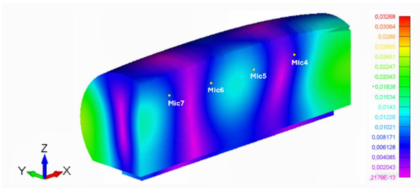

(e) 130 Hz, $Z = 5000$

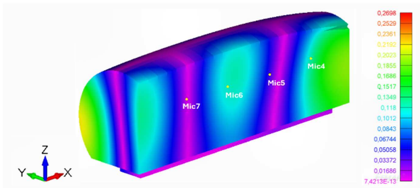

(f) 106 Hz, $Z \to \infty$

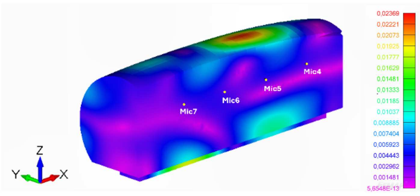

(g) 160 Hz, $Z = \rho c$

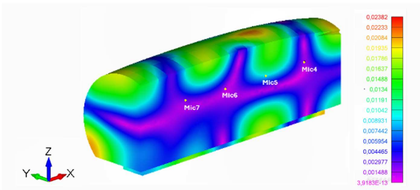

(h) 160 Hz, $Z = 5000$

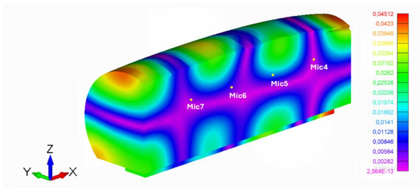

(i) 160 Hz, $Z \to \infty$

Fig. 6.18 Acoustic pressure field distribution on the cut plane corresponding to Configuration 2 for different acoustic impedance boundary conditions applied to the closing bulkheads. Rows correspond to excitation frequencies (106 Hz, 130 Hz, and 160 Hz), while columns correspond to increasing impedance values ($Z = \rho c$, $Z = 5000\,\mathrm{kg/(m^2 \cdot s)}$, and $Z \to \infty$).

Quantitative indicators for impedance sensitivity

As for the loaded-area sensitivity analysis, two quantitative indicators are introduced to evaluate the impedance sensitivity at all microphone positions: the mean absolute error MAE and the Pearson correlation coefficient r.

The indicators are evaluated for the three impedance assumptions assigned to the cavity closing panels: $Z = \rho c$, $Z = 5000$ kg/(m^{2}s), and $Z \to \infty$. The MAE quantifies the average discrepancy in absolute NR level, whereas r indicates whether the frequency-dependent experimental trend is reproduced.

Table 6.3 Quantitative indicators of numerical–experimental NR correlation for the impedance sensitivity analysis. Error metrics are computed over the one-third octave bands in the validation range.

Configuration	Microphone	Indicator	$Z = \rho c$	$Z = 5000$	$Z \to \infty$
1	Mic. 2	MAE [dB]	5.30	5.37	7.67
		r [-]	0.586	0.479	0.908
1	Mic. 3	MAE [dB]	10.28	6.93	3.83
		r [-]	0.754	0.886	0.952
1	Mic. 4	MAE [dB]	7.18	6.58	8.17
		r [-]	0.048	-0.222	-0.163
1	Mic. 5	MAE [dB]	4.66	5.28	5.65
		r [-]	0.514	0.552	0.582
1	Mic. 6	MAE [dB]	8.42	6.63	5.76
		r [-]	0.224	0.094	0.121
2	Mic. 4	MAE [dB]	11.72	9.12	7.90
		r [-]	-0.059	0.128	0.524
2	Mic. 5	MAE [dB]	6.40	5.53	3.80
		r [-]	0.714	0.482	0.823
2	Mic. 6	MAE [dB]	6.60	5.83	6.03
		r [-]	0.424	0.376	0.817
2	Mic. 7	MAE [dB]	6.28	6.08	6.14
		r [-]	0.910	0.928	0.952

The results show that the rigid-wall condition generally provides the highest Pearson correlation coefficients, especially for Configuration 2. This indicates that the frequency-dependent NR trend is better reproduced when the closing panels are modelled as nearly reflecting boundaries.

The MAE values show a less uniform behaviour: in some microphone positions, finite impedance values lead to slightly lower absolute errors. This indicates that the impedance boundary condition affects both the average NR level and the spectral trend, with a receiver-dependent influence. Overall, the impedance sensitivity analysis supports the use of the rigid-wall condition as the reference assumption for the closing panels, while confirming that local discrepancies remain dependent on the microphone position.

Discussion

The NR curves (Figures 6.15 and 6.17) indicate that the numerical predictions obtained with rigid acoustic boundary conditions ($Z \to \infty$) provide, overall, the closest agreement with the experimental data when compared to the cases $Z = \rho c$ and $Z = 5000\,\mathrm{kg/(m^2 \cdot s)}$, as already observed for representative microphones in both configurations. Consistently across all microphones, the rigid boundary condition generally yields lower NR values, reflecting higher internal pressure levels due to the fully reflective nature of the cavity walls.

However, the comparison between different impedance conditions does not reveal any monotonic or systematic relationship between NR and acoustic impedance, as the corresponding NR curves exhibit multiple intersections across the analysed frequency range. This behaviour is a direct consequence of the role of boundary impedance in controlling both the reflection of acoustic waves and the modal characteristics of the cavity. In particular, changing the acoustic boundary conditions modifies not only the level of reflection at the walls, but also the natural frequencies and associated modal shapes of the cavity. As a result, the forced response differs from that obtained under rigid-wall conditions, even when the excitation remains unchanged. Furthermore, the acoustic response at a given location is governed by the spatial distribution of the pressure field, which arises from the superposition of cavity modes excited at each frequency. Interference phenomena between incident and reflected waves therefore lead to local amplification or cancellation effects, making the prediction of the acoustic response highly sensitive to both frequency and receiver position.

The qualitative analysis of the pressure contour plots (Figs. 6.16-6.18) further confirms that, for a given excitation frequency, the spatial distribution of the pressure field differs between low-impedance ($Z = \rho c$) and rigid-wall conditions. As the impedance increases (e.g. $Z = 5000$), the pressure field progressively approaches the rigid-wall modal patterns. Importantly, the discrepancy between these two limiting cases tends to decrease with increasing excitation frequency. This behaviour is consistent with the typical response of acoustic systems, in which the influence of boundary conditions becomes less dominant at higher frequencies. As the wavelength decreases and the modal density increases, the acoustic field results from the superposition of a larger number of modes, reducing the sensitivity of the global response to the specific boundary conditions.

Overall, although the rigid boundary condition generally leads to lower NR values, followed by the intermediate and characteristic impedance cases, the response remains strongly frequency-dependent and non-monotonic. This is clearly illustrated, for instance, at 160 Hz, where all impedance conditions yield very similar NR values despite the substantially different boundary assumptions.

6.3.5 Trimmed Configuration: Effect of Acoustic Treatment

In this section, the effect of the application of acoustic absorbing material (glass wool Isover PB) on the internal acoustic response is evaluated at the same microphone locations considered in the previous sections. As previously described, the absorbing material is installed on the internal sidewalls of the fuselage, filling the cavities between adjacent structural frames. In the numerical model, this configuration is represented by means of `CAABSF` elements, i.e. frequency-dependent acoustic absorber elements applied on the boundary of the acoustic cavity. The resulting acoustic pressure field is analysed and compared with the reference case characterised by perfectly reflecting walls (Section 6.3.1), in order to quantify the effect of the acoustic treatment in terms of pressure reduction, while maintaining the same excitation area equal to A. In addition, the NR is evaluated and compared with the baseline configuration, and further assessed against the corresponding experimental measurements, thus enabling a direct numerical–experimental comparison of the model response in the presence of acoustic treatment.

Configuration 1

Figure 6.19 reports the numerically predicted SPL at the five microphones of Configuration 1 in the presence of acoustic treatment. In particular, Figure 6.19a refers to microphones 2, 3, and 5, which are located closer to the loudspeaker, while Figure 6.19b shows the results for microphones 4 and 6, positioned farther away.

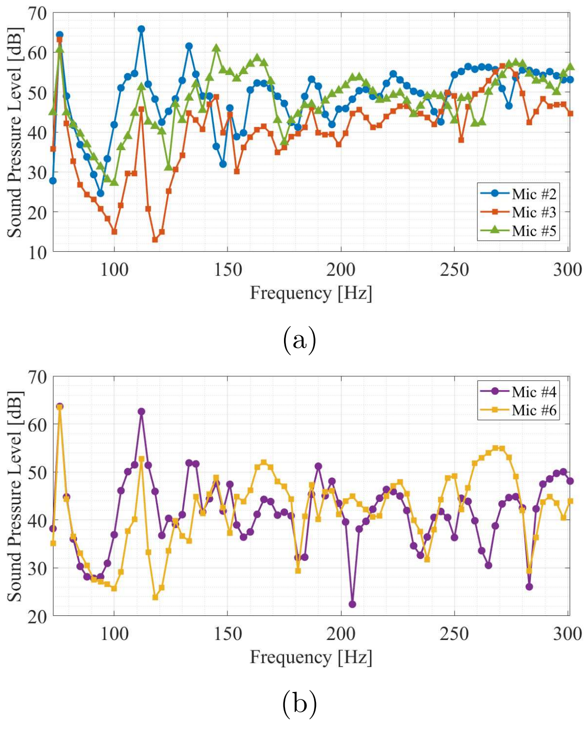

Fig. 6.19 Predicted sound pressure level at selected internal microphones for Configuration 1: (a) Microphones 2, 3, and 5; (b) Microphones 2 and 6.

A qualitative analysis reveals the presence of well-defined SPL peaks at low frequencies, occurring at excitation frequencies of approximately 76, 112, 133, 145, and 166 Hz.

In the reference configuration (body-in-white), characterised by an excitation area equal to A and perfectly reflecting boundaries, the dominant pressure peaks were instead observed at excitation frequencies of 73, 106, 130, and 160 Hz, corresponding to the acoustic natural frequencies of the cavity under rigid-wall boundary conditions (see Section 4.4.4 and Figure 6.7). As expected, in the presence of acoustic treatment, resonant behaviour is still observed although with a shift in the resonance frequencies for comparable modal patterns.

Figure 6.20 presents the contour plots of the acoustic pressure field evaluated on a cut plane corresponding to Configuration 1, for selected excitation frequencies.

At an excitation frequency of 76 Hz, a cavity resonance is observed, with all five microphones exhibiting peaks in the SPL response. In particular, microphones 3, 4, and 6 reach their absolute maximum values within the analysed frequency range, with pressure levels of 63.2 dB, 63.6 dB, and 63.5 dB, respectively. Microphones 2 and 5 also exhibit local maxima, reaching 64.3 dB and 60.6 dB, respectively. The low spatial variability of the pressure field (ΔSPL $< 4\,$dB) is clearly visible in Figure 6.20a, which shows a nearly uniform pressure distribution, characteristic of the axial modal shape excited at this frequency. A well-defined YZ-oriented nodal plane can be identified, while the second nodal plane is not visible in this cut section but is clearly observed in Figure 6.23a. This pattern corresponds to the second longitudinal acoustic mode. In the reference rigid-wall configuration, the same modal pattern was observed at an excitation frequency of 73 Hz, although with lower pressure levels compared to those obtained here, with a maximum value of approximately 51.1 dB at microphone 2.

The next pressure peak observed at all five microphones occurs at an excitation frequency of 112 Hz. The corresponding pressure distribution on the microphone plane is shown in Figure 6.20b, clearly highlighting the presence of a single longitudinal nodal plane. At this frequency, microphone 2 reaches its absolute maximum pressure level, equal to 65.8 dB, followed by microphone 4 with a value of 62.6 dB. Microphones 5, 6, and 3, located in proximity to the nodal plane, exhibit lower pressure levels compared to microphones 2 and 4, which are positioned away from it, reaching values of 51.2 dB, 52.7 dB, and 45.7 dB, respectively. In the reference rigid-wall configuration, a similar pressure

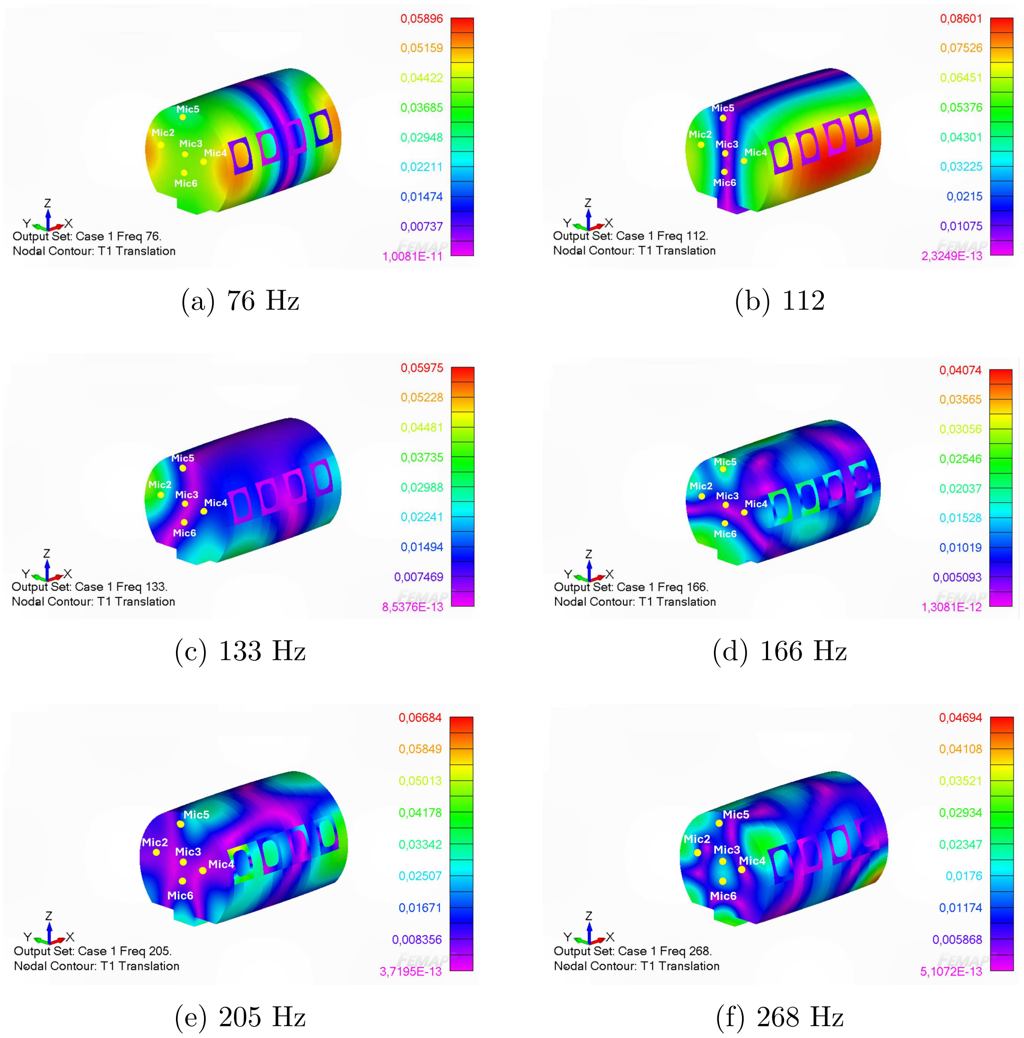

(a) 76 Hz (b) 112

(c) 133 Hz (d) 166 Hz

(e) 205 Hz (f) 268 Hz

Fig. 6.20 Acoustic cavity pressure field distribution on a cut plane corresponding to Configuration 1 for eight excitation frequencies.

distribution was observed at an excitation frequency of 106 Hz (see Figure 6.8b), although higher pressure levels were attained, with a maximum value of 69.0 dB recorded at microphone 2.

The pressure distribution obtained at an excitation frequency of 133 Hz is shown in Figure 6.20c. The pressure field exhibits a nodal plane that is slightly inclined with respect to the vertical direction, together with a YZ-oriented nodal plane, resulting in a pattern that resembles the distribution observed at 130 Hz in the rigid-wall configuration (see Figure 6.8c). At this resonance frequency, microphones 2, 4, and 3 exhibit relative maxima, reaching pressure levels of 61.5 dB, 51.9 dB, and 44.7 dB, respectively. In contrast, microphone 6, located closest to the nodal plane, exhibits a relative minimum, with a pressure level of 35.7 dB.

In the present case with acoustic damping, a higher excitation frequency of 166 Hz is required to identify a pressure distribution resembling the mode with index (3,1,0), which is excited at 160 Hz in the rigid-wall configuration (see Figure 6.8d). The pressure distribution shown in Figure 6.20d highlights the presence of an XY-oriented nodal plane. Microphone 3 lies on this nodal plane and therefore exhibits the lowest pressure level among the considered microphones, equal to 41.3 dB. Microphone 4, also located close to the nodal region, records a slightly higher value of 44.3 dB. In contrast, microphone 5, positioned away from the nodal plane, exhibits the highest pressure level, reaching 57.2 dB, followed by microphone 2 with 52.2 dB. Microphone 6 shows a local peak in the SPL response, reaching 52.0 dB.

As the excitation frequency increases, the identification of modal patterns corresponding to the natural frequencies of the rigid-wall configuration becomes progressively more difficult. This is primarily due to the decrease of the imaginary part of the impedance, which moves the system away from the perfectly reflecting boundary condition. Moreover, at higher frequencies, the SPL response exhibits less pronounced peaks, with broader and more damped resonance curves, reflecting the increased effect of acoustic absorption. To further investigate this behaviour, the response at excitation frequencies of 205 Hz and 268 Hz is analysed. The former is selected as it represents a frequency at which the modal pattern remains clearly identifiable despite the damping effects, while the latter is associated with a radial modal pattern.

More specifically, at 205 Hz (see Figure 6.20e), the pressure distribution reveals the presence of three radial nodal planes and one axial nodal plane. Microphone 4 is located at the intersection of these nodal planes and therefore exhibits the lowest pressure level within the analysed frequency range, equal to 22.4 dB. The highest pressure level is instead recorded at microphone 5, which is located away from the nodal regions and reaches 53.5 dB. It is also interesting to observe a localized cavity resonance in the vicinity of the window near microphone 4, characterised by the presence of a longitudinal nodal plane for the small cavity surrounding the cabin window.

The pressure distribution obtained at an excitation frequency of 268 Hz is shown in Figure 6.20f. The pressure field exhibits the presence of an approximately circumferential nodal plane within the section. Microphone 6 lies near the center of this region and exhibits a relative maximum, reaching a pressure level of 55 dB, second only to the absolute maximum recorded at 76 Hz. Microphones 2 and 3, also located away from the nodal region, exhibit comparable pressure levels, approximately equal to 55.3 dB. In contrast, microphone 5, located closer to a nodal region, records a slightly lower value of 52.3 dB, while microphone 4, positioned even closer to the nodal region, exhibits a significantly lower pressure level of 38.7 dB.

A more direct comparison between the rigid and trimmed configurations can be performed by analyzing the NR in one-third octave bands (Figure 6.21). For microphone 2, considering an excitation area equal to A, the figure reports both numerical (blue lines) and experimental (black lines) NR values. Solid lines refer to the body-in-white configuration, while dashed lines correspond to the trimmed case with acoustic treatment.

A numerical–numerical comparison shows that the NR is generally higher in the trimmed configuration than in the rigid case, as expected. An exception is observed at the centre frequency of 80 Hz, where the NR in the rigid configuration is 41.6 dB, compared to 30.6 dB in the trimmed case. This behaviour is consistent with the higher SPL observed in the trimmed configuration at frequencies associated with the second longitudinal cavity mode.

A comparison between the experimental body-in-white and trimmed results confirms that the trimmed configuration provides higher NR values than the

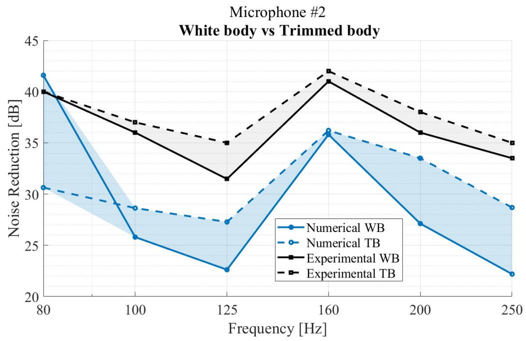

Fig. 6.21 Noise Reduction in one-third octave bands for microphone 2 in Configuration 1. Numerical results are shown in blue, with solid and dashed lines referring to the body-in-white and trimmed configurations, respectively. Experimental results are reported in black, with solid and dashed lines corresponding to the body-in-white and trimmed configurations, respectively.

untreated case. The overall trend is similar in both experimental configurations, with a maximum difference of approximately 3.5 dB at 125 Hz.

The numerical–experimental comparison for the trimmed configuration shows a satisfactory agreement for microphone 2, with a Pearson correlation coefficient of $r = 0.85$. In particular, both curves exhibit a decreasing trend between 80 Hz and 125 Hz, where a global minimum is reached. This minimum is associated with the presence of acoustic natural frequencies within the frequency band centered at 125 Hz. At this frequency, the experimentally measured NR is approximately 35 dB, while the numerical prediction yields 27.3 dB. Both curves then increase, reaching an absolute maximum at 160 Hz, with a difference of about 5.8 dB between numerical and experimental results. In the frequency range from 160 Hz to 250 Hz, both curves show a decreasing trend, reaching values of approximately 35 dB in the experimental case and 28.7 dB in the numerical prediction.

Overall, the numerical model tends to overestimate the effect of the acoustic treatment. In fact, the variations in NR between the rigid and trimmed configurations are more pronounced in the numerical results than in the experimental data, indicating an overprediction of the sound absorption capability of the modelled material.

Discussion

The forced-response analysis represents a valid alternative to classical eigenfrequency analysis when the objective is to identify the acoustic natural frequencies of a cavity under non-rigid boundary conditions. In the present study, the acoustic cavity, with absorbing material applied to selected internal side-wall surfaces and modelled through `CAABSF` surface elements, is excited using a broadband (flat-spectrum) input. This approach allows the identification of the so-called damped natural frequencies from the peaks of the acoustic response.

The acoustic impedance assigned to the absorbing boundaries is defined through a simplified reconstruction procedure. The real component is assumed equal to the characteristic impedance of air, ρc, while the frequency-dependent imaginary component is derived from the experimental absorption coefficient $\alpha(f)$ through Eq. 6.3. This representation should be regarded as an approximation, since only the absorption coefficient is experimentally available and no direct measurement of the complex acoustic impedance was performed. Considering the one-third octave bands retained for the numerical–experimental comparison, from the centre frequency of 80 Hz to that of 250 Hz, the highest frequency effectively involved in the post-processing corresponds to the upper limit of the 250 Hz band, i.e. approximately 280 Hz. Within this frequency interval, the imaginary part of the acoustic impedance decreases significantly, from $Z_I = 6410$ at 73 Hz – corresponding to the lower numerical frequency associated with the one-third octave band centred at 80 Hz – to $Z_I = 1537$ at 280 Hz. This decrease reflects a progressive reduction of the reactive behaviour of the boundary condition and a departure from the ideal rigid-wall condition.

As shown by the numerically predicted SPL levels at the five receiver locations of Configuration 1 (Fig. 6.19), for a given modal pattern, the pressure peaks in the trimmed configuration occur at higher frequencies compared to the rigid-wall case (Fig. 6.7). For instance, a frequency shift of approximately 6 Hz is observed for the first longitudinal mode (from 106 Hz in the rigid case to 112 Hz in the trimmed configuration). In addition, the corresponding pressure levels are generally reduced due to the presence of acoustic absorption. An exception to this trend is observed at an excitation frequency of 76 Hz, which corresponds to the axial mode (2,0,0) in the trimmed configuration, compared to 73 Hz in the rigid case. Despite the similar spatial pressure distribution, higher pressure levels are recorded in the trimmed configuration (64.3 dB at microphone 2) than in the rigid case (51.1 dB). At this frequency, the imaginary part of the impedance assumes a relatively high value ($Z_I \approx 6153$), corresponding to a strongly reactive boundary condition. This leads to a redistribution of acoustic energy within the cavity and may result in local amplification phenomena, producing pressure levels even higher than those observed under perfectly reflecting conditions.

As the excitation frequency increases, the identification of nodal planes becomes progressively more difficult, and their spatial distribution deviates from the regular patterns observed in the rigid-wall configuration.

In general, lower pressure levels are observed in the presence of acoustic treatment, due to the dissipative effects introduced by the absorbing material. This behaviour is more clearly highlighted by analyzing the NR, for instance at microphone 2. A numerical–numerical comparison between rigid and trimmed configurations shows higher NR values in the trimmed case, as expected. However, this trend is not observed at the centre frequency of 80 Hz, which includes the excitation frequency of 76 Hz.

The physical consistency of the acoustic treatment modelling is assessed through comparison with experimental results for microphone 2. The numerical and experimental NR curves show a satisfactory agreement in terms of overall trend, with a maximum at 160 Hz and a minimum at 125 Hz. In absolute terms, differences between numerical and experimental NR values range from approximately 4.5 dB to 9.4 dB, with experimental values consistently higher than the numerical predictions. The comparison between numerical and experimental results indicates that the numerical model tends to overestimate the effect of the acoustic treatment. In particular, the variations in NR between rigid and trimmed configurations are more pronounced in the numerical results than in the experimental data, suggesting an overprediction of the sound absorption capability of the `CAABSF` elements used in the model.

The main objective of this validation is to assess the physical consistency of the adopted modelling approach, including the implementation of the absorbing material, the frequency shift of the resonances, and the resulting modification of the pressure field. It must be emphasized that the acoustic impedance is here approximated, as the real part is assumed equal to ρc, while the imaginary

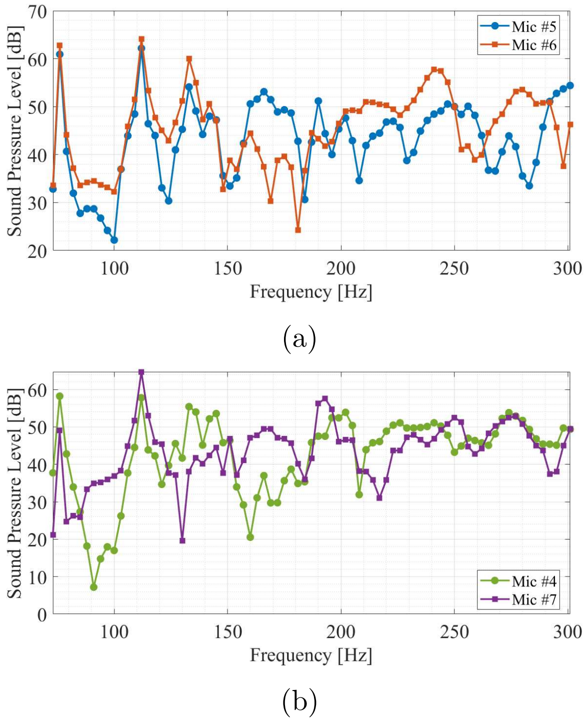

Fig. 6.22 Predicted sound pressure level at selected internal microphones for Configuration 2: (a) Microphones 5 and 6; (b) Microphones 4 and 7.

part is derived accordingly. Overall, the results show a satisfactory level of agreement between numerical and experimental data, indicating that the adopted modelling approach is capable of capturing the key physical phenomena governing the vibroacoustic response of the cavity in the presence of acoustic treatment.

Configuration 2

Similarly to Configuration 1, the SPL response is reported for the four microphones of Configuration 2. In particular, Figure 6.22a shows the pressure levels at microphones 5 and 6, located closer to the loudspeaker, while Figure 6.22b reports the results for microphones 4 and 7, positioned farther away.

Consistently with the observations made for Configuration 1, the SPL curves exhibit well-defined peaks at low frequencies, in particular at 76 Hz, 112 Hz, 133 Hz, and 166 Hz. Figure 6.23 presents the contour plots of the acoustic pressure field evaluated on a cut plane corresponding to Configuration 2, for selected excitation frequencies.

Figure 6.23a shows the pressure distribution obtained at an excitation frequency of 76 Hz, corresponding to the axial cavity mode $(2, 0, 0)$. This resonance condition leads to elevated pressure levels at all four microphones. In particular, microphone 4 reaches its absolute maximum pressure level, equal to 58.2dB. The highest pressure value is recorded at microphone 6, followed by microphone 5, both located away from the nodal planes, with pressure levels of 62.7 dB and 60.9 dB, respectively. Microphone 7, located closer to the nodal region, exhibits a lower pressure level of 49.1 dB. As observed for Configuration 1, the pressure levels at 76 Hz are higher in the trimmed configuration than in the rigid-wall case for the same modal pattern $(2, 0, 0)$, where the maximum pressure — recorded at microphone 6 — was equal to 46.9 dB.

The pressure distribution observed at 106 Hz in the rigid-wall configuration — corresponding to an acoustic mode characterised by a single longitudinal nodal plane — is, as previously discussed, recovered at an excitation frequency of 112 Hz in the trimmed case (Figure 6.23b). At this resonance frequency, microphones 7, 6, and 5 reach their absolute maximum pressure levels, equal to 64.7 dB, 64.1 dB, and 62.2 dB, respectively. The pressure distribution clearly exhibits a decrease in amplitude when moving from the rear bulkhead toward the forward bulkhead. Accordingly, microphone 4, located closer to the forward bulkhead, records the lowest pressure level among the four microphones, equal to 57.8 dB.

As previously observed for Configuration 1, a pressure distribution resembling the modal pattern $(2, 1, 0)$ is excited at an excitation frequency of 133 Hz (Figure 6.23c). However, axial nodal planes are not as clearly defined as those observed in the rigid-wall configuration (see Figure 6.10c). In particular, the two axial nodal planes tend to merge toward the lower region of the section, forming a U-shaped nodal line. Microphone 7, located in proximity to one of the vertical nodal planes, exhibits the lowest pressure level among the four microphones, equal to 38.1 dB. Microphones 4 and 5, positioned on opposite sides of the nodal region toward the forward bulkhead, exhibit comparable pressure levels of approximately 55 dB. Microphone 6, located farther from the nodal regions, records the highest pressure level among the four, equal to 60.0 dB.

At an excitation frequency of 166 Hz, the pressure distribution shown in Figure 6.23d highlights a modal pattern that can be associated with the $(3, 1, 0)$ mode, although the nodal lines are not always continuous and deviate from perfectly vertical orientations. At this frequency, microphones 5, 7, and 4 exhibit relative maxima, reaching pressure levels of 53.1 dB, 49.5 dB, and 37.0 dB, respectively. Microphone 6, located closer to a nodal region, records a pressure level of 37.5 dB.

As for Configuration 1, contour plots at higher excitation frequencies are also reported, namely at 205 Hz and 268 Hz, allowing the visualization of the corresponding modal patterns along the longitudinal direction.

Figure 6.23e shows the pressure distribution at 205 Hz. In addition to the presence of two radial nodal planes, the pattern suggests the existence of two vertical nodal planes, although they are not clearly distinguishable. The nodal region is relatively extended, resulting in comparable pressure levels at the four microphones, ranging from 49.3 dB at microphone 6 to 46.4 dB at microphone 7.

Figure 6.23f shows the pressure distribution at 268 Hz. An approximately circumferential nodal plane can be identified, extending along the longitudinal direction and intersecting the region where the microphones are located. Microphone 7 exhibits the highest pressure level, equal to 50.2 dB, followed by microphones 4, 6, and 5, with values of 48.1 dB, 46.9 dB, and 36.7 dB, respectively.

A more direct comparison between the rigid and trimmed configurations can be achieved by analyzing the NR, as shown in Figure 6.24. This figure reports, for microphone 6, the NR values in one-third octave bands within the frequency range 80–250 Hz. The numerical results are shown by blue curves, with the solid line referring to the rigid configuration and the dashed line to the trimmed case. A first qualitative comparison between numerical results shows, as expected, that the NR is generally higher in the trimmed configuration than in the rigid case. An exception is observed at the centre frequency of 80 Hz, where the NR in the body-in-white configuration exceeds that of the trimmed case by approximately 13 dB. This behaviour is consistent with the higher pressure

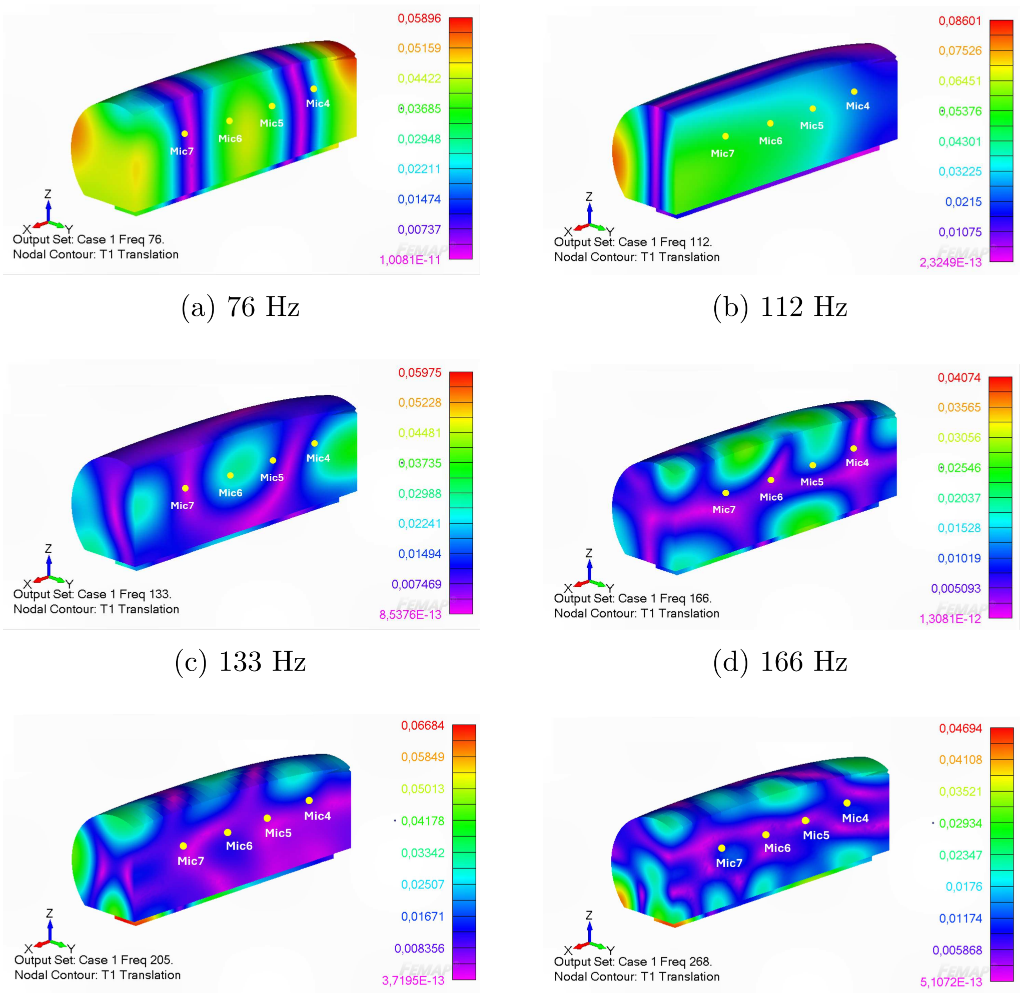

(a) 76 Hz (b) 112 Hz

(c) 133 Hz (d) 166 Hz

(e) 205 Hz (f) 268 Hz

Fig. 6.23 Acoustic cavity pressure field distribution on a cut plane corresponding to Configuration 2 for eight excitation frequencies.

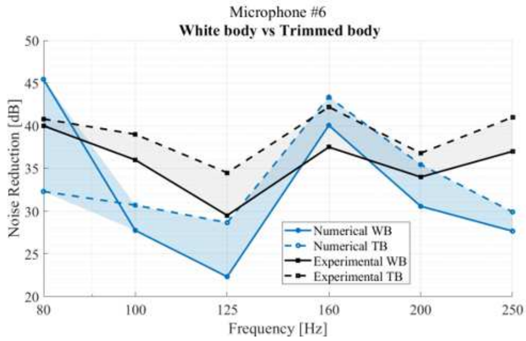

Fig. 6.24 Noise Reduction in one-third octave bands for microphone 6 in Configuration 2. Numerical results are shown in blue, with solid and dashed lines referring to the body-in-white and trimmed configurations, respectively. Experimental results are reported in black, with solid and dashed lines corresponding to the body-in-white and trimmed configurations, respectively.

levels observed in the trimmed configuration in the frequency range around 80 Hz, where the axial mode $(2, 0, 0)$ occurs. In particular, microphone 6 records 46.9 dB in the rigid case and 62.7 dB in the trimmed configuration, which can be related to the high value of the reactive component of the impedance at this frequency ($Z_I \approx 6152$). Beyond 80 Hz, the trimmed configuration consistently exhibits higher NR values than the rigid case. The difference in NR between the two configurations is approximately 3.0 dB at 100 Hz, 6.3 dB at 125 Hz, 3.3 dB at 160 Hz, 4.8 dB at 200 Hz, and 2.2 dB at 250 Hz. However, no clear monotonic trend of the NR improvement with frequency can be identified. Although the real part of the impedance is kept constant, the imaginary component decreases with increasing frequency. Despite this known behaviour of Z_I, the variation in NR between rigid and trimmed configurations does not follow a linear trend, ranging from -13 dB at 80 Hz to $+2.2$ dB at 250 Hz with a maximum benefit in the band centered at 125 Hz, where the value of $+6.3$ dB is observed.

Figure 6.24 also includes the experimentally measured NR for both configurations, with the body-in-white and trimmed cases represented by black solid and dashed lines, respectively. A comparison between experimental results for the rigid and trimmed cases confirms that the NR is higher in the presence of acoustic treatment.

Of particular interest for the purposes of this study is the comparison between numerical and experimental NR for the trimmed configuration. Considering the two dashed curves, a very satisfactory agreement in terms of overall trend can be observed for Microphone 6, with a Pearson correlation coefficient of $r = 0.50$. In particular, both curves exhibit a decreasing trend between 80 Hz and 125 Hz, where a minimum NR value is reached. This behaviour is consistent with the presence of cavity modes within the frequency band centered at 125 Hz, which produce strong SPL peaks, as discussed previously. At 160 Hz, both numerical and experimental curves exhibit a maximum, with a very good agreement also in terms of absolute values: 43.3 dB for the numerical result and 42.2 dB for the experimental one. The curves then decrease almost overlapping up to 200 Hz, where the experimental value exceeds the numerical prediction by approximately 1.4 dB. In the frequency range from 200 Hz to 250 Hz, the two curves start to diverge. In particular, the experimental NR increases, reaching approximately 41 dB, while the numerical prediction decreases down to approximately 30 dB.

Discussion

The contour plots reported for Configuration 2, with microphones distributed along the longitudinal direction, provide a comprehensive visualization of the evolution of the acoustic pressure field as a function of frequency. The introduction of acoustic absorbing material along the internal surfaces of the fuselage significantly modifies the pressure distribution within the cabin. Depending on the excitation frequency, this results in either attenuation or amplification of the SPL. This behaviour is primarily governed by the frequency-dependent imaginary part of the acoustic impedance, which varies from $Z_I = 6410$ at 73 Hz to $Z_I = 1537$ at 280 Hz, thus progressively reducing the reactive character of the boundary condition and moving away from the ideal rigid-wall behaviour.

A numerical–numerical comparison between the rigid and trimmed configurations shows that similar pressure distributions —associated with specific modal patterns — are obtained at different excitation frequencies, generally shifted toward higher values in the trimmed case. For instance, the axial mode $(2, 0, 0)$ shifts from 73 Hz to 76 Hz, the first longitudinal mode from 106 Hz to 112 Hz, the mixed $(2, 1, 0)$ mode from 130 Hz to 133 Hz, and the $(3, 1, 0)$ mode from 160 Hz to 166 Hz. As the frequency increases, the identification of nodal planes becomes progressively more difficult, reflecting the effects of complex impedance boundary conditions, which distort the ideal modal shapes observed in the rigid-wall configuration. In addition to the frequency shift, variations in the pressure amplitude are also observed. In general, the presence of acoustic treatment leads to lower SPL values due to energy dissipation at the boundaries. However, an exception is observed for the axial mode $(2, 0, 0)$, where the trimmed configuration exhibits higher pressure levels. For example, at microphone 6, an increase of approximately 15.8 dB is observed compared to the rigid case. This behaviour is associated with the high value of the reactive component of the impedance at low frequencies, which promotes energy confinement within the cavity and may lead to local amplification effects.

A comparison in terms of NR in one-third octave bands further confirms these observations. The trimmed configuration generally exhibits higher NR values than the rigid case, indicating the effectiveness of the acoustic treatment. The only exception occurs at the centre frequency of 80 Hz, which includes the excitation frequencies of 73 Hz and 76 Hz, where the aforementioned amplification mechanisms dominate.

Furthermore, the numerical predictions for the trimmed configuration show a very good agreement with the experimental results in terms of overall trend, with discrepancies becoming more evident only in the frequency range between 200 Hz and 250 Hz. The numerical model is therefore able to reproduce the main features of the acoustic response, including both attenuation and resonance-driven amplification phenomena.

However, it must be emphasized that the acoustic impedance adopted in the numerical model is not directly measured. In the present work, the real part is assumed equal to ρc, while the imaginary component is derived from the absorption coefficient. This representation inherently constitutes an approximation and, although physically consistent, would require further sensitivity analyses to achieve a more accurate characterization of the material properties. Such investigations, however, fall beyond the scope of the present study. In addition to modelling assumptions, it is important to recognize that the experimental results themselves are influenced by the mounting conditions of the absorbing material. In particular, for porous materials, the presence of an air gap between the material and the supporting structure is known to significantly enhance the absorption performance. As a consequence, experimental data should not be interpreted as absolute reference values, but rather as measurements that depend on the specific installation conditions.

Within this framework, the objective of the present validation is not to achieve a perfect quantitative agreement, but rather to assess the physical consistency of the numerical model and its ability to reproduce the governing mechanisms of the acoustic response. From this perspective, the results indicate a satisfactory level of physical consistency. The acoustic pressure field exhibits a smooth and continuous spatial distribution, both within the analysed cross-sections and along the entire fuselage barrel. No unphysical discontinuities or irregular patterns are observed, and all variations in pressure are characterised by gradual and physically meaningful transitions. This aspect is particularly significant given the complexity of the boundary condition implementation. The correct application of impedance boundary conditions over a complex geometry represents a non-trivial task, and the absence of numerical artifacts confirms the robustness of the adopted modelling strategy.

Furthermore, the analysis consistently captures the key physical mechanisms governing the vibroacoustic response of the cavity. The reduction of pressure levels due to the presence of acoustic treatment is correctly reproduced, while local pressure amplifications are always associated with resonance phenomena. In particular, the occurrence of SPL peaks is systematically correlated with the excitation of cavity modes, demonstrating a strong coherence between the numerical predictions and the underlying acoustic theory.

The agreement with the experimental data obtained for both the body-in-white and trimmed configurations supports the suitability of the proposed modelling approach. Although some discrepancies remain, mainly due to the simplified impedance representation, experimental installation effects, uncertainties in the effective source field and differences between the actual and modelled cabin geometry, the model captures the main vibroacoustic mechanisms governing the cabin response. In the analysed frequency range, the numerical predictions reproduce the main experimental NR trends at the most representative receiver locations. In addition, the agreement between predicted and measured NR levels within the sensitivity envelope further strengthens the validation. This result highlights that the selected equivalent excitation areas $A/2$, A and $2A$ provide physically meaningful representations of the effective source region, rather than arbitrary fitting parameters. The model therefore provides a suitable predictive basis for future cabin noise studies and comparative assessments of vibroacoustic modelling strategies.

Chapter 7

Conclusions and Future Developments

7.1 Main Conclusions

The present thesis has developed and validated a high-fidelity coupled structural–acoustic FE framework for the prediction of cabin noise in the Piaggio P180 Avanti EVO cockpit–cabin fuselage assembly. The work focuses on the low- to mid-frequency range associated with the first BPF harmonics, where the vibroacoustic response of turboprop aircraft cabins is governed by discrete structural modes, acoustic cavity resonances and fluid–structure interaction phenomena. In this range, the internal acoustic response is strongly receiver-dependent; therefore, predictive reliability requires an accurate representation of both the fuselage deformation mechanisms and the spatial distribution of the cabin pressure field.

The main contribution of the thesis is not limited to the construction of a detailed numerical model. Rather, the work defines a validated deterministic modelling strategy for a real full-scale aircraft configuration. In vibroacoustic modelling, the discretisation of both coupled domains, namely the fuselage structure and the internal acoustic cavity, must be related to the maximum excitation frequency to be resolved. In the present work, this frequency is defined by the third BPF harmonic of the reference propeller operating condition, while the modal and mesh requirements are assessed over an extended frequency range in order to account for the possible contribution of higher-frequency modes to the modal frequency response. For the structural mesh, the adopted approach is more detailed and physically grounded than a discretisation based only on the propagation speed of elastic waves in the structure. Each structural sub-component is analysed in order to identify its dynamic characteristics, namely natural frequencies and mode shapes, which depend on geometry, material properties, thickness, local stiffening and boundary conditions. This allows a component-specific bending wavelength used to define the corresponding structural element size. When uncertainties exist in the local boundary conditions, the least constrained configuration is retained, leading to a conservative estimate of the required mesh resolution. For the acoustic model, the mesh resolution is defined from the acoustic wavelength associated with the same extended frequency range, while maintaining compatibility with the structural discretisation along the fluid–structure interfaces. The resulting framework is therefore not merely a refined FE model, but a frequency-driven and physics-based modelling strategy in which the discretisation of both domains is tied to the dynamic phenomena that must be resolved.

From a technological point of view, the developed framework provides a numerical tool for cabin noise prediction in the Piaggio P180 Avanti EVO cockpit–cabin fuselage assembly up to the third BPF harmonic. By combining the fuselage structural model, the passenger cabin acoustic cavity and the fluid–structure coupling interfaces, it enables the analysis of noise transmission mechanisms, receiver-dependent pressure distributions and acoustic treatment effects, providing a basis for future propeller-induced noise and noise reduction studies on this aircraft configuration.

The reliability of the framework has been established progressively. The structural model was assessed through modal correlation with available free–free experimental data, showing that the dominant fuselage deformation mechanisms, including global ovalisation and lobed modes, are reproduced despite residual frequency discrepancies. These discrepancies are mainly associated with modelling uncertainties in the experimental test article, particularly the representation of the cabin floor, whose actual continuity and stiffness contribution were not fully documented. The acoustic model was verified against the analytical solution of an equivalent cylindrical cavity, confirming its physical consistency for the main longitudinal and mixed cavity modes. The coupled model was then assessed through a preliminary forced-response analysis, which confirmed the correct transfer of vibrational energy from the fuselage structure to the internal acoustic cavity and showed the expected relationship between acoustic resonances, pressure amplification and local minima in NR.

The full numerical–experimental validation was performed using acoustic test data obtained from the same Piaggio P180 fuselage barrel test article used for the structural modal correlation. Since the experimental database provided receiver-dependent NR rather than independent internal SPL spectra, the validation was carried out in terms of frequency-dependent NR trends. During the experimental test, the external loudspeaker was positioned very close to the fuselage skin; therefore, in the numerical model, it was represented through an equivalent pressure load applied to a reference fuselage area A, defined as the portion of the skin directly facing the source and selected consistently with the estimated vibrating surface of the loudspeaker. The additional $A/2$ and $2A$ cases were introduced to account for uncertainty in the effective spatial extent of the incident acoustic field. Two configurations were considered. For the body-in-white configuration, the model reproduced the main experimental NR trends, with the strongest correlation observed at receiver locations closer to the excitation region. At these locations, the response is mainly governed by the directly excited field. Conversely, larger discrepancies occurred at receivers farther from the source or closer to the floor, where reflected field contributions and floor representation become more influential. The impedance sensitivity study on the closing panels delimiting the passenger cabin cavity showed that the rigid-wall condition provides the closest overall agreement with the untreated experimental configuration. The non-monotonic dependence of the response on impedance confirms that changing the boundary condition modifies both the reflected field and the modal pressure distribution inside the cavity, leading to local amplification or cancellation effects depending on frequency and receiver position.

For the trimmed configuration, the absorbing material was represented through equivalent impedance boundary conditions, with the complex impedance reconstructed from the measured absorption coefficient through a simplified procedure. The numerical comparison between the body-in-white and trimmed configurations shows that the introduction of absorbing material modifies the acoustic response of the cavity, producing a shift of the resonance peaks and a redistribution of the internal pressure field. The treatment effect is strongly frequency-dependent: although the absorbing material generally increases NR, local increases of the internal SPL are observed in specific frequency bands, due to the reactive component of the reconstructed impedance and the modified resonance behaviour of the cavity. The comparison with experimental data confirms that the model captures the main effect of the treatment, although the predicted variation between untreated and treated configurations is more pronounced than in the measurements, indicating an overestimation of the treatment effect. Despite this limitation, the model correctly reproduces the main influence of the absorbing material on the cabin response and provides a physically consistent basis for assessing acoustic treatment effects.

Overall, the thesis demonstrates that the developed structural–acoustic framework provides a reliable numerical basis for low-frequency cabin noise studies on the Piaggio P180 Avanti EVO fuselage.

7.2 Limitations

The main limitations of the validation process arise from the numerical representation of experimental details associated with the test configurations used as validation references, which were not fully defined by the available documentation. The experimental datasets obtained from previous full-scale test campaigns provide a valuable basis for assessing both the structural dynamics and the coupled structural–acoustic response of the model. However, some experimental details had to be reconstructed in the numerical model through physically consistent modelling assumptions. Consequently, the remaining discrepancies between numerical and experimental results should be interpreted in relation to these assumptions, both in the comparison of natural frequencies and mode shapes and in the prediction of local, receiver-dependent NR.

The cabin floor represents one of the most relevant sources of uncertainty. In the numerical model, the floor is represented as a continuous structural component, whereas the available information suggests that the floor in the experimental fuselage barrel was only partially installed and locally discontinuous. Since the same structural representation is used for both the modal validation and the coupled acoustic test simulation, this assumption affected the results at both levels. Indeed, in the structural validation, the largest mode shape discrepancies were associated with modes involving deformation of the lower fuselage region. In the acoustic comparison, the largest differences between numerical and experimental NR values were observed for receivers close to the floor or farther from the source, where reflected acoustic fields and boundary condition assumptions play a more significant role.

More specifically, further limitations concern the numerical reproduction of the acoustic test configuration.

The close proximity of the loudspeaker to the fuselage skin justified the use of an equivalent harmonic pressure load applied directly to the fuselage panel facing the source, with a reference excitation area A defined from the estimated vibrating surface of the loudspeaker. However, in the experimental test, the incident acoustic field was not necessarily confined to this limited region. Additional portions of the fuselage could be excited directly by the acoustic field or indirectly through reflections within the test environment, including reflections associated with the floor and surrounding boundaries. This approximation affects the absolute level of the predicted response, because the total acoustic energy introduced into the coupled system depends on the effective loaded area. For this reason, the comparison of absolute NR values must be interpreted together with the sensitivity analysis on the excitation area, while the frequency-dependent trend of the NR curves represents the more robust validation indicator.

An additional limitation concerns the acoustic boundary conditions at the closing bulkheads in the body-in-white configuration. The bulkheads used during the experimental test were primarily structural closures of the fuselage barrel and were not designed to impose a well-characterised acoustic impedance. For this reason, the analyses performed with impedance values different from the rigid-wall condition should be interpreted as numerical sensitivity studies rather than as alternative validated boundary condition models. Their purpose was to define a confidence range and to assess the influence of the closing-boundary impedance on the internal pressure field and NR, not to identify a unique physical impedance value for the experimental setup.

The trimmed configuration introduces a further approximation related to the acoustic characterisation of the absorbing material. Since only the normal-incidence absorption coefficient $\alpha(f)$ was available, the complex acoustic impedance could not be directly determined. The real part of the impedance was therefore assumed equal to the characteristic impedance of air, while the imaginary component was reconstructed from the measured absorption coefficient. This provides a simplified impedance representation of the treatment rather than a complete material characterisation. The numerical–experimental comparison showed that this approximation is sufficient to reproduce the main physical effect of the acoustic treatment, including the modification of the cavity response and the frequency-dependent variation of NR. However, the numerical model tends to overestimate the treatment effect.

It should also be noted that the effectiveness of acoustic treatments is strongly influenced by installation details. The numerical model represents an idealised treatment installation, with prescribed impedance conditions applied to the selected cavity surfaces. In the experimental configuration, the actual installation may have included local discontinuities, imperfect contact, air gaps or non-uniform material placement. In addition, as in any full-scale acoustic test, the experimental data may include measurement uncertainties, background noise and uncontrolled environmental effects. These aspects can affect both the body-in-white and trimmed configurations.

Overall, these limitations do not compromise the validity of the developed framework, but define the level of confidence with which local numerical–experimental discrepancies should be interpreted.

7.3 Future Developments

A central extension of the present work concerns the application of realistic propeller-induced excitation. The Piaggio P180 Avanti EVO is characterised by a five-blade pusher-propeller configuration, for which the first Blade-Passage Frequency harmonics fall within the frequency range targeted in this thesis. Future studies should therefore include aerodynamic and aeroacoustic analyses of the propellers under representative operating conditions, in order to compute the pressure fields associated with the BPF harmonics. A suitable strategy would consist of first evaluating the unsteady aerodynamic loading on the blades and then predicting the radiated acoustic field through an aeroacoustic formulation, such as a Ffowcs Williams–Hawkings/Farassat-type approach. The resulting pressure distributions, including possible installation and scattering effects, could then be mapped onto the fuselage skin and used as external excitation for the validated structural–acoustic model.

Once realistic excitation fields are available, the validated framework can be used as a basis for future cabin noise mitigation studies. Possible applications include the assessment of alternative trim layouts, local treatments at critical frequencies, acoustic metamaterial solutions, and hybrid passive–active noise-control strategies. In this perspective, the model can support the design of cabin treatments not only by comparing global NR values, but also by analysing the spatial distribution of the internal pressure field at passenger-relevant receiver locations. A specific improvement in this direction should concern the characterisation of acoustic absorbing materials. Future tests should include direct measurements of the complex acoustic impedance, or the identification of equivalent-fluid material parameters, in order to determine both the real and imaginary components of the boundary impedance.

Finally, the numerical framework can be extended from physical acoustic indicators, such as SPL and NR, toward passenger-centred and psychoacoustic metrics. Once the pressure field is reliably predicted at passenger ear locations, the same model can be used to evaluate quantities related to perceived sound quality and comfort, including tonal content, loudness, sharpness, roughness, fluctuation strength and speech-intelligibility indicators. This extension would allow the model to support not only the reduction of cabin noise levels, but also the assessment of the perceived acoustic quality of the Piaggio P180 cabin environment.

References

[1] Harvey H. Hubbard, editor. *Aeroacoustics of Flight Vehicles: Theory and Practice. Volume 1: Noise Sources*. NASA, Hampton, VA, 1991. NASA Reference Publication 1258.

[2] L. Gutin. On the sound field of a rotating propeller. NACA Technical Memorandum 1195, National Advisory Committee for Aeronautics, Washington, DC, 1948.

[3] M. J. Lighthill. On Sound Generated Aerodynamically: I. General Theory. *Proceedings of the Royal Society of London. Series A*, 211(1107):564–587, 1952.

[4] M. J. Lighthill. On Sound Generated Aerodynamically: II. Turbulence as a Source of Sound. *Proceedings of the Royal Society of London. Series A*, 222(1148):1–32, 1954.

[5] M. J. Lighthill. The Bakerian Lecture, 1961: Sound Generated Aerodynamically. *Proceedings of the Royal Society of London. Series A*, 267(1329):147–182, 1962.

[6] M. J. Lighthill. Jet noise. *AIAA Journal*, 1(7):1507–1517, 1963.

[7] Federal Aviation Administration. Code of Federal Regulations, Title 14: Aeronautics and Space, Part 36 — Noise Standards: Aircraft Type and Airworthiness Certification, 1969.

[8] International Civil Aviation Organization. Annex 16 to the convention on international civil aviation — environmental protection, volume i: Aircraft noise, 1971.

[9] National Research Council. *For Greener Skies: Reducing Environmental Impacts of Aviation*. National Academies Press, Washington, DC, 2002. Committee on Aeronautics Research and Technology for Environmental Compatibility.

[10] International Civil Aviation Organization. Icao environmental report 2016: Aviation and climate change. Technical report, ICAO, Montreal, Canada, 2016.

[11] U.S. Government Accountability Office. Commercial aviation: Pilots' and flight attendants' exposure to noise aboard aircraft. Technical Report GAO-18-109R, U.S. Government Accountability Office, Washington, DC, 2017.

[12] Heow Pueh Lee, Sanjay Kumar, Saurabh Garg, and Kian Meng Lim. Assessment of in-cabin noise of wide-body aircrafts. *Applied Acoustics*, 194:108809, 2022.

[13] D. Miljković. Active noise control in light aircraft cabin using multichannel coherent method. *Automatika*, 57(4):1056–1069, 2016.

[14] B. Balakrishnan, A. Rajagopal, and S. Raja. Vibroacoustic performance assessment of aircraft panels in low, mid and high frequency regimes. *Mechanics of Advanced Materials and Structures*, 29(20):2942–2961, 2022.

[15] R. D. Dewald, T. Klimmek, C. Hesse, and R. Winter. Parametric approach to primary structure modeling of aircraft for cabin noise analysis in fem. *CEAS Aeronautical Journal*, 2025.

[16] P. R. Bassett and S. J. Zand. Noise reduction in cabin airplanes. *Transactions of the American Society of Mechanical Engineers*, 56(1):49–56, 1934.

[17] P. Vink and S. Hallbeck. Comfort and discomfort studies demonstrate the need for a new model. *Applied Ergonomics*, 43(2):271–276, 2012.

[18] H. Xue, G. Previati, Ma. Gobbi, and G. Mastinu. Research and development on noise, vibration, and harshness of road vehicles using driving simulators—a review. *SAE International Journal of Vehicle Dynamics, Stability, and NVH*, 7(4):555–577, 2023.

[19] Independent Commission on Civil Aviation Noise (ICCAN). A review of aviation noise metrics and measurement. Technical report, Independent Commission on Civil Aviation Noise, 2020.

[20] H. P. Lee, S. Kumar, S. Garg, and K. M. Lim. Assessment of in-cabin noise of wide-body aircrafts. *Applied Acoustics*, 194:108809, 2022.

[21] G. Aggarwal, N. Mansfield, F. Vanheusden, and S. Faulkner. Human comfort model of noise and vibration for sustainable design of the turboprop aircraft cabin. *Sustainability*, 14(15), 2022.

[22] R. Merino-Martinez and V. S. Buzetelu. Aircraft noise-induced annoyance analysis using psychoacoustic listening experiments. In *Proceedings of the 11th Convention of the European Acoustics Association (Forum Acusticum / Euronoise 2025)*, Malaga, Spain, June 2025. European Acoustics Association.

[23] A. W. Christian and R. Cabell. Initial investigation into the psychoacoustic properties of small unmanned aerial system noise. In *23rd AIAA/CEAS Aeroacoustics Conference*, page 4051. AIAA, 2017.

[24] C. T. Justine Hui, M. J. Kingan, Y. Hioka, G. Schmid, G. Dodd, K. N. Dirks, S. Edlin, S. Mascarenhas, and Y.-M. Shim. Quantification of the psychoacoustic effect of noise from small unmanned aerial vehicles. *International Journal of Environmental Research and Public Health*, 18(17):8893, 2021.

[25] A. J. Torija, Z. Li, and P. Chaitanya. Psychoacoustic modelling of rotor noise. *The Journal of the Acoustical Society of America*, 151(3):1804–1815, 2022.

[26] F. D. Monteiro, R. Merino-Martinez, and L. T. Lima Pereira. Psychoacoustic evaluation of an array of distributed propellers under synchrophasing operation. In *30th AIAA/CEAS Aeroacoustics Conference*, page 3321. AIAA, 2024.

[27] Y. AllahTavakoli, C. Marquis-Favre, M. N. Ichchou, and N. Hamzaoui. A psychoacoustic assessment for enhancing the sound quality of vibrating composite panels. *Acta Acustica*, 9:48, 2025.

[28] S. Krishnamurthy, A. Christian, and S. A. Rizzi. Psychoacoustic test to determine sound quality metric indicators of rotorcraft noise annoyance. In *Proceedings of the International Congress and Exposition on Noise Control Engineering (Inter-Noise)*, Chicago, IL, USA, 2018. Institute of Noise Control Engineering. NASA Technical Report, Document ID: 20200002557.

[29] J. Li, W. X. Liu, Y. Z. Zhang, L. Zhang, and S. S. Li. A novel mpp-nsga algorithm and its application in optimization for radiated noises in the aircraft cabin. *Journal of Vibroengineering*, 19(8):6485–6501, 2017.

[30] Internation Standard ISO 9921:2003. Ergonomics — Assessment of Speech Communication, October 2003. Accessed: 2026-03-09.

[31] J. Ma, Y. Hu, and P. C. Loizou. Objective measures for predicting speech intelligibility in noisy conditions based on new band-importance functions. *The Journal of the Acoustical Society of America*, 125(5):3387–3405, 2009.

[32] P. Zhu, W. Tao, F. Mo, F. Guo, X. Lu, and Xidong Liu. Experimental comparison of speech transmission index measurement in natural sound rooms and auditoria. *Applied Acoustics*, 165:107326, 2020.

[33] H. J. Ban and H. S. Kim. Understanding customer experience and satisfaction through airline passengers' online review. *Sustainability*, 11(15):1–17, 2019.

[34] Satish Dhandole and S.V. Modak. Review of vibro-acoustics analysis procedures for prediction of low frequency noise inside a cavity. *Conference Proceedings of the Society for Experimental Mechanics Series*, 01 2007.

[35] F. Holmström. Structure–Acoustic Analysis Using BEM/FEM: Implementation in MATLAB. Master's thesis, Lund University, 2001. Available at: https://www.lunduniversity.lu.se/lup/publication/3566643.

[36] S. Li. Modal models for vibro-acoustic response analysis of fluid-loaded plates. *Journal of Vibration and Control*, 17(10):1540–1546, 2011.

[37] R. Ohayon and C. Soize. *Structural Acoustics and Vibration: Mechanical Models, Variational Formulations and Discretization.* Academic Press, San Diego, CA, 1998.

[38] P. Li, Y. Yan, and H. Lin. Numerical simulation and experimental researches on the vibration–acoustic coupled property of an aircraft model under strong reverberation noise. *Journal of Vibration and Control*, 23(17):2757–2766, 2017.

[39] B. Dash, T. R. Mahapatra, P. Mishra, D. Mishra, and S. R. Mahmoud. A review of computational methods for vibroacoustic analysis of advanced material structures. *Archives of Computational Methods in Engineering*, 32:2187–2211, 2024.

[40] S. A. Bagherzadeh and M. Salehi. Assessment of cabin noise contributing factors of a turbo-propeller airplane using emd and ssa signal decomposition methods. *Applied Acoustics*, 178:108020, 2021.

[41] D. G. Zimcik. Active control of aircraft cabin noise. In *RTO AVT Symposium on Habitability of Combat and Transport Vehicles: Noise, Vibration and Motion*, RTO-MP-AVT-110, Prague, Czech Republic, 2004. NATO Research and Technology Organization.

[42] F. W. Grosveld. Large civil tiltrotor (lctr2) interior noise predictions due to turbulent boundary layer excitation. NASA Contractor Report NASA/CR-2013-218005, NASA, 2013.

[43] C. Hesse, P. Allebrodt, M. Teschner, and J. Biedermann. Knowledge-based model generation for aircraft cabin noise prediction from pre-design data. *CEAS Aeronautical Journal*, 15:1127–1136, 2024.

[44] R. D. Buehrle, R. S. Pappa G. Fleming, and F. Grosveld. Finite element model development for aircraft fuselage structures. *Sound Vibr*, 35:32–38, 2001.

[45] G. Petrone, G. Melillo, A. Laudiero, and S. De Rosa. A Statistical Energy Analysis (SEA) model of a fuselage section for the prediction of the internal Sound Pressure Level (SPL) at cruise flight conditions. *Aerospace Science and Technology*, 88:340–349, 2019.

[46] F. W. Grosveld, R. H. Cabell, and D. D. Boyd. Interior Noise Predictions in the Preliminary Design of the Large Civil Tiltrotor (LCTR2). In *Proceedings of the 69th Annual American Helicopter Society Forum and Technology Display*, Phoenix, AZ, USA, May 2013. NASA Report NF1676L-15561.

[47] R. L. Hambric, B. M. Gibbs, and F. Fahy. *Engineering Vibroacoustic Analysis: Methods and Applications*. John Wiley & Sons, 2016.

[48] S. Kirkup. The boundary element method in acoustics: A survey. *Applied Sciences*, 2019.

[49] R. H. Lyon and R. G. DeJong. *Theory and Application of Statistical Energy Analysis*. Elsevier, Amsterdam, The Netherlands, 2 edition, 2014.

[50] V. Cotoni, B. Gardner, J. Cordioli, J. Carneal, and C. Fuller. Advanced Modeling of Aircraft Interior Noise Using the Hybrid FE-SEA Method. Technical Report 2008-36-0575, SAE Technical Paper, 2008.

[51] G. C. Everstine. Finite element formulations of structural acoustics problems. *Computers & Structures*, 65(3):307–321, 1997.

[52] J. Rodriguez Ahlquist, P. Huguenet, and P. Higueras. Coupled fem/bem vibroacoustic modeling of turbopropeller cabin noise. In *16th AIAA/CEAS Aeroacosutics Conference*, 2010.

[53] H. M. Lee, S. Garg, K. M. Lim, and H. P. Lee. Comparison of cabin noise of turboprop and turbofan aircrafts. *Applied Acoustics*, 214:109651, 2023.

[54] G. Chirico, G. N. Barakos, and N. Bown. Propeller installation effects on turboprop aircraft acoustics. *Journal of Sound and Vibration*, 424:238–262, 2018.

[55] L. Luo, Huang X., and Zhang T. External and interior acoustics simulation for multi-propeller aircraft based on URANS + FW-H and acoustic-solid coupling. *Chinese Journal of Aeronautics*, 38(7):100093, 2025.

[56] J. Thoma, J. Delfs, S. Proskurov, and S. C. Langer. Cabin acoustics in preliminary aircraft design with propulsion pressure field excitation. In *Proceedings of DAS | DAGA 2025*, Copenhagen, Denmark, 2025.

[57] M. Cinefra, S. Passabia, and E. Carrera. FEM vibroacoustic analysis in the cabin of a regional turboprop aircraft. *Advances in Aircraft and Spacecraft Science*, 5(4):477–498, 2018.

[58] M. C. Moruzzi, M. Cinefra, S. Bagassi, and E. Carrera. Attenuation of noise in the cabin of a regional aircraft by metamaterial trim panels. In *32nd Congress of the International Council of the Aeronautical Sciences, ICAS 2020*, 2020.

[59] M. C. Moruzzi, M. Cinefra, and S. Bagassi. Vibroacoustic analysis of an innovative windowless cabin with metamaterial trim panels in regional turboprops. *Mechanics of Advanced Materials and Structures*, 28(14):1509–1521, 2021.

[60] P. Gardonio. Review of active techniques for aerospace vibro-acoustic control. *Journal of Aircraft*, 39(2):206–214, 2002.

[61] M. Misol. Full-scale experiments on the reduction of propeller-induced aircraft interior noise with active trim panels. *Applied Acoustics*, 159:107086, 2020.

[62] J. Romeu, J. I. Palacios, A. Balastegui, and T. Pàmies. Optimization of the active control of turboprop cabin noise. *Journal of Aircraft*, 52(5):1386–1393, 2015.

[63] K. Yoon, D. Kim, and S. Lee. Short-term annoyance reduction evoked by active noise control method on turboprop regional aircraft cabin noise. *Journal of Mechanical Science and Technology*, 33(4):1573–1584, 2019.

[64] I. Dimino, C. Colangeli, J. Cuenca, P. Vitiello, and M. Barbarino. Active noise control for aircraft cabin seats. *Applied Sciences*, 12(11):5610, 2022.

[65] S. G. Leão, E. C. Monteiro, M. O. dos Reis, L. P.P. Mapa, and A. F. Avila. Noise attenuation inside airplane cabin: Combined porous and nano-fibrous materials. *Applied Acoustics*, 199:109009, 2022.

[66] B. Aloufi, K. Behdinan, and J. Zu. Vibro-acoustic model of an active aircraft cabin window. *Journal of Sound and Vibration*, 398:1–27, 2017.

[67] T. Landi, C. Hoareau, J.-F. Deü, R. Ohayon, and R. Citarella. Comparative vibroacoustic analyses: FEM vs. IGA. *Computational Mechanics*, 76:1027–1059, 2025.

[68] T. J. R. Hughes. *The Finite Element Method: Linear Static and Dynamic Finite Element Analysis Vibroacoustic Analysis: Methods and Applications*. Dover, 2000.

[69] Ohayon R. Reduced models for fluid-structure interaction problems. *International Journal for Numerical Methods in Engineering*, 60:139–152, 2004.

[70] Morand HJ-P and Ohayon R. *Fluid-Structure Interaction: Applied Numerical Methods*. Wiley, 1995.

[71] Altair Engineering. *Normal Modes Analysis*. Altair Engineering Inc., 2024. Accessed: 2026-03-30.

[72] Hexagon Manufacturing Intelligence. *MSC Nastran 2024.2 - Dynamic Analysis User's Guide*. https://nexus.hexagon.com/documentationcenter/en-US/bundle/MSC_Nastran_2024.2_Dynamic_Analysis_User_Guide/resource/MSC_Nastran_2024.2_Dynamic_Analysis_User_Guide.pdf.

[73] G. Dessena and M. Civera. Multiple input tangential interpolation-driven damage detection of a jet trainer aircraft. *Aerospace Science and Technology*, 168:111032, 2026.

[74] Kvaternik R. G. A government/industry summary of the design analysis methods for vibrations (damvibs) program. Technical Report N93-21311, NASA, 1993.

[75] Hexagon Manufacturing Intelligence. *MSC Nastran 2024.1 Quick Reference Guide*. Hexagon Manufacturing Intelligence, 2024. https://nexus.hexagon.com/documentationcenter/en-US/bundle/MSC_Nastran_2024.1_Quick_Reference_Guide/resource/MSC_Nastran_2024.1_Quick_Reference_Guide.pdf.

[76] S. Martini de'Pompeis R., Cinquetti P. Development and certification flight test on the piaggio p.180 avanti aircraft: A general overview. Technical Report 911003, SAE International, 1991.

[77] George F. Piaggio aero p180 avanti ii. *Business & Commercial Aviation*, pages 116–125, 2007.

[78] A. Sollo. P.180 avanti: An iconic airplane and the achievement of an historical milestone. *Aerotecnica Missili & Spazio*, 100:69–78, 2021.

[79] Redazione Ares Difesa. Rilancio del p-180 da parte di baykar, January 2026. Accessed: 2026-04-07.

[80] AGEEI/Aerospazionews. Aviazione: Piaggio aerospace lancia il velivolo p.180 avanti nx e presenta la sua nuova brand identity, March 2026. Accessed: 2026-04-07.

[81] Piaggio Aerospace. *Avanti EVO – Specification and Description*. Piaggio Aero Industries S.p.A., 2016.

[82] P. T. Soderman and Clifton Horne W. Acoustic and aerodynamic study of a pusher-propeller aircraft model. Technical Report NASA-TP-3040, NASA, 1990.

[83] Quek S. S. Liu, G. R. *The Finite Element Method: A Practical Course*. Butterworth-Heinemann, Cambridge University Press, 2 edition, 2013.

[84] Siemens PLM Software. *Femap User Guide*. https://www.manuallib.com/download/2023-10-15/FEMAP%20User%20Guide.pdf.

[85] T. Polito, F. Marulo, A. Sollo, M. Aversano, and G. Pagnozzi. Modal and acoustic characterization of structural components for fuselage applications. In *Proceedings of the 24th International Conference on Noise and Vibration Engineering, Leuven, Belgium*, 09 2010.

[86] Robert D. Blevins. Formulas for natural frequency and mode shape. *Krieger Publishing Company*, 1995.

[87] R. R. Craig Chang T. C. Normal modes of uniform beams. *J. Eng. Mech. Div., Am. Soc. Civil Engrs.*, 95(1027-1031), 1969.

Appendix A

Analytical Estimation of Natural Frequencies and Preliminary Mesh Resolution Criteria

This appendix presents the closed-form analytical expressions used to estimate the natural frequencies and associated bending wavelengths of regular plate-like structural components. These estimates support the definition of preliminary mesh resolution criteria for FE analyses.

A.1 Approximate Natural Frequencies

As reported in [86], approximate closed-form solutions for the natural frequencies of rectangular plates can be obtained by assuming that the plate mode shape is approximated by the mode shapes of single-span beams along the x and y directions. The beam modal parameters used for this approximation are reported in Tables A.2 and A.3.

For example, a rectangular plate with simply supported–free–simply supported–clamped boundary conditions, as shown in Fig. A.1, can be approximated by considering a simply supported–simply supported beam along the x-direction and a clamped–free beam along the y-direction.

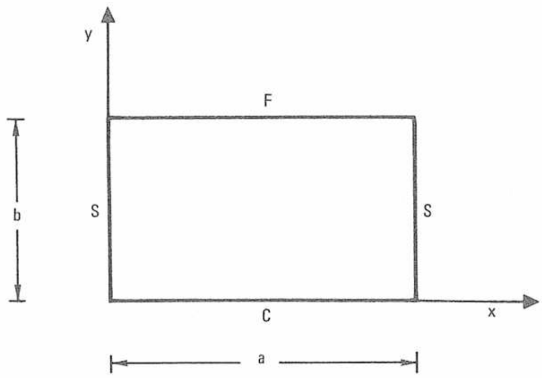

Fig. A.1 Coordinate system for a rectangular plate with simply supported–free–simply supported–clamped boundary conditions.

The approximate closed-form solution for the natural frequencies is obtained using the energy, or Rayleigh, method and gives an approximate natural frequency, in Hertz, in the form:

$$f_{ij} = \frac{\pi}{2}\left[\frac{G_1^4}{a^4} + \frac{G_2^4}{b^4} + \frac{2J_1J_2 + 2\nu(H_1H_2 - J_1J_2)}{a^2b^2}\right]^{\frac{1}{2}}\left[\frac{Eh^3}{12\gamma(1-\nu^2)}\right]^{\frac{1}{2}} \qquad \text{(A.1)}$$
$$i = 1, 2, 3, \ldots, \quad j = 1, 2, 3, \ldots$$

The dimensionless parameters G, H, and J, which depend on the modal indices i and j and on the boundary conditions of the plate, are reported in Table A.1. The quantities a, b, and h denote the plate length, width, and thickness, respectively; E is Young's modulus, ν is Poisson's ratio, and γ is the mass per unit area of the plate. For mesh-sizing purposes, the analytical formulation in Eq. A.1 can be used to obtain a preliminary estimate of the modal content of regular plane plate-like components up to a prescribed target frequency f_{conv}. In the present thesis, this frequency is selected higher than the maximum excitation frequency in order to ensure that the structural modal content is adequately resolved over the frequency range relevant to the vibroacoustic analyses.

For a regular plane component, Eq. A.1 is applied to determine the modal frequency f_{ij} closest to the target frequency f_{conv}, here denoted as f^*. Once this frequency is identified, all modal indices i and j associated with frequencies up to f^* are examined. The maximum values, $i_{\max}$ and $j_{\max}$, which do not necessarily correspond to the same modal pair associated with f^*, represent the

Table A.1 Boundary conditions, mode index and dimensionless parameters G, H, and J.

Boundary Condition	n	$G^{(a)}$	$H^{(a)}$	$J^{(a)}$
Free–Free	1	0	0	0
	2	0	1.248	1.216
	3	1.506	5.017	—
	$n\,(n>3)$	$n-\frac{3}{2}$	$\left(n-\frac{3}{2}\right)^2\left[1-\frac{2}{(n-\frac{3}{2})\pi}\right]$	$\left(n-\frac{3}{2}\right)^2\left[1-\frac{2}{(n-\frac{3}{2})\pi}\right]$
Simply Supported–Free	1	0	0	0.3040
	2	1.25	1.165	2.756
	3	2.25	4.346	7.211
	$n\,(n>1)$	$n-\frac{3}{4}$	$\left(n-\frac{3}{4}\right)^2\left[1-\frac{1}{(n-\frac{3}{4})\pi}\right]$	$\left(n-\frac{3}{4}\right)^2\left[1+\frac{3}{(n-\frac{3}{4})\pi}\right]$
Clamped–Free	1	0.597	-0.0870	0.471
	2	1.494	1.347	3.284
	3	2.500	4.658	7.842
	$n\,(n>2)$	$n-\frac{1}{2}$	$\left(n-\frac{1}{2}\right)^2\left[1-\frac{2}{(n-\frac{1}{2})\pi}\right]$	$\left(n-\frac{1}{2}\right)^2\left[1+\frac{2}{(n-\frac{1}{2})\pi}\right]$
Simply Supported–Simply Supported	1	1	1	1
	2	2	4	4
	3	3	9	9
	n	n	n^2	n^2
Clamped–Simply Supported	1	1.25	1.165	—
	2	2.25	4.346	—
	3	3.25	9.528	—
	n	$n+\frac{1}{4}$	$\left(n+\frac{1}{4}\right)^2\left[1-\frac{1}{(n+\frac{1}{4})\pi}\right]$	—
Clamped–Clamped	1	1.506	1.248	—
	2	2.5	4.658	—
	3	3.5	10.02	—
	$n\,(n>1)$	$n+\frac{1}{2}$	$\left(n+\frac{1}{2}\right)^2\left[1-\frac{2}{(n+\frac{1}{2})\pi}\right]$	—

highest modal orders to be resolved along the x and y directions, respectively. Once these limiting modal indices are identified, Tables A.2 and A.3 provide the corresponding non-dimensional frequency parameters and beam mode shapes for the relevant boundary conditions. The dimensional bending wavelength associated with each mode can then be estimated from the corresponding mode shape.

This wavelength provides a preliminary basis for evaluating the spatial resolution requirements of the FE model. The characteristic element size can be selected by prescribing a minimum number of elements per bending wavelength. In the present work, six elements per wavelength are adopted for the preliminary mesh estimate, consistently with commonly used wavelength-based resolution criteria for linear finite elements.

Table A.2 Single-Span Beams.
Notation: x = distance along span of beam; m = mass per unit length of beam; E = modulus of elasticity; I = area moment of inertia of beam about neutral axis; L = span of beam;

Natural frequency (hertz): $f_i = \dfrac{\lambda_i^2}{2\pi L^2}\left(\dfrac{EI}{m}\right)^{1/2}, \quad i = 1, 2, 3, \ldots$

Description	$\lambda_i; i = 1, 2, 3, \ldots$	Mode Shape $\tilde{y}_i\left(\frac{x}{L}\right)$	$\sigma_i; i = 1, 2, 3, \ldots$
1. Free-Free	4.73004074	$\cosh\frac{\lambda_i x}{L} + \cos\frac{\lambda_i x}{L}$	0.982502215
	7.85320462	$-\sigma_i\left(\sinh\frac{\lambda_i x}{L} + \sin\frac{\lambda_i x}{L}\right)$	1.000777312
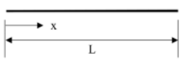	10.9956078		0.999966450
	14.1371655		1.000001450
	17.2787597		0.999999937
	$(2i+1)\frac{\pi}{2}; i > 5$		≈ 1.0 for $i > 5$
			See Ref. [87]
2. Free-Sliding	2.36502037	$\cosh\frac{\lambda_i x}{L} + \cos\frac{\lambda_i x}{L}$	0.982502207
	5.49780392	$-\sigma_i\left(\sinh\frac{\lambda_i x}{L} + \sin\frac{\lambda_i x}{L}\right)$	0.999966450
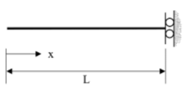	8.63937983		0.999999931
	11.78097245		0.999999993
	14.92256510		0.999999993

	$(4i-1)\frac{\pi}{4}; i>5$		$1.0; i>5$
3. Clamped-Free	1.87510407	$\cosh\frac{\lambda_i x}{L} - \cos\frac{\lambda_i x}{L}$	0.734095514
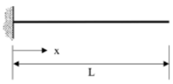	4.69409113	$-\sigma_i\left(\sinh\frac{\lambda_i x}{L} - \sin\frac{\lambda_i x}{L}\right)$	1.018467319
	7.85475744		0.999224497
	10.99554073		1.000033553
	14.13716839		0.999998550
	$(2i-1)\frac{\pi}{2}; i>5$		≈ 1.0 for $i>5$
			See Ref. [87]
4.Free-Pinned	3.92660231	$\cosh\frac{\lambda_i x}{L} + \cos\frac{\lambda_i x}{L}$	1.000777304
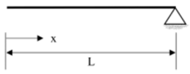	7.06858275	$-\sigma_i\left(\sinh\frac{\lambda_i x}{L} + \sin\frac{\lambda_i x}{L}\right)$	1.000001445
	10.21017612		1.000000000
	13.35176878		1.000000000
	16.49336143		1.000000000
	$(4i+1)\frac{\pi}{4}; i>5$		1.0; for $i>5$
5. Pinned-Pinned 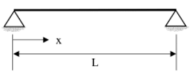	$i\pi$	$\sin\frac{i\pi x}{L}$	
6. Clamped-Pinned	3.92660231	$\cosh\frac{\lambda_i x}{L} - \cos\frac{\lambda_i x}{L}$	1.000777304
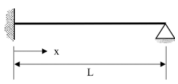	7.06858275	$-\sigma_i\left(\sinh\frac{\lambda_i x}{L} - \sin\frac{\lambda_i x}{L}\right)$	1.000001445
	10.21017612		1.000000000
	13.35176878		1.000000000
	16.49336143		1.000000000
	$(4i+1)\frac{\pi}{4}; i>5$		$1.0; i>5$

Table A.3 Single-span beams. (Continued)
Notation: x = distance along span of beam; m = mass per unit length of beam; E = modulus of elasticity; I = area moment of inertia of beam about neutral axis; L = span of beam.

Natural frequency (hertz): $f_i = \frac{\lambda_i^2}{2\pi L^2}\left(\frac{EI}{m}\right)^{1/2}, \quad i = 1, 2, 3, \ldots$

Description	$\lambda_i; i = 1, 2, 3, \ldots$	Mode Shape $\tilde{y}_i\left(\frac{x}{L}\right)$	$\sigma_i; i = 1, 2, 3, \ldots$
7. Clamped–Clamped	4.73004074	$\cosh\frac{\lambda_i x}{L} - \cos\frac{\lambda_i x}{L}$	0.982502215
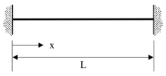	7.85320462	$-\sigma_i\left(\sinh\frac{\lambda_i x}{L} - \sin\frac{\lambda_i x}{L}\right)$	1.000777312
	10.9956079		0.999966450
	14.1371655		1.000001450
	17.2787597		0.999999937
	$(2i+1)\frac{\pi}{2}; i > 5$		$1.0; i > 5$
			See Ref. [87]
8. Clamped–Sliding	2.36502037	$\cosh\frac{\lambda_i x}{L} - \cos\frac{\lambda_i x}{L}$	0.982502207
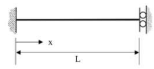	5.49780392	$-\sigma_i\left(\sinh\frac{\lambda_i x}{L} - \sin\frac{\lambda_i x}{L}\right)$	0.999966450
	8.63937983		0.999999933
	11.78097245		0.999999993
	14.92256510		0.999999993
	$(4i-1)\frac{\pi}{4}; i > 5$		$1.0; i > 5$
9. Sliding–Pinned 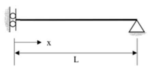	$(2i-1)\frac{\pi}{2}$	$\cosh\frac{(2i-1)\pi x}{2L}$	
10. Sliding–Sliding 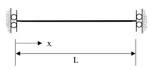	$i\pi$	$\cos\frac{i\pi x}{L}$	

Appendix B

Contribution to the scientific community and attended conferences

B.1 Journal and conference publications

B.1.1 Journal articles

- **Brancaccio C.**, Fasulo G., Palmiero F., Travostino G., Citarella R., "A Finite Element Modeling Approach for Assessing Noise Reduction in the Passenger Cabin of the Piaggio P.180 Aircraft", *Acoustics*, 7(3):54, 2025. https://doi.org/10.3390/acoustics7030054

- **Brancaccio C.**, Fasulo G., Palmiero F., Travostino G., Citarella R., "Finite Element Modeling of Piaggio P.180 Aircraft for Noise Reduction Assessment", *WSEAS Transactions on Applied and Theoretical Mechanics*, 20:113–118, 2025. https://doi.org/10.37394/232011.2025.20.13

B.1.2 Conference papers

- **Brancaccio C.**, Fasulo G., Barbarino M., Palmiero F., Travostino G., Citarella R., “Metamaterial-Based Passive Noise Control for the Piaggio P.180 Cabin”, AIAS2026 – 55º Convegno AIAS, Milan, Italy, 2026.
- **Brancaccio C.**, Fasulo G., Barbarino M., Palmiero F., Travostino G., Citarella R., “Numerical and Experimental Assessment of Cabin Noise Transmission Loss for Piaggio P.180 Aircraft”, 15th European Aerospace Science Network (EASN) International Conference on Innovation in Aviation & Space Towards Sustainability Today & Tomorrow, Madrid, Spain, 2025.
- **Brancaccio C.**, Citarella R., Testa C., Passacantilli F., Dessì D., Bernardini G., “Valutazione del rumore interno ad una stanza indotto dal traffico veicolare”, 50º Convegno Nazionale dell’Associazione Italiana di Acustica, Taormina, Italy, 2024.

“‘latex

B.2 Participation in scientific events

Date	Type	Event	Role
11/2023	Workshop	IEA Wind Task: Turbulent Inflow Innovative Aerodynamics (TURBINIA), Istituto di Ingegneria del Mare CNR-INM, Rome, Italy.	Speaker
01/2024	Workshop	Microelectronic Implementation for Noise Emissions Reduction and Vibration Assessment (MINERVA), Università di Roma Tre, Rome, Italy.	Speaker
05/2024	Conference	50º Convegno Nazionale dell’Associazione Italiana di Acustica (AIA), Taormina, Italy (*Acustica numerica e modelli previsionali* session).	Speaker

Date	Type	Event	Role
06/2025	Conference	International Conference on Applied Physics, Simulation and Computing (APSAC), Salerno, Italy (*Modelling, Simulation and Data Analysis in Engineering and Physics Applications* session).	Speaker
10/2025	Conference	15th European Aerospace Science Network (EASN) International Conference on Innovation in Aviation & Space Towards Sustainability Today & Tomorrow, Madrid, Spain (*Aerodynamic & Aeroacoustic Analysis and Design* session).	Speaker
02/2026	Workshop	Giornate di Lavoro, Comitato Tecnico Automotive AIAS, Università degli Studi di Modena e Reggio Emilia.	Speaker
09/2026	Conference	55º Convegno AIAS, Milan, Italy.	Scheduled speaker